Jorma Selin

Fluorescence Enhancement with Large-Scale Nanoparticle Arrays

School of Electrical Engineering

Thesis submitted for examination for the degree of Master of Science in Technology.

Espoo 19.10.2015

Thesis supervisor:

Prof. Ilkka Tittonen

Thesis advisor:

M.Sc. (Tech.) Ville Pale

Aalto University
School of Electrical
Engineering

AALTO UNIVERSITY
SCHOOL OF ELECTRICAL ENGINEERING

ABSTRACT OF THE
MASTER'S THESIS

Author: Jorma Selin

Title: Fluorescence Enhancement with Large-Scale Nanoparticle Arrays

Date: 19.10.2015 Language: English Number of pages: 8+81

Department of Micro- and Nanosciences

Professorship: Electrophysics Code: S-129

Supervisor: Prof. Ilkka Tittonen

Advisor: M.Sc. (Tech.) Ville Pale

For a multitude of biomedical applications, accurate sensing of fluorescence is essential. In addition to using more sophisticated measurement instruments, sensitivity in fluorescence sensing can also be improved by plasmonic nanostructures, owing to their ability to enhance molecular fluorescence.

Using finite element method modelling, this thesis designs plasmonic nanoparticle arrays suited for enhancing the fluorescence intensity of organic molecules. Such arrays are to be fabricated using a novel nanofabrication procedure based on azopolymer interference lithography. Relying only on parallel fabrication techniques, this fabrication procedure is readily scalable and economical. However, the procedure also imposes additional limits on feasible array designs.

In this work, the fluorescence enhancement efficiencies of fabricated array samples are quantified by confocal fluorescence microscopy. Additionally, fabricated arrays are characterized by UV–Vis spectroscopy, fluorescence spectroscopy, scanning electron microscopy, and atomic force microscopy. The results of these experiments are compared to simulations in order to investigate the applicability of finite element method modelling for designing fluorescence-enhancing plasmonic nanoparticle arrays. Based on these results, conclusions are also drawn on the precision of the nanofabrication procedure used for this thesis.

A maximum fluorescence enhancement factor of 4.11 was measured in this work. In agreement with the simulation results, this maximum value was achieved when the dipolar localized surface plasmon resonances of the studied array sample were tuned with the emission wavelength of the rhodamine 6G molecules used in the experiment. According to the experimental measurements, azopolymer interference lithography can be used to fabricate fluorescence-enhancing silver nanoparticle arrays with acceptably low variations in particle shapes and sizes, as well as in interparticle distances.

Keywords: Fluorescence, Fluorescence enhancement, Radiative decay engineering, Plasmon, Nanoparticle, Array, Finite element method, Azopolymer, Interference lithography

AALTO-YLIOPISTO
SÄHKÖTEKNIIKAN KORKEAKOULU

DIPLOMITYÖN
TIIVISTELMÄ

Tekijä: Jorma Selin

Työn nimi: Fluoresenssin vahvistaminen laajamittaisilla nanopartikkelihiloilla

Päivämäärä: 19.10.2015 Kieli: Englanti Sivumäärä: 8+81

Mikro- ja nanotekniikan laitos

Professuuri: Sähköfysiikka Koodi: S-129

Valvoja: Prof. Ilkka Tittonen

Ohjaaja: DI Ville Pale

Molekyylien fluoresenssin tarkka havaitseminen, ja tämän havaitsemistarkkuuden parantaminen, on tärkeää useissa biolääketieteen sovelluksissa. Yhä kalliimpien mittalaitteiden käyttöönoton lisäksi fluoresenssin havaitsemisen tarkkuutta voidaan parantaa myös fluoresenssia voimistavien plasmonisten nanorakenteiden avulla.

Tässä työssä suunnitellaan elementtimenetelmään perustuvien tietokonemallien avulla fluoresenssin vahvistamiseen soveltuvia plasmonisia nanopartikkelihiloja. Kyseiset hilat valmistetaan taloudellisella ja helposti skaalattavalla, atsopolymeeri-interferenssilitografiaan perustuvalla nanovalmistusmenetelmällä. Hyödyllisten ominaisuuksiensa vastapainoksi tämä valmistusmenetelmä asettaa kuitenkin ylimääräisiä rajoitteita suunniteltujen partikkelihilojen geometrioille.

Työn kokeellisessa osassa tarkastellaan valmiiden nanopartikkelihilojen soveltuvuutta fluoresenssin vahvistamiseen fluoresenssimikroskopian avulla. Kyseisiä hiloja myös karakterisoidaan ultravioletin ja näkyvän valon aallonpituuksien spektroskopian, fluoresenssispektroskopian ja sekä atomivoima- että pyyhkäisyelektronimikroskopian keinoin. Elementtimenetelmän soveltuvuus plasmonisten nanorakenteiden suunnittelussa todennetaan vertaamalla näiden kokeellisten mittausten tuloksia tietokonesimulaatioihin. Lisäksi mittaustulosten perusteella arvioidaan käytetyn valmistusmenetelmän tarkkuutta ja käyttökelpoisuutta.

Korkein tässä työssä mitattu fluoresenssivahvistuskerroin oli 4,11. Simulaatiotulosten mukaisesti tämä maksimiarvo saavutettiin sovittamalla tutkitun nanopartikkelihilan dipoliresonanssin ja väriaineena käytetyn rodamiini 6G:n fluoresenssin aallonpituudet toisiinsa. Tutkittujen näytteiden optisten ominaisuuksien ja nanomikroskopisin menetelmin todennetun riittävän tasalaatuisuuden perusteella atsopolymeeri-interferenssilitografian voidaan arvioida soveltuvan fluoresenssia vahvistavien hopeananopartikkelihilojen valmistamiseen.

Avainsanat: Fluoresenssi, Fluoresenssivahvistus, Plasmoni, Nanopartikkeli, Hila, Elementtimenetelmä, Atsopolymeeri, Interferenssilitografia

Preface

First and foremost, I wish to express my gratitude to Ville Pale and Christoffer Kauppinen, with whom I have had the pleasure to collaborate throughout my thesis project at the Micronova Nanofabrication Centre in Espoo. I want to thank Ville Pale for aiding me in formulating my research topic, and for his continuous help and supervision as my thesis advisor. Furthermore, Christoffer Kauppinen is gracefully acknowledged for his crucial contribution in fabricating the studied silver nanoparticle array samples.

I thank professor Ilkka Tittonen for acting as my thesis supervisor and for giving me the opportunity to continuously work as a part of his research group for the better part of my university studies. I would also like to extend my gratitude to the whole Micro and Quantum Systems Group for valuable support and feedback, as well as the occasional humorous comments and witticism. I am also grateful to Ville Kivijärvi for his aid concerning the finite element modelling of plasmonic nanostructures. Without his input, the computational part of this thesis would surely have been a complete disaster.

Additionally, this thesis would never have become reality without the support of my friends and family. It is, therefore, fitting to thank you all for filling my days with joy, interesting conversations, and a sense of purpose. Finally, special thanks should also be appointed to my dear wife, Lyyti. Despite my best efforts at being my annoying self, you have patiently stood by me. For that, I am forever grateful.

Otaniemi,
September 22, 2015

Jorma Selin

Contents

Symbols and abbreviations

Symbols

A	Area
C_a	Absorption cross section
C_{ext}	Extinction cross section
C_s	Scattering cross section
c	Molar concentration
c_0	Speed of light in vacuum
d	Thickness
E	Energy
$\mathbf{E}$	Electric field vector
F_{abs}	Absorption rate enhancement
F_P	Purcell factor
g	Acceleration of free fall
$\mathbf{H}$	Magnetic field vector
$\hbar$	Reduced Planck's constant
I	Intensity
i	Imaginary unit
k_B	Boltzmann constant
$\mathbf{k}$	Wave vector
l	Distance
n	Refractive index
P	Power
$P_{m\to k}$	Transition probability from state m to state k
Q	Quality factor
Q_a	Absorption efficiency
Q_{ext}	Extinction efficiency
Q_f	Fluorescence quantum yield
Q_s	Scattering efficiency
R	Reflectance
r	Radius
$\mathbf{S}$	Poynting vector
T	Transmittance
t	Time
U_0	Withdrawal speed
V	Potential energy
W	Energy transfer rate across a surface
α	Polarizability
β	Polar angle of diffracted waves
Γ	Transition rate
γ_{lv}	Liquid-vapour surface tension
ΔOPL	Optical path length difference
ϵ	Molar extinction coefficient

ε	Permittivity
ε_0	Vacuum permittivity
η	Viscosity
Q_{coll}	Collection efficiency
θ	Polar angle of incidence
Λ	Periodicity
λ	Wavelength
λ_{exc}	Excitation wavelength
λ_R	Rayleigh cut-off wavelength
μ_{km}	Transition dipole moment
ρ	Density
ϱ	Density of states
τ	Excited state lifetime
ϕ	Azimuthal angle
Ψ	Wavefunction
ω	Angular frequency
ω_0	Angular resonance frequency

Operators

$\hat{H}$	Hamiltonian operator
$\hat{X}_{km}$	Matrix element km of operator $\hat{X}$
$\langle ... \rangle$	Expectation value; Time average
$\lvert ... \rvert$	Vector norm

Abbreviations

2D	Two-dimensional
AFM	Atomic force microscopy
Ag	Silver
ALD	Atomic layer deposition
APIL	Azopolymer interference lithography
Ar	Argon
Au	Gold
CB	Cascade blue
DIW	De-ionized water
EBL	Electron beam lithography
FE	Fluorescence enhancement
FE-FOM	Fluorescence enhancement figure of merit
FEM	Finite element method
FWHM	Full width at half maximum
HOMO	Highest occupied molecular orbital
LIL	Laser interference lithography
LUMO	Lowest unoccupied molecular orbital

NA	Numerical aperture
NP	Nanoparticle
pDR1a	poly(Disperse Red 1 acrylate)
PML	Perfectly matched layer
PMT	Photomultiplier tube
R6G	Rhodamine 6G
RET	Resonance energy transfer
SEM	Scanning electron microscopy
SRG	Surface relief grating
UV–Vis	Ultraviolet–visible

1 Introduction

From its early beginning in the 1950s, the optical detection of fluorescent molecules has emerged as a crucial research tool in a variety of fields, including biotechnology, medicine, and forensic science. [1] Although a plethora of organic compounds fluoresce by themselves when excited with light of a suitable wavelength, the detection of fluorescence is applicable to the sensing of a wide range of molecules mainly due to the possibility of attaching fluorescent probes to non-fluorescent target molecules.

Fluorescence sensing is highly sensitive because photons emitted by different fluorophores can easily be differentiated according to their emission wavelengths. Compared to absorption measurements, fluorescence signals can be utilized for the detection of considerably smaller quantities of target molecules. [2] Furthermore, as fluorescent probes have been used for decades in various fields of science and technology, modern fluorescent molecules are highly efficient in producing optical signals. In some cases, fluorescence signals are detectable down to the single-molecule level. [3]

As further increases in detection sensitivity cannot be easily achieved by enhancing the optical properties of fluorescent molecules themselves, plasmonic noble metal nanoparticles (NPs) have received much attention due to their ability to enhance the light emission of fluorophores placed in the vicinity of the particles. The effect of such NPs is two-fold: they alter both the absorption and emission efficiency of the molecules. In general, the optical properties of noble metal NPs vary depending on the material, size, shape, environment, and arrangement of the particles. [4, 5] Therefore, both reproducibility and precision are needed in the fabrication of plasmonic NPs.

Noble metal NPs have been fabricated using both bottom-up and top-down fabrication approaches. The bottom-up approach refers to fabrication methods in which the metal particles are formed from their constitutive species, i.e., metal atoms, one at a time. Such techniques rely heavily on colloidal chemistry and can be used to produce metal NPs of multiple different shapes and sizes with minimal variations. [6] However, these chemical methods cannot be easily used to produce well-defined arrangements of particles, which can result in sizeable variations in the optical properties of densely packed colloidal structures. [7]

The second approach, top-down methods, usually utilizes electron beam lithography (EBL) to define the shapes of fabricated structures. Compared to bottom-up fabrication methods, EBL can produce more precise arrangements of plasmonic nanostructures with slightly increased size and shape variations. [8] EBL has been used for fabricating controlled arrays of various plasmonic structures, including disks [9], as well as squares and triangles [10], with total array sizes of the order of 100 μm $\times$ 100 μm. Although EBL has proved to be both versatile and reliable as a fabrication method, the technique is not cost-effective for the industrial-scale production of noble metal NP arrays, due to its serial nature. In order to circumvent this impediment, parallel top-down fabrication methods, such as nanosphere lithography [11], nanoimprint lithography [12], or laser interference lithography (LIL) [13], can be used for fabricating plasmonic structures. To develop such alternative methods, this thesis designs metal NP arrays to be subsequently fabricated using azopoly-

mer interference lithography (APIL). This fabrication method is a special variant of LIL, in which standard photoresists are replaced by an amorphous azobenzene-functionalized polymer. APIL can be used to produce precise NP arrays covering a comparably large area of roughly 1 cm^2. In this thesis, such arrays will be used for enhancing molecular fluorescence.

In order to develop suitable array designs for fluorescence enhancement, this thesis first establishes design rules for fluorescence enhancement with plasmonic NPs. The discussion on these design rules will emphasize the special geometrical restrictions imposed by the APIL method and the plasmonic materials used, as well as the problems these restrictions cause for different models and simulations. Then, the particle arrays are simulated using commercial finite-element method software. Suitable plasmonic NP arrays will finally be designed based on predictions drawn from the presented theory and simulation results. In the experimental part of the thesis, the optical properties of fabricated NPs will be measured and compared to theoretical predictions. The thesis also analyzes the effect of silver particles on the fluorescence of adjacent molecules. Fluorescence intensities of molecules deposited onto a two-dimensional array of similar NPs will be measured by both confocal microscopy and fluorescence spectroscopy and compared to intensities attainable without the NPs.

The research questions investigated in this thesis are formulated as follows. Can the models used in this thesis predict the optical properties of a metal NP array fabricated on a glass substrate and coated with a protective dielectric layer? In particular, can the designed arrays be successfully used as fluorescence-enhancing substrates for the detection of organic molecules? What is the extent to which fluorescence enhancement is achieved?

Three major factors define the scope of the present study: computational capacity, the APIL fabrication method, and accessible optical characterization methods. Due to limited computational capacity, the simulation models used in this thesis do not directly solve the emission rate enhancements experienced by organic molecules in the vicinity of metallic NPs. Because of the complexity of the APIL fabrication method, optical measurements will be performed on ready-made NP array samples. Moreover, the APIL method limits the obtainable NP shapes. Finally, optical measurements of single particles are not presented due to a lack of suitable characterization tools. All the conclusions of the thesis are, therefore, based exclusively on ensemble measurements.

The rest of this thesis is organized as follows. Chapter 2 introduces the concept of localized surface plasmon resonances and analyzes the effect of these resonances on the optical properties of noble metal NPs. Chapter 3 considers the quantized energy levels of organic molecules and energy transitions between different energy states. The chapter also presents a theoretical framework based on cavity quantum electrodynamics for understanding the fluorescence-enhancing effects of plasmonic particles. Chapter 4 describes the materials and methods used in the thesis, while the results of the thesis are presented and evaluated in Chapter 5. Finally, Chapter 6 provides some conclusions based on the achieved results.

2 Optical properties of metal nanoparticles

Naturally, a solid understanding of the optical properties of metal NPs is paramount if the particles are to be used for the enhancement of molecular fluorescence. This chapter describes the plasmonic response of noble metal NPs using classical electromagnetics. Sections 2.1 and 2.2 first present a series of basic concepts relevant to this thesis. Then, the following section (2.3) examines diversity in the optical response of plasmonic particles caused by variations in particle sizes and shapes. Section 2.4 explains effects caused by placing metal NPs on a dielectric substrate or covering the particles with a dielectric coating, while Section 2.5 describes the mutual interactions in an array of similar NPs. Section 2.6 is of utmost importance to this thesis, as it discusses the intense local field magnifications in two-dimensional arrays of metal NPs.

2.1 Localized surface plasmon resonances

When a metal NP is subjected to an electric field, positive and negative charges accumulate on the particle surface. This phenomenon is depicted in Figure 1. The extent and manner in which this surface charge is induced by the electric field determines the optical response of metal NPs. [14] This charge accumulation is highly dependent on the wavelength of the incident beam of light. When the response of a particle to a time-varying electric field is exceptionally strong, the particle is referred to as being resonant with the field.

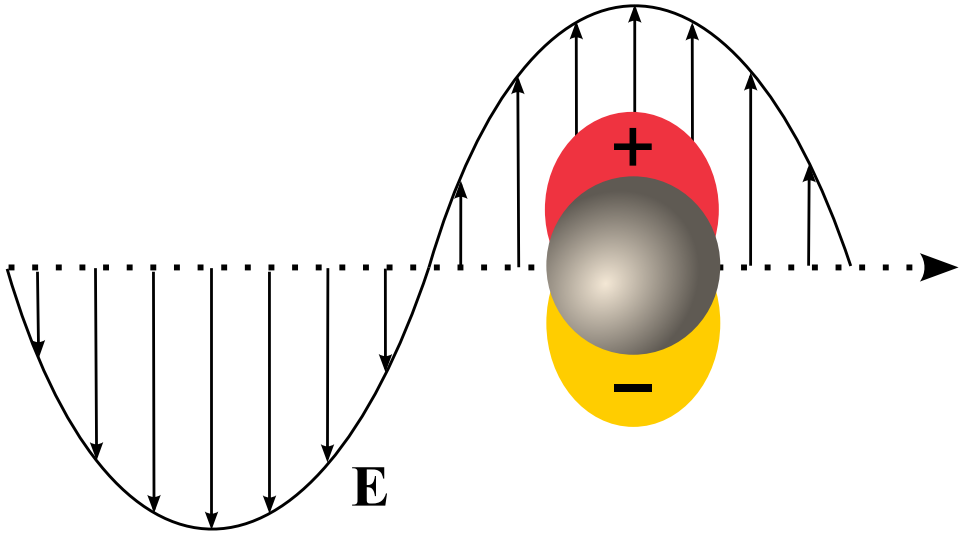

Figure 1: A metal nanoparticle in a sinusoidally varying electric field **E**.

In general, resonance can be broadly defined as a state of a system in which a repeating external stimulus triggers an exceptionally strong response by the system. A resonator is a structure or device that is resonant to only a set of certain frequencies, often referred to as the natural frequencies of the resonator. [15] At these natural frequencies, the vibrating field inside the resonator forms distinctive spatial

patterns called resonator modes. For example, a guitar string resonates at multiple frequencies with different characteristic displacement patterns, when struck by a guitarist. Resonant behaviour requires both spatial confinement and some feedback mechanism that converts energy back and forth between different forms, such as potential and kinetic energy. Resonators that provide confinement for electromagnetic fields are commonly referred to as cavities.

Real systems are always dissipative, i.e., they experience energy losses. The quality factor Q of a resonator is a dimensionless parameter whose value is proportional to the ratio of the energy stored inside the resonator to the power loss of the resonator. An approximate numerical value for the quality factor Q can be calculated from

$$Q = \frac{\omega}{\mathrm{FWHM}}, \tag{1}$$

where ω is the resonance frequency of the resonator and FWHM is the full width at half maximum of the resonance peak. [16] Increasing the Q of an optical resonator will increase the average photon lifetime inside the cavity. In Section 3.5, the effect of noble metal NPs on the light emission rates of organic molecules will be described by considering the particles as lossy (i.e., leaky) optical resonators.

The resonant normal modes of metal NPs have been termed localized surface plasmon modes, as the resonances occur due to collective oscillations of the conduction electrons in a given particle, and the modes are confined in space due to the finite size of the particle. [14] Depending on their sizes and shapes, NPs can possess a varying number of resonance frequencies with different electric field distributions. When the size of an NP is larger than the resonant plasmon wavelength and the incident field cannot penetrate deeply into the particle, the characteristic field distributions of these modes are strongly localized on the surface of the particle. On the other hand, small NPs can only support plasmon modes for which the electric field extends through the whole volume of the particle.

The material used for the fabrication of an NP affects both the plasmon resonance frequencies of the particle and the losses related to the resonances. In electromagnetics, material properties are commonly represented by a material and frequency-dependent complex permittivity, ε, or equivalently by the complex refractive index, n. In plasmonics, optical material parameters need additional adjustment for particles of different sizes and shapes to account for surface effects. [8] In this thesis, such considerations are omitted, as the utilized fabrication method (see Section 4.1) is expected to result in sufficiently sizeable structures to justify the use of bulk-like material parameters.

The optical properties of metals are often described using the Drude-Lorentz material model. This model describes the conduction electrons of metals as a freely-moving electron plasma held in place by the attractive Coulomb force exerted by the positive nuclei in the metal. [17] The optical properties of metals are mainly contributed to these free electrons. However, energy transitions between non-conducting electron states (i.e., interband transitions) are seen to produce additional energy losses in metals. An optimal plasmonic material should, therefore, have minimal

interband contribution in its material parameters at the frequency range of interest. In the visible wavelength range, the losses of silver (Ag) and gold (Au) are relatively low, explaining their wide-spread use in plasmonics. Of these two metals, Ag exhibits lower losses; however, the chemical reactivity of Ag particles has made Au the material of choice for practical applications. Since Ag is used as the plasmonic material in the present work, the particles are designed to be protected from ambient oxygen and other pollutants by a thin dielectric layer, as described in Section 4.1. Similar protective coatings for plasmonic Ag nanostructures have already been reported previously. [18]

2.2 Absorption, scattering, and extinction

When an atom, a molecule, or an NP is subjected to electromagnetic radiation, electrically charged constituents (e.g., protons and electrons) in the given nanometer-sized object are set in motion due to interactions with the impinging wave. These charged species then re-radiate energy in all directions. This secondary electromagnetic radiation is commonly referred to as scattered radiation. In elastic scattering, the light scattered by an object has the same frequency as the incident wave, whereas scattering with an ensuing frequency-shift is called inelastic. The constituent particles can also transform some of the incident energy into other forms of energy, a process known as absorption. In general, scattering is caused by the heterogeneity of a system. [14] Since practically all matter is heterogeneous at sufficiently small length scales, all media scatter light to some extent.

Suppose that a photodetector is placed in a beam of light. Let us define the radiation power initially received by the detector as P_0. If one or multiple metal NPs are then placed on the beam path before the detector, the received power will decrease to a value $P < P_0$. The addition of the NPs has then resulted in the extinction of the beam. In general, extinction is caused by both absorption and scattering processes and depends on the composition, size, shape, and orientation of the NPs. [7] Extinction is also dependent on the number of particles, properties of the surrounding medium, as well as the wavelength and polarization state of the incident light.

Let us then consider a single metal NP embedded in a non-absorbing medium and illuminated by an arbitrarily polarized monochromatic wave, $(\mathbf{E}_i, \mathbf{H}_i)$, of intensity I_i. The energy scattered by the NP corresponds to the scattered field, denoted by $(\mathbf{E}_s, \mathbf{H}_s)$. The electromagnetic field inside the particle is $(\mathbf{E}_{in}, \mathbf{H}_{in})$, whereas the field in the surrounding medium is referred to as $(\mathbf{E}_{out}, \mathbf{H}_{out})$. Owing to the linearity of the Maxwell equations, the field $(\mathbf{E}_{out}, \mathbf{H}_{out})$ outside the NP can be written as a superposition of the incident and scattered fields: [14]

$$\mathbf{E}_{out} = \mathbf{E}_i + \mathbf{E}_s, \tag{2}$$

$$\mathbf{H}_{out} = \mathbf{H}_i + \mathbf{H}_s. \tag{3}$$

If the fields are considered to be time-harmonic with $\exp(-i\omega t)$ time dependence,

the time-averaged Poynting vector $\langle \mathbf{S} \rangle$ outside the particle is given by

$$\langle \mathbf{S} \rangle = \frac{1}{2} \Re \langle \mathbf{E}_{out} \times \mathbf{H}^*_{out} \rangle = \langle \mathbf{S}_i \rangle + \langle \mathbf{S}_s \rangle + \langle \mathbf{S}_{ext} \rangle , \tag{4}$$

where

$$\begin{aligned} \langle \mathbf{S}_i \rangle &= \frac{1}{2} \Re \langle \mathbf{E}_i \times \mathbf{H}^*_i \rangle , \\ \langle \mathbf{S}_s \rangle &= \frac{1}{2} \Re \langle \mathbf{E}_s \times \mathbf{H}^*_s \rangle , \\ \langle \mathbf{S}_{ext} \rangle &= \frac{1}{2} \Re \langle \mathbf{E}_i \times \mathbf{H}^*_s + \mathbf{E}_s \times \mathbf{H}^*_i \rangle . \end{aligned}$$

One can then calculate the net energy flow across the boundary of the NP by integrating the Poynting vector on an imaginary closed surface, A, infinitesimally near but still outside the NP surface. If $\mathbf{n}$ is the outward-pointing unit vector of A, the time-averaged net transfer rate $\langle W_a \rangle$ of electromagnetic energy across surface A is

$$\begin{aligned} \langle W_a \rangle &= -\int_A \langle \mathbf{S} \rangle \cdot \mathbf{n} \; dA = -\int_A (\langle \mathbf{S}_i \rangle + \langle \mathbf{S}_s \rangle + \langle \mathbf{S}_{ext} \rangle) \cdot \mathbf{n} \; dA \\ &= -\int_A \langle \mathbf{S}_i \rangle \cdot \mathbf{n} \; dA - \int_A \langle \mathbf{S}_s \rangle \cdot \mathbf{n} \; dA - \int_A \langle \mathbf{S}_{ext} \rangle \cdot \mathbf{n} \; dA. \end{aligned} \tag{5}$$

Because the metal NP in question cannot produce energy, W_a is always a positive quantity. As the medium surrounding the particle is thought to be completely non-absorbing, W_a indicates the energy absorption rate of the metal NP. Furthermore, according to the divergence theorem $-\int_A \langle \mathbf{S}_i \rangle \cdot \mathbf{n} \; dA = 0$ because the incident field $(\mathbf{E}_i, \mathbf{H}_i)$ is a non-divergent plane wave. Then, let us further define

$$\langle W_s \rangle = \int_A \langle \mathbf{S}_s \rangle \cdot \mathbf{n} \; dA, \tag{6}$$

$$\langle W_{ext} \rangle = -\int_A \langle \mathbf{S}_{ext} \rangle \cdot \mathbf{n} \; dA, \tag{7}$$

where $\langle W_s \rangle$ and $\langle W_{ext} \rangle$ are termed the scattering and extinction rates of the particle, respectively. The former indicates the rate at which incident electromagnetic energy is re-radiated by the particle. With the given definitions we can finally write

$$\langle W_{ext} \rangle = \langle W_a \rangle + \langle W_s \rangle . \tag{8}$$

As presented in Equation 8, the total extinction rate $\langle W_{ext} \rangle$ is just the sum of the absorption and scattering rates of the particle.

All of the aforementioned energy transfer rates have the units of [W], i.e., energy per unit time. If $\langle W_{ext} \rangle$, $\langle W_a \rangle$, and $\langle W_s \rangle$ are then divided by the intensity I_i of the incident plane wave, we get

$$C_{ext} = C_a + C_s = \frac{\langle W_a \rangle}{I_i} + \frac{\langle W_s \rangle}{I_i}, \tag{9}$$

where C_{ext}, C_a, and C_s have dimensions of area and are often referred to as the extinction, absorption, and scattering cross sections of the NP, respectively. Spectral maxima in these cross sections correspond to the resonant frequencies of the plasmon modes in the particle. Additionally, the cross sections of Equation 9 can be compared with the area $A_\perp$ of the projection of the NP onto a plane perpendicular to the impinging beam:

$$Q_{ext} = Q_a + Q_s = \frac{C_a}{A_\perp} + \frac{C_s}{A_\perp}. \tag{10}$$

The quantities Q_{ext}, Q_a, and Q_s are called the efficiencies for extinction, absorption, and scattering. Despite their somewhat misleading nomenclature, the magnitudes of these efficiency factors can be significantly larger than unity.

2.3 Size- and shape-related variation in plasmonic properties

As will be further discussed in Section 3.5, controlling the plasmon resonance frequencies of metal NPs is especially important for improving the fluorescence intensity of organic molecules in the vicinity of the particles. Since the resonant frequencies of plasmon modes can be distinguished as maxima in extinction spectra, this section describes variations in the spectral properties of plasmonic NPs with different sizes and shapes using the terminology provided in the preceding section.

Plasmonic structures can be roughly divided into two size regimes: the quantum and the classical regime. In the quantum regime, plasmonic structures contain features with sizes of the order of 1 nm, and their properties need to be described using quantum mechanics. [19] If not strictly necessary, the properties of plasmonic structures are, however, not calculated using quantum simulations, as the computational effort required would be unreasonably high. Due to the nanofabrication method used in this thesis (see Section 4.1), quantum phenomena are assumed to be insignificant, and quantum-mechanical simulations will not be used.

In the second size regime, classical electrodynamics can be used to predict the optical properties of plasmonic NPs. The optical properties of spherical particles are often described by an exact analytical framework commonly referred to as Mie theory, which has also been used to study spheroidal particles [20] and coated spheres [21]. Using generalized Mie theory, even the optical properties of collections of such particles can be numerically calculated. [17] Nevertheless, Mie solutions can be applied only in the case of relatively simple, highly symmetric geometries. In this thesis, Ag NP arrays are fabricated onto a glass substrate and coated by a protective dielectric layer, both design choices reducing the symmetry of the final structures. The optical properties of plasmonic particles are, therefore, modelled using finite element simulations (see Section 4.3). This allows simulating particles with various sizes and shapes, as well as in different environments and arrangements.

In the following discussion, the size- and shape-dependent optical properties of plasmonic particles will be introduced by considering the properties of various ellipsoidal particles (i.e., spheres, spheroids, and general, tri-axial ellipsoids) of different sizes, ordered based on increasing NP size. The scope of this section is limited to

NPs with diameters ranging from roughly 20 nm to 200 nm. Then, Sections 2.4 and 2.5 will present effects induced by the environment and arrangement of plasmonic particles, respectively.

This section first describes the properties of noble metal NPs with diameters of the order of 20 nm. Although the plasmon resonance frequencies of these small NPs are reasonably stable with respect to the exact volume of the particles, the plasmon resonances are highly dependent on particle shapes. [17] As a first example, Figure 2 depicts the vacuum absorption and scattering spectra of a small spherical Ag NP with a radius of 20 nm and the electrical near field in the proximity of the particle at its resonance frequency. As depicted in the figure, spherical particles with radii less than roughly 30 nm exhibit only a single dipolar resonance, when illuminated by plane waves in the visible wavelength range, and their extinction spectrum is mainly comprised of absorption with a minute scattering contribution.

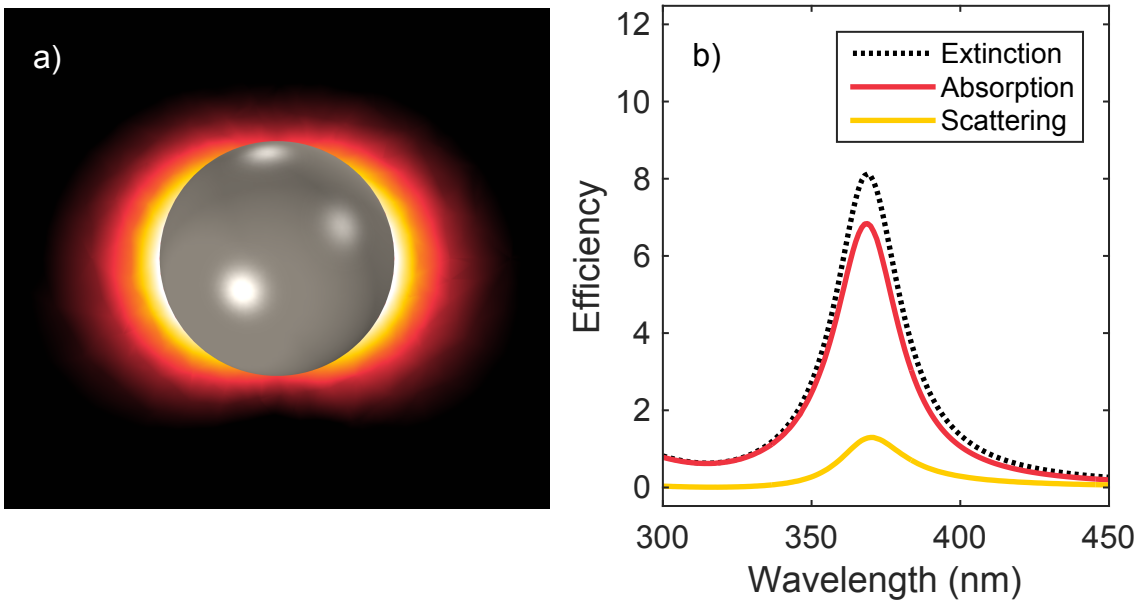

Figure 2: a) The simulated near field pattern of a spherical silver nanoparticle with a radius of 20 nm at resonance ($\lambda_{exc} = 369$ nm), and b) its extinction, absorption, and scattering spectra in vacuum.

For a particle with a diameter below approximately 50 nm, retardation of a light wave is negligible throughout the surface of the particle. Consequently, the extinction spectra of such a particle can be approximately calculated using quasi-static analytical models, i.e., by treating a plane wave incident on such a particle as a constant electric field. [14] In this quasi-static size regime, Mie theory can be used to derive simple analytical expressions for the resonance conditions of various symmetric NP geometries. In particular, the dipole resonance frequency of small spherical particles can by approximated by the well-known Fröhlich condition:

$$\Re\left\{\frac{\varepsilon_p}{\varepsilon_m}\right\} = -2, \tag{11}$$

where ε_p is the permittivity of the particle and ε_m is the permittivity of the surrounding medium. [22] For Ag particles in vacuum, this criterion is satisfied when the wavelength of the incident beam of light is roughly 350 nm. This simple result is in relatively good agreement with Figure 2.

Although the extinction spectra of small spherical particles feature only dipolar resonances, the particles can also sustain higher order resonances. Such multipolar dark modes can, for example, be excited by the near fields of an organic molecule. [23] In the electrostatic limit, the resonance frequencies of a homogeneous metal sphere occur whenever $|l\varepsilon_p + (l+1)\,\varepsilon_m|\,,\ l = 1, 2, 3...$ reach their minima. [24] The case when $l = 1$ corresponds to the Fröchlich condition of Equation 11, and higher values of l correspond to multipolar resonances. For example, the quadrupole resonance of a spherical Ag particle in vacuum can be approximately calculated to occur at a wavelength of 345 nm. Evidently, both the dipole and multipole resonances of small spherical particles occur at similar wavelengths.

As opposed to small spherical NPs, ellipsoidal particles resonate at multiple frequencies under plane wave illumination. A spheroidal particle (i.e., an oblate or prolate spheroid) having two semi-axes of equal length shows two dipole resonances with dipole moments parallel and perpendicular to its symmetry axis. [14] Similarly, a tri-axial ellipsoid exhibits three resonances with dipole moments along the principal axes: the dipole moment of the lowest resonance frequency is directed along the longest axis, and the highest frequency along the shortest axis. In general, reduced symmetry in a plasmonic structure allows for an increased number of resonance frequencies. [25] In addition to producing multiple resonances, elongation of an NP from a spherical to a more ellipsoidal shape has also been shown to increase its scattering efficiency. [26]

Continuing with larger NPs, Figure 3 shows the extinction spectrum of a spherical Ag NP with a radius of 50 nm. The spectrum is composed of two separate peaks corresponding to a dipolar resonance at 408 nm and a quadrupolar resonance at 359 nm. In the case of the 50 nm particle, the dipole resonance shows a clear red-shift compared to that of the smaller particle shown previously in Figure 2. This red-shift originates from the increased depolarization of incident radiation across an NP when the size of the NP increases, an effect commonly referred to as dynamic depolarization. [27] Figure 3 also depicts the near field around a plasmonic NP at the quadrupolar resonance wavelength. Comparison with the previous figure reveals a distinctive difference in the electric near field patterns of dipole and quadrupole resonances.

In general, increasing the size of an NP above the quasi-static limit allows the multipolar resonances of a particle to couple more efficiently to the far field. This effect has been demonstrated experimentally, for example, in the case of colloidal Ag NPs. [28] However, though characteristic of large spherical particles, multipolar extinction peaks have been shown to be less pronounced in the case of spheroidal and tri-axial ellipsoidal particles than spherical ones. This quenching of multipolar resonances was demonstrated specifically for oblate spheroid particles, using exact electrodynamic calculations. [7]

With increasing size, plasmonic particles also become more efficient scatterers

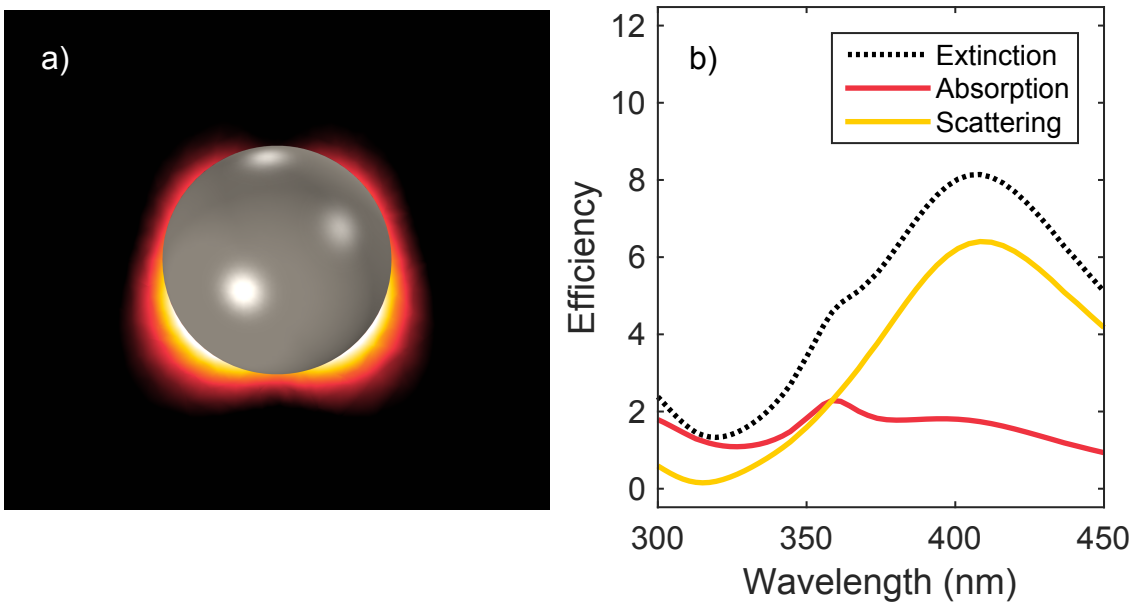

Figure 3: a) The simulated near field pattern of a spherical silver nanoparticle with a radius of 50 nm at resonance ($\lambda_{exc} = 359$ nm), and b) its extinction, absorption, and scattering spectra in vacuum.

of incoming radiation. This increase in scattering decreases the dipole moment of a particle induced by an impinging beam of light. As a result, the extinction spectra of larger plasmonic particles broaden compared to those of smaller particles, an effect often referred to as radiative damping. [7] If these particles are thought of as optical cavities, their quality factors are decreased by the increased radiative losses. For plasmonic fluorescence enhancement (FE), the quality factors of metal NPs are critical, as a reduction in the quality factor of an optical cavity decreases the emission rates of organic fluorophores inside the cavity (see Section 3.5) However, radiative damping should not be considered unconditionally detrimental to FE, as proposed in Section 3.6.

2.4 Resonance shifts due to nearby dielectrics

The previous section examined variations in plasmon frequencies and their characteristic field distributions caused by changes in the sizes and shapes of noble metal NPs. Building on the preceding discussion, this section outlines environmental effects in the case of individual plasmonic NPs. These effects can be divided into two categories: coating- and substrate-induced effects. After pointing out some general remarks, this section presents the properties of coated NPs and concludes with substrate-induced effects.

In general, the resonance wavelengths of a plasmonic NP depend on the local refractive index of the medium surrounding the particle. In a homogeneous environment, increasing the refractive index of the medium surrounding a plasmonic NP has been shown to red-shift the resonance wavelengths of the particle [7], and these

red-shifts show an approximately linear dependence on refractive index [29]. For a given NP, the sensitivity of its resonance wavelengths to variations in local refractive index is determined by its shape, sharper features enhancing the sensitivity. [6] In addition to inducing red-shifts in the resonances of plasmonic NPs, an increase in the refractive index of the surrounding medium has also been shown to enhance the scattering efficiency of plasmonic particles. [26]

The addition of a dielectric coating onto a plasmonic NP can be qualitatively described as affecting the local refractive index environment of the particle. More specifically, in the quasi-static size regime, the polarizability α of a spherical NP with radius r coated with a dielectric coating of thickness d can be written as

$$\alpha \propto 4\pi(r+d)^3 \frac{(\varepsilon_c - \varepsilon_m)(\varepsilon_p + 2\varepsilon_c) + f(\varepsilon_p - \varepsilon_c)(\varepsilon_m + 2\varepsilon_c)}{(\varepsilon_c + 2\varepsilon_m)(\varepsilon_p + 2\varepsilon_m) + f(2\varepsilon_c - 2\varepsilon_m)(\varepsilon_p - \varepsilon_c)}, \tag{12}$$

where ε_p, ε_c, and ε_m refer to the permittivities of the particle, coating, and the surrounding medium, respectively. [22] Additionally, $f = r/(r+d)$ denotes the ratio of the particle radius to the combined radius of the particle and the coating. The resonance frequencies of a coated NP correspond to maxima in its polarizability.

To illustrate the effect of dielectric coatings, Figure 4 depicts the plasmon resonance wavelengths of spherical Ag NPs in the quasi-static limit as a function of coating refractive index. For all three cases depicted in the figure, an approximately linear dependence can be seen between the plasmon resonance wavelength and the refractive index of the coating. Although Equation 12 and Figure 4 are based on quasi-static equations, the resonance frequencies of larger NPs follow a similar trend. For thin coatings with thicknesses below roughly 50 nm, red-shifts can be strengthened by increasing either the refractive index [30] or the thickness [31] of the coating. In the case of thicker coatings, interference [32] and waveguiding [33] phenomena may be relevant. In this thesis, such considerations are assumed to be of minor significance due to the relatively minor coating thickness used (see Section 4.1).

Contrary to the case of dielectric coatings presented above, the effects of a high-refractive index substrate on the optical properties of plasmonic NPs cannot be considered merely as being caused by changes in the local refractive index environment of the particles. Upon optical excitation, plasmonic particles placed above a substrate experience surface charge density oscillations that induce the build-up of charges on the substrate–superstrate interface. For short particle–substrate distances, the effect of this charge accumulation can be approximated using the concept of image charges. [34] In such a scheme, an inverted image of the charge distribution on the surface of an NP is produced underneath the substrate surface with a magnitude reduced by a factor of $(\varepsilon_2 - \varepsilon_1)/(\varepsilon_2 + \varepsilon_1)$, where ε_1 and ε_2 refer to the permittivities of the superstrate and substrate, respectively. Such a situation is depicted in Figure 5 below. The plasmon resonance shifts imposed by the dielectric substrate can then be viewed as being produced by the interaction of the real charge distribution on the surface of the particle with its reversed image. The strength of this interaction depends on the nanoparticle–substrate separation, permittivities of the substrate and superstrate, and the polarization state of incident light. [35]

The simplified image charge model can predict two important effects caused by

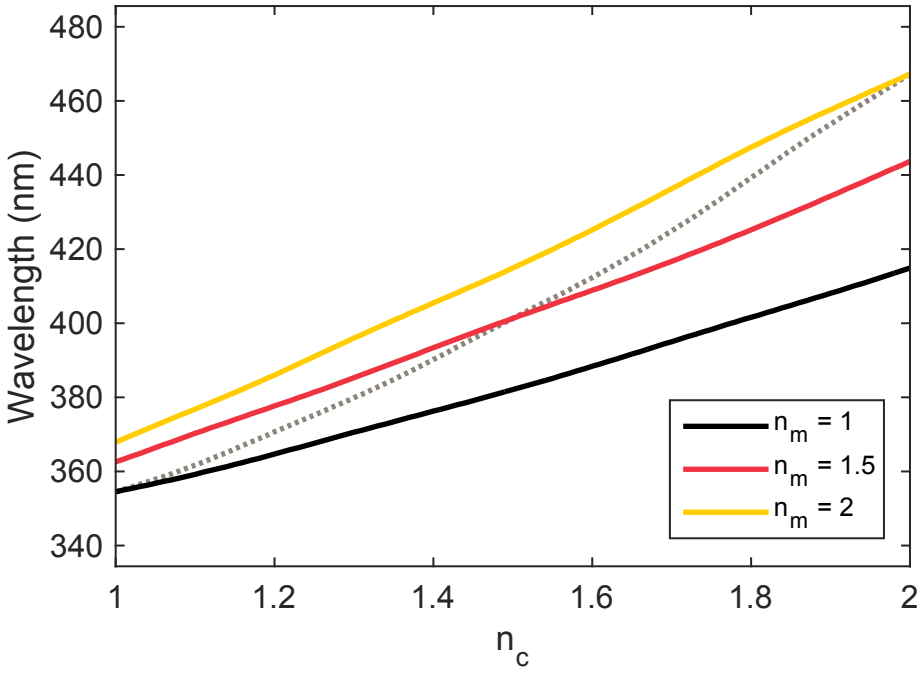

Figure 4: The plasmon resonance wavelengths of coated spherical silver nanoparticles with radii of 10 nm and coating thicknesses of 5 nm as a function of the coating refractive index n_c. The three lines correspond to different values for the refractive indices n_m of the surrounding medium. The plasmon resonance wavelengths of similar silver spheres in homogeneous environments with refractive indices of n_c are additionally indicated in the figure (dotted grey line).

a planar substrate on the extinction spectra of plasmonic NPs: increased multipolar extinction and scattering, as well as the energy splitting of degenerate resonances. The coupling of multipolar plasmon resonances to the far field can be facilitated by the accumulation of charges on the substrate surface, since the presence of the substrate imposes partial dipolar character to the multipolar resonances. Furthermore, a dielectric boundary can lift the mode degeneracy of symmetrical particles, such as spheres and spheroids. These two effects have been demonstrated experimentally by dark-field microscopy [35] and simulated using finite-difference time-domain simulations [36].

In addition to the two substrate-induced effects described above, fabricating NPs on a planar substrate also introduces a third effect related to the geometry of the particles themselves. Due to direct contact with the substrate, supported NPs tend to form in truncated spheroidal shapes, the exact dimensions of which depend on the growth conditions. [37] Naturally, the optical properties of such truncated particles differ from those of perfect spheroids. Primarily, the reduction in particle symmetry imposed by the substrate results in inhomogeneous polarization fields in supported NPs, enhancing the coupling of multipolar plasmon resonances to the far field. [38]

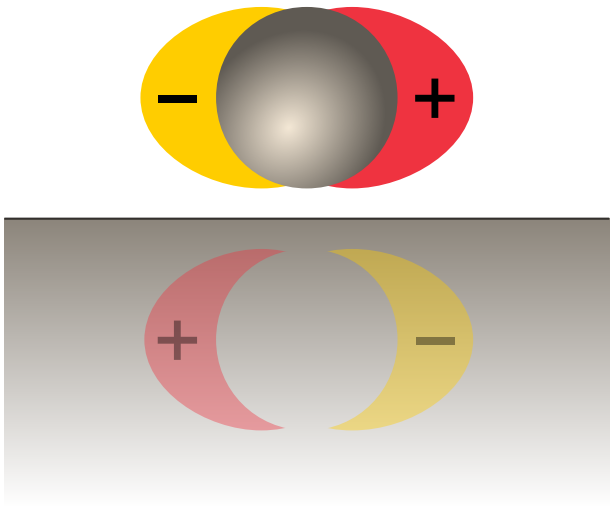

Figure 5: The quasi-static image charge model of substrate effects for plasmonic nanoparticles placed in the vicinity of a planar dielectric boundary.

2.5 Plasmon coupling

The local environment of plasmonic NPs affects their optical response, as already elaborated in the preceding section. In addition to their dielectric environment, the arrangement of individual NPs in an assembly influences the optical properties of the total assembly. Two main factors contribute to the properties of plasmonic NP assemblies: regularity and interparticle spacing. Although the field of FE has a rich history in using irregular assemblies of plasmonic NPs (for example, see Ref. [39]), this section focuses on two-dimensional, regular NP arrangements (i.e., 2D arrays) with interparticle spacings comparable to visible wavelengths. Such a scope is justified by the fabrication method used for producing arrays simulated in this thesis (see Section 4.1). Compared to irregular arrangements, utilization of regular array designs is presumed to facilitate the synthesis of theoretical predictions with measurement results.

Two distinctive features differentiate the extinction spectra of 2D NP arrays and individual NPs: wavelength shifts in localized surface plasmon resonances (i.e., single-particle resonances) and the appearance of collective array resonances. Wavelength shifts in single-particle resonances occur due to interactions between individual NPs. For sufficiently small, closely packed NPs, these interactions result in red-shifted extinction and scattering spectra for interacting NPs compared to individual NPs. Such red-shifts can be described as resulting from static dipole interactions [40] or plasmon hybridization [41] between individual particles.

However, more accurate models are needed in the case of larger particles and lengthened interparticle distances. Although the applicability of the plasmon hybridization model is rather limited above the quasi-static limit, the dipolar coupling model can be extended to take into account phase retardation and radiative cou-

pling [42], as well as multipolar coupling effects [43]. For example, dipolar single-particle resonances in rectangular arrays of spherical particles have been shown to exhibit blue-shifts with decreasing array periodicity Λ if

$$\Lambda \gtrsim \frac{\lambda_s}{2\pi}, \tag{13}$$

where λ_s is the wavelength of the single-particle resonance. [40] Further decreases in Λ were seen to result in red-shifted spectra. A reduction in Λ also resulted in narrower single-particle resonances for array perodicities above 180 nm. Additionally, the magnitudes of the spectral shifts in single-particle resonances have been shown to increase with increasing number of NPs. [44] However, the number of NPs was seen to have only a minor effect on the optical response of regular arrays beyond an array size of 16×16 particles.

The remainder of this section describes the collective resonances of regular 2D NP arrays. Fundamentally, collective array resonances can be interpreted as an interference phenomenon. When a periodic NP array is illuminated by light, the local electric field experienced by a single particle is composed of the incident wave and the waves scattered by all the other particles in the array. Assuming coherent illumination, the magnitudes and relative phases of these waves determines the total electromagnetic field experienced by an individual particle in the array. Generally, two distinctive features are observed in the extinction spectra of diffractively coupled arrays: Wood anomalies (corresponding to local minima in extinction) and collective plasmon modes (corresponding to local maxima in extinction). [45] Wood anomalies occur whenever a diffraction order of a grating or an array changes from radiative to evanescent state. [46] The particular wavelengths at which this occurs are commonly referred to as Rayleigh cut-off wavelengths. Collective plasmon resonances are slightly red-shifted with respect to these Rayleigh cut-off wavelengths. [45]

In order to study collective resonances in plasmonic NP arrays, let's assume a plane wave with vacuum wavelength λ_0 incident on a rectangular, 2D NP array supported on a dielectric substrate, as depicted in Figure 6. The wavelength λ_0 is presumed to overlap with the localized surface plasmon resonance of the particles.

Let's first consider the diffraction of incident light into the substrate. The optical path length difference ΔOPL_{air} in the superstrate for rays 1 and 2 can be written as

$$\Delta OPL_{air} = n_{air} \frac{\mathbf{k}_{air}}{|\mathbf{k}_{air}|} \cdot \left(Ma\hat{i} + Nb\hat{j} \right) = n_{air} \sin\theta \left(Ma\cos\varphi + Nb\sin\varphi \right), \tag{14}$$

where n_{air} is the refractive index of the superstrate, a and b are the array lattice constants in the x- and y-directions, respectively, and $M, N = 0, 1, 2...$ Additionally, the optical path difference ΔOPL_{sub} corresponding to passage of light beneath the substrate surface is given by

$$\Delta OPL_{sub} = n_{sub} d \sin\beta = n_{sub} \sqrt{(Na)^2 + (Mb)^2} \sin\beta, \tag{15}$$

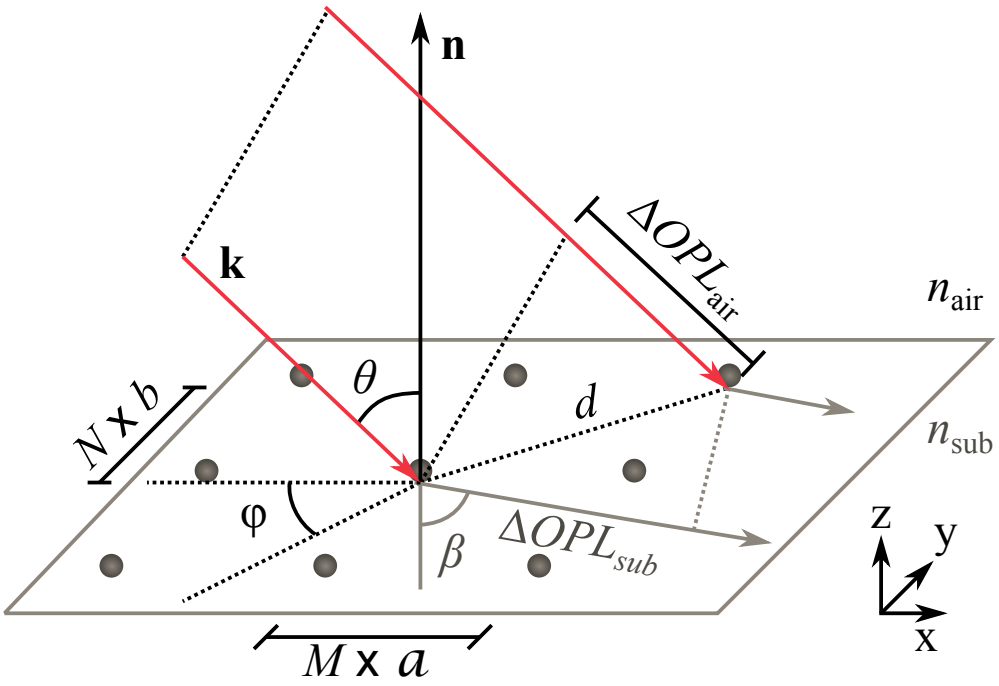

Figure 6: Diffraction from a rectangular array of nanoparticles with periodicities a and b in the x- and y-directions, respectively. The polar angle of incidence with respect to the z-axis is θ, the azimuthal angle of incidence with respect to the x-axis is φ, and the polar angle of the diffracted wave is β. For the presented case, $M = N = 1$.

where n_{sub} is the refractive index of the substrate and $\sin\beta$ is the azimuthal angle of the diffracted wave.

For constructive interference to occur between rays 1 and 2, the combined optical path length difference $\Delta OPL_{tot} = \Delta OPL_{air} + \Delta OPL_{sub}$ between the two paths has to equal a multiple of the vacuum wavelength λ_0. Furthermore, diffraction into the plane of the array suggests $\sin\beta = 1$. For a rectangular array, the Rayleigh cut-off wavelengths λ_R^{sub} are then given by the following condition:

$$m\lambda_R^{sub} = n_{sub}\sqrt{(Na)^2 + (Mb)^2} \pm n_{air}\sin\theta\,(Ma\cos\varphi + Nb\sin\varphi)\,. \tag{16}$$

The $\pm$-sign in Equation 16 results from purely geometrical considerations. Setting $a = b = \Lambda$ yields a simple equation for the Rayleigh cut-off wavelengths λ_R^{sub} of a 2D square array as

$$\lambda_R^{sub} = \frac{\Lambda}{m}\left[n_{sub}\sqrt{N^2 + M^2} \pm n_{air}\sin\theta\,(M\cos\varphi + Nb\sin\varphi)\right]. \tag{17}$$

However, Equation 17 only takes into account the Rayleigh cut-off wavelengths corresponding to the disappearance of so-called substrate diffraction modes, i.e., wavelengths at which a diffraction order crosses the substrate–superstrate boundary from the substrate to the superstrate. One can similarly show that additional superstrate

resonances occur whenever

$$\lambda_R^{air} = \frac{\Lambda}{m}\left[n_{air}\sqrt{N^2+M^2} \pm n_{air}\sin\theta\,(M\cos\varphi + Nb\sin\varphi)\right]. \quad (18)$$

A similar expression for λ_R^{air} can be found in the literature. [46] Remembering that collective plasmon resonances occur at wavelengths slightly red-shifted from λ_R^{sub} and λ_R^{air}, Equations 17 and 18 can be used for the engineering and identification of collective resonances in rectangular NP arrays.

The number of experimentally observable array resonances is usually limited to the very lowest order resonances. [47] This limitation can be attributed to three factors: the limited spectral range of plasmon resonances of individual NPs, interference effects in the substrate-superstrate boundary [48], and inhomogeneity in realistic systems [5]. In order to strengthen diffractive coupling and array resonances, individual particles should exhibit minimal size variations and be large enough to show high scattering cross sections. Additionally, individual particles should be thick enough to reduce the disturbances caused by the planar dielectric boundary beneath the particles, and the refractive indices of the substrate and the superstrate should be sufficiently closely matched to each other. [49] Although most of the literature focuses on the so-called orthogonal collective resonances (i.e., array resonances in which the incident electromagnetic field is orthogonally polarized with respect to the diffraction wave vectors of the modes), the necessity of this refractive index matching could be reduced by using parallel resonances. [50]

2.6 Local field enhancement

Various applications of plasmonic metal NPs, including surface-enhanced Raman spectroscopy [51] and FE, rely on the ability of plasmonic NPs to focus electromagnetic energy into small volumes. In the case of individual particles, this focusing effect has traditionally been attributed to two different factors: plasmonic enhancement at the resonance frequencies of the particles and the lightning rod effect, which is independent of the frequency of incident radiation. [52] Plasmonic enhancement refers to the accumulation of surface charges associated with localized surface plasmon oscillations that generate strong electric fields close to the surface of an NP. Naturally, the amount of accumulated charge is influenced by the material, size, and shape of the particle. On the other hand, the lightning rod effect is caused by sharp, high-curvature features in NPs, as the electric fields associated with electromagnetic radiation typically align perpendicular to conducting surfaces. In addition to these single-particle effects, interactions between adjacent particles can be used to produce highly focused fields. In order to elucidate these phenomena, this section critically reviews local field enhancements reported in the literature, starting with individual spherical particles.

The maximum electric field enhancements produced by plasmonic structures depend on particle shapes. For example, the electric field enhancements on the surfaces of spherical particles can be calculated using Mie theory, and the highest resonant electric field intensity enhancement on the surface of a 20 nm diameter Ag

sphere has been shown to be roughly 240. [53] The local fields of such a particle were also shown to be highly localized close to the particle surface, as they diminished rapidly with increasing distance from the sphere. In the case of ellipsoidal particles, highest simulated field enhancements were increased compared to spherical particles. The maximum electric field enhancement produced by an oblate spheroid with minor and major semi-axes of 22.6 nm and 6.6 nm, respectively, was shown to be of the order of 4700. This increase in field enhancement can be attributed to the lightning rod effect caused by the highly curved surface of the spheroid.

In addition to particle shape, the exact numerical values for field enhancements depend also on particle sizes. For prolate spheroids, peak enhancements have been shown to be reduced by increasing particle size. [54] To demonstrate this effect, Figure 7 depicts the electric field enhancement at the tip of a prolate Ag spheroid as a function of axial ratio and length. Maxima in enhancement correspond to the plasmon resonances of the particle. These maxima can be seen to decrease from roughly 200 to 50 as the major axis length of a prolate spheroid is increased from approximately 100 nm to 1600 nm.

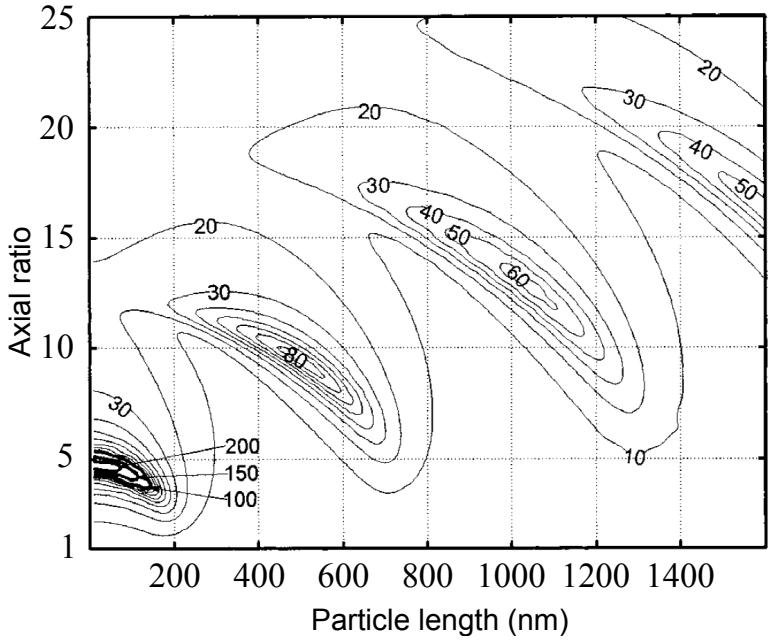

Figure 7: Contour plot of the electric field enhancement at the end of a silver spheroid at an excitation wavelength of 633 nm. Figure re-drawn based on Ref. [54].

As mentioned previously, interparticle effects can also produce enhanced fields. By utilizing the near-field interactions of multiple particles, very high field intensity enhancements of the order of 5×10^4 have been theoretically predicted. [53] In particular, such enhancements were simulated for NP dimers composed of two triangular prisms, arranged in either tip-to-tip or head-to-tail orientations with 2 nm separations. Using the tip-to-tip (i.e., bowtie) design, a FE factor of 1340 has been experimentally demonstrated for single molecules. [55] For a bowtie with a 14 nm

gap between individual triangles, the maximum electric field intensity enhancement was simulated to be nearly 300, occurring at a wavelength of 820 nm.

The usage of far-field interactions between individual particles provides another means of achieving high electric field enhancements. Figure 8 illustrates the maximum enhancements for normally incident linearly polarized light caused by various rectangular Ag NP arrays with different interparticle distances. Individual particles are oblate spheroids with major and minor axis lengths of 120 nm and 75 nm, respectively, and the particles are embedded in a uniform refractive index of 1.5. [45] In the figure, the enhancements are depicted for two different sites, both at the outside boundary of the particles and between the particles. The highest enhancements occur at the collective plasmon resonances of the arrays. To calculate these field enhancements, only the component parallel to the polarization direction of the incident plane wave is considered. Based on Figure 8, these field enhancements can be argued to exhibit a complicated dependence on lattice spacing, as the material losses of Au do not exhibit a minimum at the resonance wavelength corresponding to the maximum enhancements (roughly 1000 nm). Moreover the localized surface plasmon resonance of individual particles, occurring at approximately 600 nm, is markedly blue-shifted with respect to the the maximum enhancement wavelength.

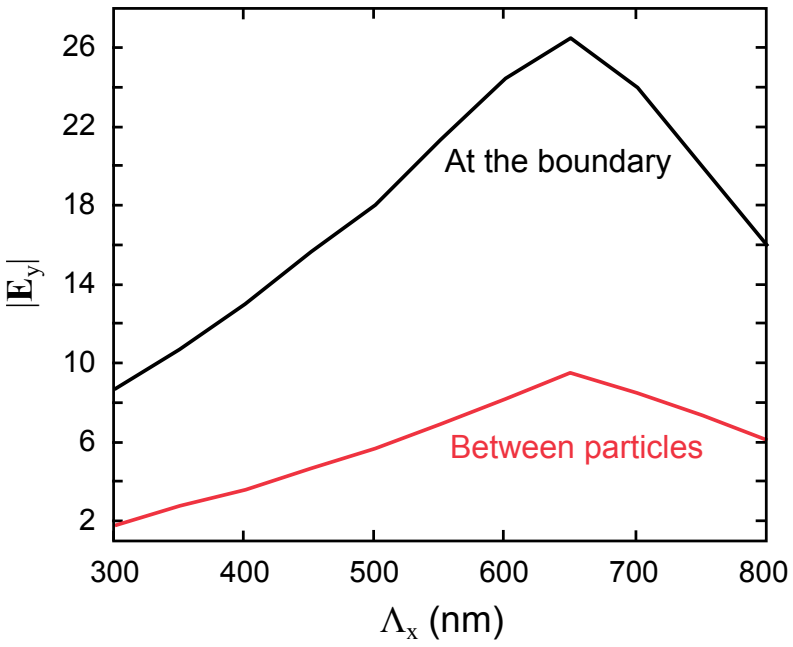

Figure 8: Magnification of the electric field y-component $\mathbf{E}_y$ in rectangular gold nanoparticle arrays with different lattice constants Λ_x in the direction orthogonal to the polarization direction of a normally incident plane wave. The values at two different locations are depicted. Figure re-drawn based on Ref. [45].

When metal NPs are used for FE, a clear distinction should be made between single-molecule and ensemble measurements. For single molecule measurements, maximum field enhancement determines the maximum FEs measurable from a particular system. However, in the case of ensemble experiments, measured fluorescence

intensities depend on the average intensity experienced by individual molecules. In this thesis, all experimental data is based on ensemble measurements. Consequently, simulation results stress the importance of average intensities in favour of maximum intensities (see Section 4.3). In particular, the average field enhancements on the surfaces of simulated NP arrays are used for determining the suitability of the arrays for FE.

To emphasize the effect of averaging, Figure 9 depicts the calculated electric field intensity enhancements of two Ag NPs at different positions along the surface of the particles. In the figure, line (b) corresponds to a prolate spheroid with major and minor semi-axis lengths of 50 nm and 25 nm, respectively, illuminated by a linearly polarized plane wave with its polarization vector parallel to the major axis of the spheroid. In such a case, a maximum intensity enhancement of roughly 1500 occurs at the tip of the particle. However, the field enhancements at other sites along the surface of the particle are considerably more modest, resulting in an surface-averaged intensity enhancement of only 256.

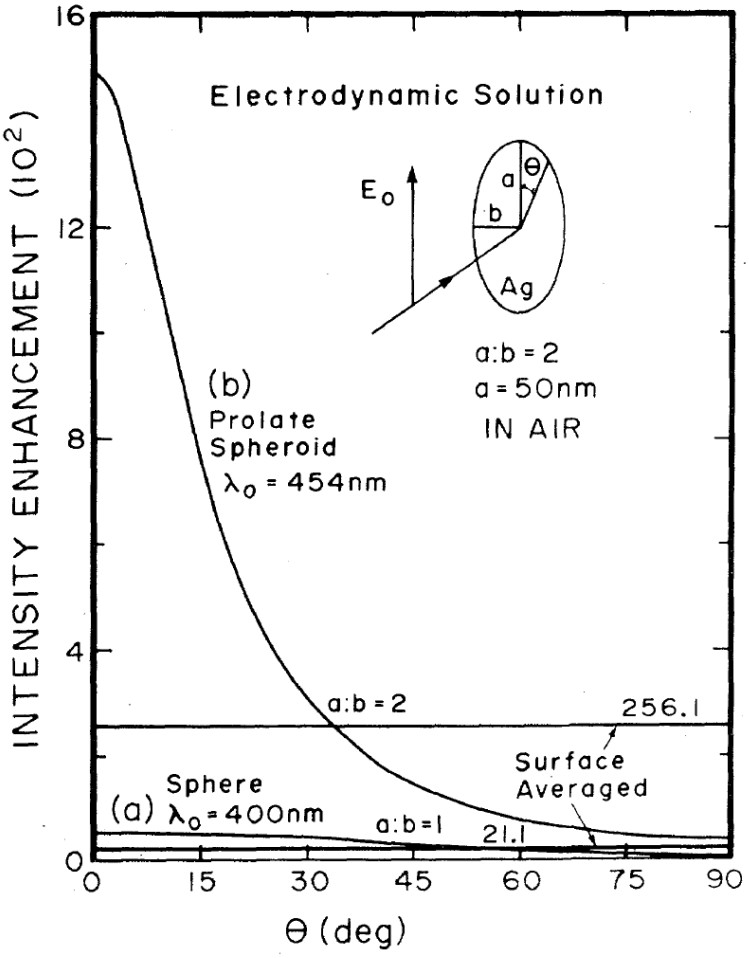

Figure 9: The angular spectrum for the magnification of the electric field intensity on the surface of (a) a spherical and (b) a prolate silver nanoparticle. Surface averaged values are also depicted. Figure reproduced from Ref. [56].

3 Plasmon-enhanced fluorescence

The preceding chapter discussed the optical properties of plasmonic NP arrays. In this thesis, such arrays are used to enhance the light emission efficiency of organic molecules. In the vicinity of plasmonic particles, the amount of light emitted by a molecule is changed both due to a change in the absorption and emission rates of the molecules. In order to provide a theoretical description of these effects, this chapter opens with a generalized picture of transition rates in a quantum system, based on time-dependent perturbation theory. Then, Section 3.2 presents the energy levels and electronic transitions of fluorophores, using molecular orbital formalism, and Section 3.3 describes effects causes by interactions of the molecules with their environment. Finally, Sections 3.4–3.6 discuss the effects of noble metal NPs on the light absorbed and emitted by organic molecules.

3.1 Transition rates between states

In this section, factors affecting the transition rate of a quantum system between two quantized states will be presented starting from a simplified picture of time-dependent perturbation theory. The following discussion loosely follows the treatment by Griffiths. [57]

The dynamics of a quantum system is described by the time-dependent Schrödinger equation

$$\hat{H}\Psi = i\hbar\frac{\partial\Psi}{\partial t}, \tag{19}$$

where $\hbar$ is the reduced Planck's constant and Ψ is the (time-dependent) wave function of the particle. Now suppose that the Hamiltonian $\hat{H}$ of a quantum system can be expressed as

$$\hat{H} = \hat{H}_0 + \hat{H}', \tag{20}$$

where $\hat{H}_0$ is an (unperturbed) Hamiltonian operator with known eigenfunctions ψ_n with eigenvalues E_n and $\hat{H}'$ is an additional term used to describe a time-dependent perturbation of the studied system. Let's try to look for possible wave functions Ψ of the form

$$\Psi\left(t\right) = \sum_n c_n\left(t\right)\psi_n e^{-iE_n t/\hbar}. \tag{21}$$

One only has to be able to deduce c_n as all other parameters are assumed to be known. Substitution of the above expression into Equation 19 leads to

$$\sum_n c_n E_n \psi_n e^{-iE_n t/\hbar} + \sum_n c_n \hat{H}'\psi_n e^{-iE_n t/\hbar} = i\hbar\frac{\partial}{\partial t}\left(\sum_n c_n \psi_n e^{-iE_n t/\hbar}\right), \tag{22}$$

where we have also made use of Equation 20 and the linearity of the operators $\hat{H}_0$ and $\hat{H}'$. Due to the orthonormality of the time-independent wave functions ψ_n, taking the left inner product with the bra vector $\langle\psi_k|$ then yields

$$c_k E_k e^{-iE_k t/\hbar} + \sum_n \left\langle \psi_k | \hat{H}' | \psi_n \right\rangle c_n e^{-iE_n t/\hbar} = i\hbar \frac{\partial}{\partial t} \left(c_k e^{-iE_k t/\hbar} \right). \tag{23}$$

By utilizing the product rule for the derivative on the right-hand side and the definition of matrix elements on the left, one ends up with

$$\sum_n \hat{H}'_{kn} c_n e^{i(E_k - E_n)t/\hbar} = i\hbar \frac{\partial}{\partial t} c_k. \tag{24}$$

If the perturbation represented by $\hat{H}'$ is relatively minor, Equation 24 can be solved for c_k by successive approximations. [57] Furthermore, if some 'zeroth order' approximation $c_k^{(0)}$ for c_k can be deduced, any higher-order approximation can be calculated using a recursive formula:

$$\sum_n \hat{H}'_{kn} c_n^{(p)}(t) e^{i(E_k - E_n)t/\hbar} = i\hbar \frac{\partial}{\partial t} c_k^{(p+1)}(t). \tag{25}$$

Let's assume that the system is initially in some state ψ_m so that $c_n^{(0)}(t) = \delta_{nm}$, where δ_{nm} is the Kronecker delta function. Equation 25 then yields a first order approximation for c_k as

$$c_k^{(1)}(t) = -\frac{i}{\hbar} \int_0^t \hat{H}'_{km}(t') e^{i(E_k - E_n)t'/\hbar} dt'. \tag{26}$$

In the context of the present work it is natural to select a sinusoidal time dependence for the perturbation. Therefore, $\hat{H}'$ is re-written as $\hat{H}'(\mathbf{r}, t) = 2V(\mathbf{r})\cos(\omega t)$ so that

$$\hat{H}'_{km} = \langle\psi_k|2V|\psi_m\rangle \cos(\omega t) = 2V_{km}\cos(\omega t). \tag{27}$$

Consequently, Equation 26 can be written as

$$\begin{aligned} c_k^{(1)}(t) &= -\frac{2iV_{km}}{\hbar} \int_0^t \cos(\omega t') e^{i(E_k - E_n)t'/\hbar} dt' \\ &= -\frac{iV_{km}}{\hbar} \int_0^t \left(e^{i(\omega_0 + \omega)t'} + e^{i(\omega_0 - \omega)t'} \right) dt' \\ &= -\frac{V_{km}}{\hbar} \left(\frac{e^{i(\omega_0 + \omega)t} - 1}{\omega_0 + \omega} + \frac{e^{i(\omega_0 - \omega)t} - 1}{\omega_0 - \omega} \right), \end{aligned} \tag{28}$$

where the resonance frequency ω_0 is defined as $\omega_0 = (E_k - E_m)/\hbar$. One is usually mostly interested in the response of the system at frequencies near ω_0. For optical frequencies, $\omega_0 \approx \omega \gg 1$, and the right-most term in the above expression clearly dominates. $c_k^{(1)}(t)$ can then approximated further by dropping out the sum frequency

term, and the probability $P_{m\to k}(t)$ that the studied system is in state ψ_k after having started out from state ψ_m is roughly given by

$$P_{m\to k}(t) = |c_k(t)|^2 = \frac{4|V_{km}|^2}{\hbar^2}\frac{\sin^2[(\omega_0-\omega)t/2]}{(\omega_0-\omega)^2}. \tag{29}$$

From a practical point of view, it is more useful to come up with an expression for the net transition probability $P^{tot}_{m\to k}(t)$ to states with energies close to the energy of state k. An approximate result can be obtained by naming the number of states to which transitions can occur per unit angular frequency interval near ω as the density of states $\varrho(\omega)$. Then, the number of possible final states dn in an infinitesimal frequency band $d\omega$ is given by

$$dn = \varrho(\omega)\, d\omega. \tag{30}$$

Let's further take the width of the studied energy band as corresponding to an angular frequency interval $\Delta\omega \equiv (E_{max} - E_{min})/\hbar$. With the given assumptions, the net transition probability $P^{tot}_{m\to k}(t)$ can be written in an integral form as

$$\begin{aligned} P^{tot}_{m\to k}(t) &= \int_{\omega_0-\Delta\omega/2}^{\omega_0+\Delta\omega/2} P_{m\to k}(t)\,\varrho(\omega)\, d\omega \\ &= \int_{\omega_0-\Delta\omega/2}^{\omega_0+\Delta\omega/2} \frac{4|V_{km}|^2}{\hbar^2}\frac{\sin^2[(\omega_0-\omega)t/2]}{(\omega_0-\omega)^2}\varrho(\omega)\, d\omega. \end{aligned} \tag{31}$$

If one further assumes $\varrho(\omega)$ to vary smoothly as a function of ω, the last expression can be approximately re-written as

$$P^{tot}_{m\to k}(t) \approx \frac{4|V_{km}|^2}{\hbar^2}\varrho(\omega_0)\int_{\omega_0-\Delta\omega/2}^{\omega_0+\Delta\omega/2}\frac{\sin^2[(\omega_0-\omega)t/2]}{(\omega_0-\omega)^2}d\omega \tag{32}$$

Following a suitable change of variables, the integral in the above expression can be evaluated roughly as $\pi t/2$ so that the transition probability $P^{tot}_{m\to k}(t)$ is then given by

$$P^{tot}_{m\to k}(t) = \frac{2\pi}{\hbar^2}|V_{km}|^2\,\varrho(\omega_0)\, t. \tag{33}$$

The aim of the present discussion was to identify factors that affect the transition rate $\Gamma^{tot}_{m\to k}(t) = dP^{tot}_{m\to k}(t)/dt$. One can now arrive at the conclusion that

$$\Gamma^{tot}_{m\to k}(t) \propto |V_{km}|^2\,\varrho(\omega_0). \tag{34}$$

In other words, the transition rate of a quantum system is determined by the 'magnitude' of the perturbation and the final density of states. The focus of the present work is to study the spontaneous radiative emission rates of organic molecules. In such a case, it is the density of photon states in the vicinity of the molecule that determines the emission rate.

When describing the interaction between light and an organic molecule, the perturbation $\hat{H}'$ is often presented in a semi-classical form so that particles with mass are considered as quantum objects whereas light is treated as a classical wave. In such a scheme, a multitude of different interaction types arise. The strongest interaction type is usually the so-called electric dipole interaction in which the perturbation is caused by the interaction of the electric field component $\mathbf{E}$ of the incoming light and the electric dipole moment $\mathbf{p}$ of the molecule. For the electric dipole interaction, the matrix element V_{km} can be written as

$$V_{km} = -\mu_{km} \cdot \mathbf{E}, \tag{35}$$

where the strength of the dipole moment μ_{km} of the transition is given by $\mu_{km} = -e \langle \psi_k | \mathbf{r} | \psi_m \rangle$. Due to the odd $\mathbf{r}$ term in the definition of μ_{km}, the electric dipole interaction is strong only for transitions in which the parities of the starting state and the final state are different. It should also be noted that the spin quantum number S of the molecule should stay constant during a dipolar transition, as a photon does not interact with the spin of a molecule.

3.2 Energy levels and transitions in fluorophores

The preceding section identified the key factors that affect the transition rates in a quantum system. In the following, energy levels in organic molecules are discussed, and the selection rules mentioned in the previous section are used to describe transitions between electronic energy states in fluorescent organic molecules. Additionally, the light-emitting efficiency of organic molecules is quantified by introducing the concept of fluorescence quantum yield. For simplicity and brevity, some features of molecular energy levels and energy transfer processes are intentionally left out of this discussion. For a more in depth discussion, the reader is referred to Refs. [1] and [2].

The energy levels of organic molecules are usually described within the framework of the Born-Oppenheimer approximation, i.e., nuclei in the molecules are considered stationary, as electronic transitions occur considerably faster than the movement of nuclei. [58] Within this framework, the wavefunction of the electrons surrounding the nuclei needs to be solved in order to decipher the electronic energy states of the molecule. The electronic wavefunction (i.e., the structure of the electron cloud) in a many-electron molecule is commonly presented using a set of molecular orbitals. In this scheme, electrons are seen to occupy only a single molecular orbital at a time, and each molecular orbital can contain up to two electrons with opposite spins. Individual electrons are considered to be at higher or lower energy levels depending on the orbitals they occupy.

Different electronic energy states of the molecule are differentiated by the way in which electrons are distributed to the MOs. The lowest energy state S_0 (i.e., the ground state) of the molecule corresponds to electrons filling the orbitals with the lowest possible energies. The highest-energy orbital that is filled in the ground state is commonly referred to as the highest occupied molecular orbital (HOMO). [59] Similarly, the orbital without electrons in the ground state and with the lowest energy is

the lowest unoccupied molecular orbital (LUMO). Since the electronic ground states of most organic molecules are singlet states (i.e., the ground states have zero total spin) and only dipole-allowed transitions are considered in this thesis, triplet states with non-zero spin and intersystem crossing between states of different multiplicity are omitted in the following discussion (for more information, see Refs. [2, 1]).

The energy level scheme presented thus far has completely disregarded the movement of nuclei in the molecules. The quantized oscillations of nuclei are usually thought of as producing a vibrational fine-structure or sublevels for the electronic energy states. In this picture, each electronic state possesses one lowest vibrational sublevel corresponding to the minimum oscillation energy of the nuclei. Molecules readily relax to this lowest vibrational state by transferring energy to their surroundings. [1] This radiationless decay process called internal conversion is often relatively fast.

A photon incident on an organic molecule can promote a transition in the molecule just as it could do to any other quantum system. In light-sensitive molecules called chromophores, the photon energies needed to promote a transition from the ground electronic state to an excited state correspond to electromagnetic radiation in the visible part of the spectrum. In other words, the energy difference of the HOMO and LUMO corresponds to the photon energy of visible radiation, and the absorption of light by the molecule can promote an electron from the HOMO to the LUMO.

Figure 10 presents a situation in which an organic molecule is excited from its electronic ground state S_0 to some high-energy electronic state, due to the absorption of a photon. Following absorption, internal conversion rapidly releases any excess vibrational energy, and the molecule is left at the lowest vibrational sublevel of the excited electronic state S_1. At this point, the molecule has two relaxation mechanisms by which to decay back to the ground state: radiative decay (i.e., the emission of a photon) and non-radiative decay. In the present work, one only needs to consider radiative transitions in which the total spin of the molecule stays constant during the transition. Such a radiative transition is called fluorescence. As a result of the constant total spin, fluorescence is a dipole-allowed transition and inherently a relatively fast process. Fluorescent molecules (i.e., fluorophores) typically exhibit excited state lifetimes of the order of nanoseconds. [2] As a result of internal conversion, the photons emitted as fluorescence are generally of lower energy than the photons absorbed by the molecule, producing a red-shift (i.e., Stokes shift) in the fluorescence spectra of organic molecules compared to their absorption spectra. [59] The second relaxation mechanism, non-radiative decay, is similar to internal conversion: the excitation energy of the molecule is non-radiatively transferred to the vibration, rotation, and translation of the surrounding medium.

The extent to which different organic molecules emit light varies considerably. The probability that an excited molecule will fluoresce is often called the fluorescence quantum yield Q_f of the molecule. In general, a similar probability or quantum yield can be calculated for any energy transfer process whenever the energy transition rates in the studied quantum system are known. For the simple situation considered previously, the fluorescence quantum yield Q_f is given by the ratio of the fluorescence

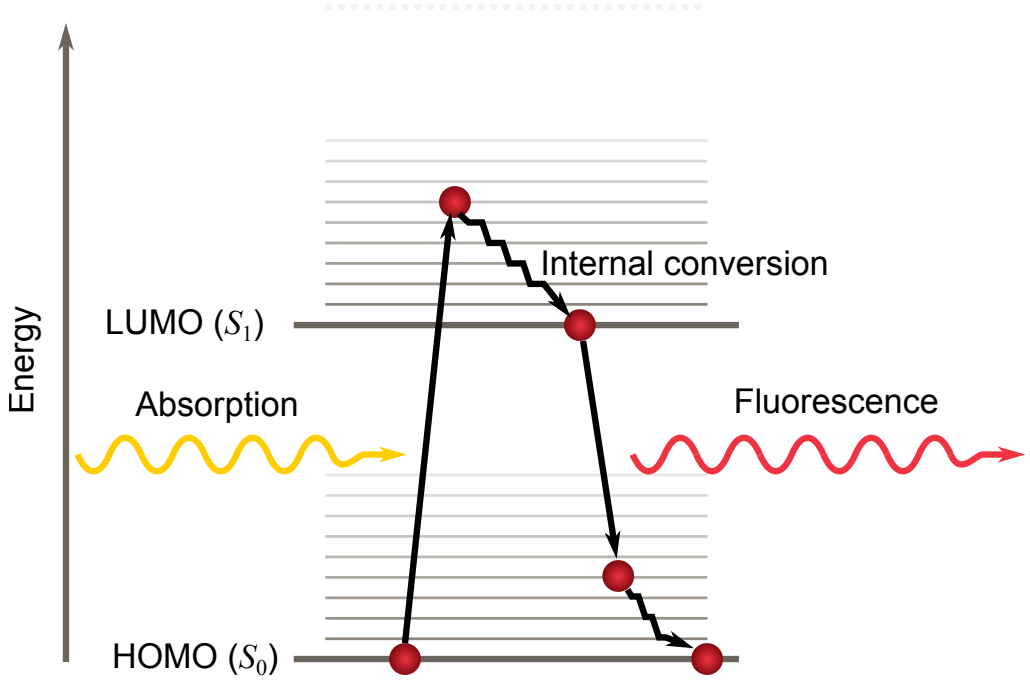

Figure 10: The physical processes leading to molecular fluorescence, starting from the absorption of a photon by the fluorophore. The vertical scale represents the energy of the molecule.

rate Γ_f to the total relaxation rate of the excited state S_1:

$$Q_f = \frac{\Gamma_f}{\Gamma_f + \Gamma_{nr}}, \tag{36}$$

where Γ_{nr} is used to denote the non-radiative decay rate of the molecule.

3.3 Intermolecular and environmental effects

The fact that the energy levels of a quantum system are discrete, i.e. non-continuous, suggests that radiation emitted in molecular transitions should be either monochromatic or contain only a finite set of distinct wavelengths. The fluorescence spectrum of a collection of molecules is, however, composed of a continuum of wavelengths, due to natural line broadening and because the energy levels and transitions in an individual molecule are influenced by the local environment of the molecule. After introducing the concept of natural line broadening, the remainder of this section will describe three different environmental effects that produce broadening in fluorescence spectra: interactions and energy transfer of the molecules with their surroundings, as well the aggregation tendency of identical molecules.

Natural line broadening (i.e., lifetime broadening) is usually explained in terms of the well-known energy-time uncertainty principle: [16]

$$\Delta E \Delta t \gtrsim \hbar. \tag{37}$$

The finite lifetime τ of any excited state can be shown to produce a spectral line with a full width at half maximum, FWHM, of

$$\mathrm{FWHM} = \frac{1}{\tau}, \tag{38}$$

Lifetime broadening is intrinsic to the transition and it cannot be completely avoided. However, the linewidth of a molecular transition decreases, if the lifetime of the excited state increases.

In general, all particles (e.g., electrons and nuclei) experience constant mutual interactions. In the language of quantum mechanics, these interactions produce additional terms in the Hamiltonians of studied quantum systems, i.e., they alter the quantized energy levels of these systems. If a collection of identical fluorophores are placed in a heterogeneous environment, the interaction terms of individual molecules vary, resulting in a broadening of the average fluorescence spectrum of the entire set of molecules.

Compared to isolated molecules, the environment of a fluorophore can also affect its transition rates or introduce altogether new energy transfer mechanisms. Naturally, the non-radiative relaxation rate of a molecule is dependent on the environment of the molecule, as fluorophores relax non-radiatively by transferring their excitation energy to their surroundings. Consequently, the fluorescence quantum yield of a fluorophore varies in different environments. As the non-radiative decay rates of organic molecules are generally higher in the solid state than in the liquid state [16], broadened fluorescence spectra and lowered fluorescence quantum yields should be expected in the solid state. In the present work, organic molecules are deposited onto solid substrates (see Section 4.2), justifying a similar prediction.

The excitation energy of a fluorescent molecule can also be directly transferred to the electronic excitation of a second molecule in a process known as resonance energy transfer (RET). Although a more general description of RET can be provided by quantum electrodynamics [60], RET is usually described using approximate equations that can be derived semi-classically and apply only for short intermolecular distances. Adhering to the description given in Ref. [59], such a picture of RET will be qualitatively provided in the following.

Consider two fluorophores, A and B, placed a distance l apart. If a sinusoidally time-dependent electromagnetic field E is incident on A, an oscillating dipole moment μ_A is induced in its electron cloud. Then, the oscillating dipole moment on A induces in turn a second dipole moment μ_B on B. As a first approximation, the molecules are, therefore, represented by two dipole moments μ_A and μ_B with oscillation frequency ω determined by E. When the separation l of the molecules is small enough, the potential energy V_d of the dipole–dipole interaction between μ_A and μ_B can be written as

$$V_d \propto \frac{\mu_A \mu_B}{l^3}. \tag{39}$$

In accordance with Equation 34, the transition rate between two states is proportional to the square modulus of the perturbation matrix element between the states. In the case of RET from A to B, the starting state can be written as $\psi_{A^*}\psi_B$,

and the final state is designated by $\psi_A\psi_{B^*}$. The transition rate (i.e., the RET rate) Γ_{RET} is then given by

$$\Gamma_{RET} \propto \frac{1}{l^6} \langle \psi_A \psi_{B^*} | \mu_A \mu_B | \psi_{A^*} \psi_B \rangle^2 = \frac{1}{l^6} \langle \psi_A | \mu_A | \psi_{A^*} \rangle^2 \langle \psi_{B^*} | \mu_B | \psi_B \rangle^2 , \tag{40}$$

where $\langle \psi_A | \mu_A | \psi_{A^*} \rangle$ is the matrix element for the emission of a photon by A at frequency ω. Similarly, $\langle \psi_{B^*} | \mu_B | \psi_B \rangle$ is the matrix element for the absorption of a photon at frequency ω. As the absorption and emission spectra of organic molecules are relatively broad, Equation 40 is equivalent to stating that efficient RET requires sufficient overlap between the the fluorescence emission spectrum of the donor molecule, A, and the absorption spectrum of the acceptor, B. The energy transfer rate is also proportional to the inverse sixth power of the distance l between the two molecules. Consequently, RET is efficient only across short distances of the order of 10 nm [1]. Although the directions of μ_A and μ_B are omitted in Equation 39, the efficiency of RET is also highly dependent on the orientations of the two molecules with respect to each other. [59]

In the solvated state, organic molecules often interact with each other to form supramolecular aggregates. This aggregation tendency increases with increasing concentration. Aggregation can be mainly contributed to the non-covalent interactions of different functional groups and de-localized π-orbitals with each other and with their local environment. [59] Although notable exceptions exist [61], organic molecules generally aggregate into irregular structures with limited long-range order. As the intermolecular distances in aggregates are relatively short, efficient RET should be expected between individual molecules of molecular aggregates. Moreover, the decreased intermolecular distances increase the magnitude of the potential energy term V_d in Equation 39, resulting in significant spectral shifts in the absorption and emission spectra of aggregates compared to those of monomeric molecules. Based on these spectral shifts, aggregates are commonly divided into two groups: H-aggregates exhibit a blue-shift (i.e., hypsochromic shift), whereas J-aggregates (i.e., Jelley aggregates) feature red-shifted spectra. [62] These two types of spectral shifts can be explained by differences in the stacking of individual molecules in an aggregate, resulting in different transition dipole orientations between the molecules. [63]

In order to maximize fluorescence intensity of a collection of organic fluorophores, energy transfer rates and aggregation between the molecules should be kept relatively low. This reasoning is justified by the presence of defective fluorophores with low fluorescence quantum yields. If such defective fluorophores are able to receive the excitation energy of intact, correctly functioning fluorophores, they can act as energy sinks, turning a considerable portion of absorbed energy into heat and reducing the overall fluorescence intensity of the entire collection of fluorophores. [64] Moreover, H-aggregation has been shown to inhibit fluorescence also by increasing coupling of excitation energy to triplet states. [63] In this thesis, energy transfer and aggregation between fluorophores is minimized by using highly diluted solutions for the deposition of the fluorophores onto the studied Ag NP arrays (see Section 4.2).

Furthermore, the fluorophores used in this thesis are assumed to experience attractive interactions with the surface that they are deposited on, supposedly reducing their tendency to aggregate.

In addition to spontaneous aggregation, fluorescent molecules also exhibit photobleaching, i.e., they undergo chemical reactions induced by incident light. Although specific reaction mechanisms depend on the studied molecules, chemical reactions causing photobleaching can be roughly divided into two categories: reactions that involve only individual molecules (i.e., intramolecular reactions), such as dissociation and isomerization reactions, and those involving multiple molecular species (i.e., intermolecular reactions), such as electron transfer, addition, and abstraction reactions. [59] Being clearly disadvantageous for fluorescence, photobleaching should be kept to a minimum when measuring the fluorescence intensities of organic molecules. In this thesis, photobleaching is reduced by utilizing low-intensity light, short exposure times, and low molecular concentrations.

3.4 Absorption rate enhancement

Having introduced the basic optical properties of organic molecules, this chapter will now move on to study the changes in absorption and emission rates caused by the proximity of plasmonic NPs. First, this section introduces the concept of absorption enhancement factor that will be essential in the determination of suitable array designs for FE. Section 3.5 then describes the fluorescence emission rate enhancement induced by noble metal NPs, and Section 3.6 provides a supplementary picture of the absorption and emission rate enhancements using an energy transfer formalism.

The rate at which a collection of molecules absorbs photons from an incident beam of light grows linearly with increasing light intensity. This is true whenever the intensity of incident light is low enough that at any given time most of the molecules are at their ground state. Since metal NPs can produce large local intensity variations (see Section 2.6), the absorption rates of fluorophores can be altered considerably by the proximity of plasmonic particles. In the vicinity of such particles, a single molecule experiences a fractional absorption rate change of

$$F_{abs} = \frac{|\mathbf{E}|^2}{|\mathbf{E}_0|^2} \frac{|\mu_{km} \cdot \mathbf{E}|^2}{|\mu_{km} \cdot \mathbf{E}_0|^2}, \tag{41}$$

where $\mathbf{E}$ and $\mathbf{E}_0$ refer to the field intensities at the location of the molecule with and without the NP, respectively. [8] In accordance with Equations 34 and 35, the amount of absorption enhancement depends on the mutual orientations of the electric field vectors $\mathbf{E}$ and $\mathbf{E}_0$ and the dipole moment μ_{km} of the studied molecule. One should note that the directions of $\mathbf{E}$ and $\mathbf{E}_0$ are generally not the same.

As mentioned previously, the model described above is strictly applicable only with very low light intensities. If the intensity of impinging radiation is increased beyond a specific threshold intensity (i.e., the saturation threshold), I_{sat}, the absorbance of a collection of molecules begins to saturate, as a considerable fraction of the molecules are in their excited states at any given moment. Due to the intensity-focusing effect of metal NPs, this saturation threshold is more easily exceeded if

molecules are placed in the vicinity of plasmonic particles resonant with the incident beam of light. By taking into account the saturation of organic molecules, the fractional absorption rate change experienced by a molecule in the presence of plasmonic NPs can be written as

$$F_{abs} = \frac{|\mathbf{E}|^2}{|\mathbf{E}_0|^2} \left(\frac{1 + |\mathbf{E}_0|^2 / |\mathbf{E}_{sat}|^2}{1 + |\mathbf{E}|^2 / |\mathbf{E}_{sat}|^2} \right) \frac{|\mu_{km} \cdot \mathbf{E}|^2}{|\mu_{km} \cdot \mathbf{E}_0|^2}, \tag{42}$$

where $|\mathbf{E}_{sat}|^2 \propto I_{sat}$. [8] For low intensities, Equations 41 and 42 yield the same results. However, for higher intensities, the absorption enhancement factor tends to unity, in accordance with the latter equation. When measuring FE, incident light intensity should, therefore, be kept reasonably low in order to inhibit the saturation of the studied fluorophores.

In the present work, fluorescence intensities are measured only for large collections of fluorophores. In each measured array, every NP is surrounded by a multitude of molecules with supposedly random orientations, and excitation intensity is kept to a minimum. In such a case, the orientational dependency of F_{abs} can be omitted, and changes in the total measured fluorescence intensity enhancements are proportional to the average intensity enhancement experienced by the fluorophores.

3.5 The Purcell effect

Thus far, the presented analysis has only considered changes in the absorption rates of molecules in the vicinity of metal NPs. It is, however, crucial to also take into account changes in light emission rates. Therefore, this section presents a perturbative theory for explaining the changes in the fluorescence emission rates of light-emitting molecules caused by plasmonic NPs.

From a quantum optics perspective, noble metal NPs can be treated as leaky cavities with low quality factors. [65] Let's therefore consider a fluorescent molecule that is placed inside a low-Q single-mode optical cavity. In other words, most of the cavity modes are assumed to be far from resonance, but one lossy mode is taken to coincide with the optical transition frequency of the molecule. Consequently, any photon inside the cavity can be absorbed by the molecule and photons emitted by the molecule can be trapped inside the cavity. However, photons emitted by the molecule into the cavity field quickly leak out of the resonator and the emission of photons is seen as an irreversible process. Such cavities are said to provide weak coupling between the cavity and the fluorophore. [8] The effect of these optical resonators on the emission of the fluorophores are relatively minor so that perturbative methods can be utilized to characterize these systems.

According to Equation 34, the emission rate of a fluorescent molecule is linearly dependent on the photon density of states $\varrho(\omega_0)$. In a finite volume V_0 of free space, the value of $\varrho(\omega_0)$ is

$$\varrho_{free}(\omega_0) = \frac{\omega_0^2 V_0}{\pi^2 c_0^3}, \tag{43}$$

where c_0 is the speed of light in vacuum. Furthermore, the matrix element V_{km} can be calculated using Equation 35. The spontaneous emission of photons can be thought of as being stimulated by an ever-present, fluctuating background electromagnetic field termed the vacuum field. Inside a cavity with volume V_0, the vacuum field magnitude $|\mathbf{E}_{vac}|$ can be shown to be [16]

$$|\mathbf{E}_{vac}| = \sqrt{\frac{\hbar\omega_0}{2\varepsilon_0 V_0}}. \tag{44}$$

where ε_0 is the vacuum permittivity. By averaging over all possible dipole orientations relative to this background field, one obtains an expression for the magnitude of the matrix element:

$$|V_{km}|^2 = \frac{1}{3}\mu_{km}^2 |\mathbf{E}_{vac}|^2 = \frac{\mu_{km}^2 \hbar\omega_0}{6\varepsilon_0 V_0}. \tag{45}$$

The emission rate Γ_{free} of the molecule in free space can then be written as

$$\Gamma_{free} = \frac{2\pi}{\hbar^2} |V_{km}|^2 \varrho_{free}(\omega_0) = \frac{\mu_{km}^2 \omega_0^3}{3\pi\varepsilon_0 \hbar c^3}. \tag{46}$$

When coupled to a lossy single-mode cavity, the emission rate of the same molecule is altered in comparison to the free-space value due to a change in $\varrho(\omega_0)$. At exact resonance (i.e., when the cavity resonance frequency exactly matches the emission frequency of the fluorophore) the density of cavity modes is [8]

$$\varrho(\omega_0) = \frac{2Q}{\pi\omega_0}. \tag{47}$$

Consequently, the fluorescence emission rate Γ_{cav} into an optical cavity with modal volume V_0 is given by

$$\Gamma_{cav} = \frac{2\mu_{km}^2 Q}{3\varepsilon_0 V_0 \hbar}. \tag{48}$$

Clearly, the fluorescence rate Γ_{cav} is different from the free-space value. This change in emission rate caused by the cavity is often called the Purcell effect in honor of E. M. Purcell, the first physicist to consider the spontaneous emission rate of a two-level quantum system inside a weakly coupled single-mode cavity. [66] Additionally, the ratio of cavity emission rate Γ_{cav} to free space emission rate Γ_{free} is often referred to as the Purcell factor F_P. For a closed cavity, F_P would simply be given by

$$F_P = \frac{\Gamma_{cav}}{\Gamma_{free}} = \frac{Q\lambda^3}{4\pi^2 V_0 n^3}, \tag{49}$$

where λ is the vacuum wavelength of fluorescence and n is the refractive index of the medium inside the optical resonator. An averaging identical to the one previously is done for transition dipole and electric field orientations. However, in the case of lossy cavities, one has to take into account that the fluorophores can also radiate into free-space modes. As a first approximation, the free-space emission of the molecules

can be considered to be unaffected by the NPs [8], resulting in a total Purcell factor of

$$F_P = \frac{\Gamma_{free} + \Gamma_{cav}}{\Gamma_{free}} = 1 + \frac{Q\lambda^3}{4\pi^2 V_0 n^3}. \tag{50}$$

A Purcell factor greater than unity clearly implies an enhancement in the spontanous emission rate. Furthermore, large Purcell factors are attainable with high-Q cavities and small modal volumes. However, in the discussion above, the resonance frequency of the optical resonator is assumed to be closely matched with the emission frequency of the fluorophore. Dissimilarity in the resonance frequencies of the cavity and the molecule may actually cause inhibition of spontaneous emission. As noble metal NPs are considered to act similarly to open cavities, Equation 49 can be used to qualitatively describe their effect on the emission rates of nearby resonant molecules. However, quantitative results are not easily obtained, as the modal volumes V_0 of open cavities are difficult to determine unambiguously. [15]

3.6 Energy transfer picture

The fluorescence intensity of organic molecules depends on their energy absorption rates and fluorescence emission rates, as described in Sections 3.4 and 3.5. In this section, the results of these previous sections will be combined and further elaborated. In this section, the energy transfer mechanisms in a weakly coupled system consisting of organic fluorophores placed onto a plasmonic NP are presented in order to determine critical factors influencing the fluorescence intensity of the fluorophores. Therefore, an approximate fluorescence quantum yield is calculated for fluorophores in the vicinity of a metal NP. The expression for the quantum yield will be interpreted in accordance with the radiative plasmon (RP) model of Lakowicz [67]. In order to simplify the following analysis, individual molecules are not considered to interact with each other or exhibit chemical reactivity. For convenience, energy transfer, aggregation, and photochemical reactions of the fluorophores are taken into account at a later stage.

Let's assume that a collection of organic fluorophores are placed in the proximity of a plasmonic NP and illuminated by monochromatic light with frequency corresponding to both the emission wavelength of the fluorophores and the LSPR frequency of the particles. If the absorption of photons induces plasmon oscillations in the NP, energy can be transferred from the particle to adjacent molecules through near field coupling. Although a plasmon resonance decays relatively rapidly, the amount of energy transferred to the molecules can be significant, as the extinction cross sections of NPs are considerably higher than those of organic fluorophores. This process was described in Section 3.4, based on the concept of local intensity magnification of incident radiation.

Consider then a situation such that some of the fluorophores are in their excited states, be it through direct absorption of incident photons or through their interaction with the near fields of the NP. Figure 11 depicts a schematic picture of the energy transfer processes present. The excited molecules can either fluoresce with

an energy transfer rate of Γ_r^m, relax non-radiatively at a rate Γ_{nr}^m, or excite plasmons in the NP with an energy transfer rate Γ_c. In the NP, plasmon oscillations can relax either radiatively at a rate Γ_r^p or non-radiatively, the rate of which is represented in the figure by Γ_{nr}^p.

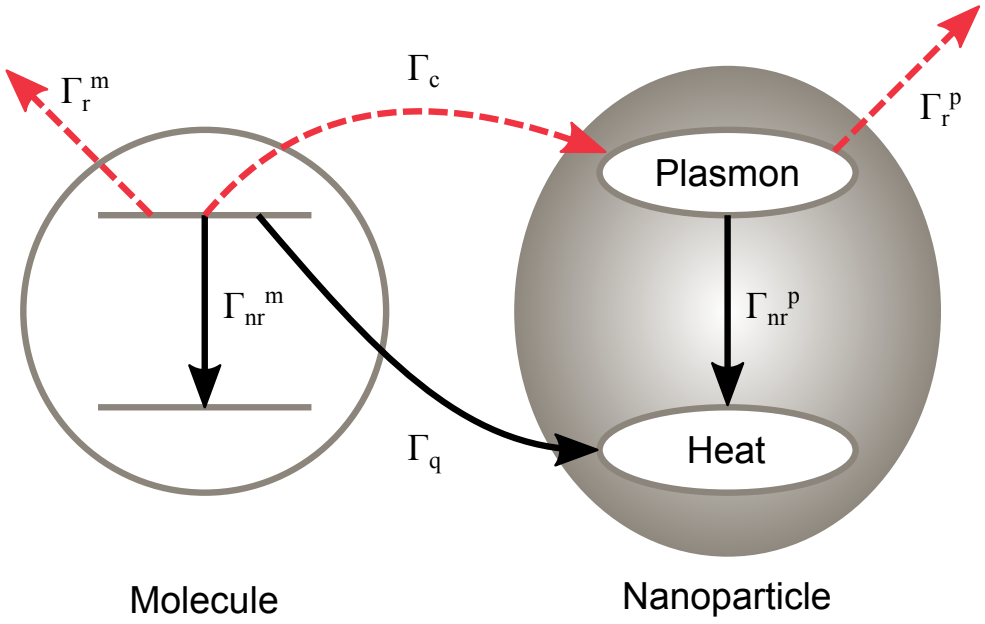

Figure 11: Schematic representation of the energy transfer processes involved in plasmon enhanced fluorescence. Processes that result in lowered fluorescence intensities are depicted in black, and processes favorable to fluorescence enhancement are diplayed in red. Figure drawn based on [8].

The NP can also quench the excited states of the fluorophores. Following the terminology presented in [8], quenching in this thesis refers mainly to the loss of energy by direct coupling of the excited states of the fluorophores to single-electron excitations in metal NPs and direct charge transfer between fluorophores and plasmonic particles. Quenching rates become significant whenever excited molecules are situated less than roughly 10 nm apart from the surface of an NP [68]. Therefore, in order to enhance the fluorescence intensity of the molecules, it is beneficial to provide a dielectric spacer between the NPs and the molecules. In the present work, a thin coating of aluminum oxide and silicon oxide is placed onto the particles (see Section 4.1) to reduce fluorescence quenching. The oxide layer also acts as an oxidation barrier, protecting the chemically reactive Ag NPs.

The energy transfer scheme presented in Figure 11 provides an approximate expression for the effective fluorescence rate and fluorescence quantum yield of the molecules in the presence of the NP. The total relaxation rate Γ_{tot} of the molecules is simply given by the sum of their individual relaxation rates:

$$\Gamma_{tot} = \Gamma_r^m + \Gamma_{nr}^m + \Gamma_c + \Gamma_q. \tag{51}$$

The radiative and non-radiative relaxation rates Γ_r^m and Γ_{nr}^m are considered to remain approximately constant with and without the NPs. [8]

The coupled system of excited fluorophores and plasmonic NPs can radiate to the far field either through direct fluorescence of the molecules or via the scattering of the NPs. [67] Therefore, the total radiative rate Γ_r of the coupled system is the sum of the direct fluorescence rate of the fluorophores and the plasmon generation rate Γ_c multiplied by the radiation quantum yield of the NP:

$$\Gamma_r = \Gamma_r^m + \Gamma_c \frac{\Gamma_r^p}{\Gamma_r^p + \Gamma_{nr}^p}. \tag{52}$$

In the above expression, the reverse transfer of energy from the NP back to the molecules is omitted owing to the swift relaxation rates of plasmon oscillations. Similarly to the simple case presented in Section 3.2, the fluorescence quantum yield Q_f of the coupled system is given by

$$Q_f = \frac{\Gamma_r}{\Gamma_{tot}} = \frac{\Gamma_r^m}{\Gamma_{tot}} + \frac{\Gamma_c}{\Gamma_{tot}} \frac{\Gamma_r^p}{\Gamma_r^p + \Gamma_{nr}^p}. \tag{53}$$

The fluorescence quantum yield of the molecules can be either increased or decreased by the presence of the NP depending on the values of the individual energy transfer rates. In particular, the effect of the NP is expected to depend on the fluorescence quantum yield of the molecules in the absence of the NP. [67] If this intrinsic quantum yield is high, the coupling rates Γ_c and Γ_q can only decrease the value of the total quantum yield relative to the intrinsic one. However, if the intrinsic quantum yield of the molecules is low, efficient coupling of the excited molecules to plasmon oscillations can enhance the overall radiative quantum yield, provided that the plasmon mode in question couples efficiently to the far field. Additionally, in the case of a high coupling rate Γ_c, the angular distribution (i.e., the far field radiation pattern) of fluorescence can be altered to resemble that of the NP. [69]

In the literature, a wide range of numerical values have been reported for experimentally measured FE factors. In an article by Tam et al. [70], an average enhancement factor of more than 50 was measured using indocyanine green molecules and Au nanospheres. Furthermore, enhancement factors of the order of 100 have been demonstrated with cyanine dyes coupled to periodic arrays of Ag NPs. However, considerably lower values of 3.5, 8, and 10 have also been presented in the case of ellipsoidal [9], triangular [71], and spherical [72] plasmonic NPs, respectively. This order of magnitude difference can be partially explained by the fluorescence quantum yields of the fluorophores used in these experiments, i.e., highest enhancements are usually attained with poorly emitting fluorophores.

As mentioned previously, the above discussion follows the RP model of Lakowicz [67]. This is not, however, the only luminescence enhancement model presented in the literature. For example, it has been proposed that higher-order resonances (e.g., quadrupole resonances) of plasmonic particles should be treated as inherently disadvantageous for FE. [73] However, such a simplified model does not account for the radiative relaxation of higher-order modes, induced by dynamic depolarization,

non-sphericity of the particles [74], a non-symmetric environment [75], or coupling of multipolar modes with dipole resonances [8] (see Sections 2.3–2.4).

The discussion above does not account for photobleaching, aggregation, or RET between the molecules. To first approximation, the effect of these additional factors can be considered by setting $\Gamma_{nr} = \Gamma_{nr}^{i} + \Gamma_{pcr} + \Gamma_{RET}$, where Γ_{nr}^{i} is the intrinsic non-radiative rate of the fluorophores, Γ_{pcr} is the rate at which excitation energy is directed to the photochemical degradation of the fluorophores, and Γ_{RET} is the rate of energy transfer between the molecules (see Section 3.3). This simple substitution does not, however, take into account the cumulative effect of photobleaching. In reality, Γ_{pcr} is assumed to produce an intensity-, absorbance-, and concentration-dependent reduction in the fluorescence quantum yield of a collection of fluorophores.

In conclusion, the total fluorescence intensity of a collection of fluorophores depends on the average absorption enhancement, F_{abs}, and the average fluorescence rate enhancement (i.e., the Purcell factor, F_P) experienced by the fluorophores. When placed in the immediate vicinity of a plasmonic NP, these two factors are assumed to have different spectral profiles. It has been both predicted theoretically [76] and verified experimentally [77] that optimal FE is usually produced by NPs with plasmon resonances slightly red-shifted with respect to the fluorescence emission peak of the studied fluorophores. This simple rule can be used as a convenient starting point when designing NP arrays for FE. It should be stressed, however, that the effect of plasmonic NPs on the optical properties of fluorophores is not limited to absorption and emission enhancement. The emission spectra of molecular aggregates can also be shifted considerably due to efficient coupling to plasmonic particles [78], and strong coupling between fluorophores and NPs can even be used to inhibit photobleaching. [68] The latter effect can be explained by a simple reduction of the quantum yield of primary photochemical reductions for the fluorophores. [59] Additionally, plasmonic nanostructures can even influence the coupling between individual fluorophores. [79]

4 Materials and methods

The previous chapters have reviewed the theoretical background related to plasmon-enhanced fluorescence. In the following, a brief summary of the fabrication procedure is given in order to elucidate the choice of methodology in this thesis. However, this chapter mainly presents the simulation models built for predicting NP properties and describes the characterization methods used to determine the plasmonic response of fabricated NP arrays.

4.1 Nanofabrication procedure

This section provides a description of the azopolymer interference lithography (APIL) nanofabrication procedure used to produce the designed NP arrays. First, the structure and properties of azobenzene-containing polymers (i.e., azopolymers) are summarized, followed by a detailed process flow for fabricating Ag NPs on glass substrates. As will be elaborated further in the following, the fabrication method imposes a set of restrictions on achievable NP sizes and shapes, as well as particle arrangements. These restrictions will be pointed out, and some prospects for improving the procedure are also briefly introduced.

The nanofabrication process used in this thesis relies on the unusual opto-mechanical properties of amorphous azopolymer layers. The molecular structure of the particular azopolymer used for this thesis, poly(Disperse Red 1 acrylate) (i.e., pDR1a), is presented in Figure 12 below.

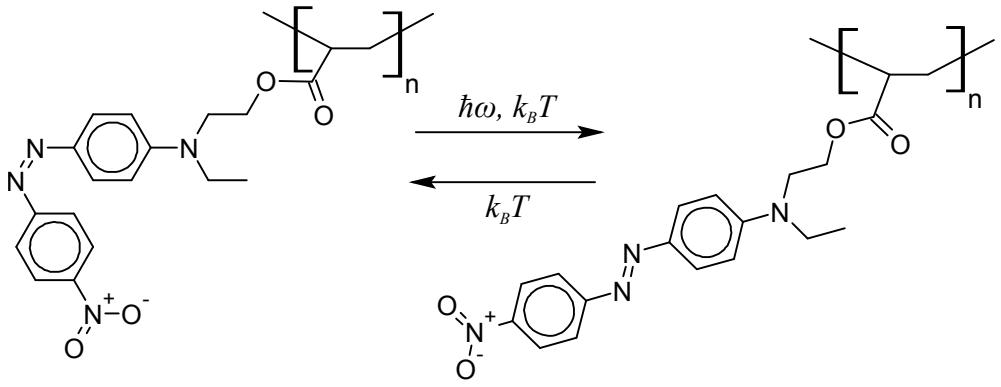

Figure 12: The two *cis–trans* isomers of poly(Disperse Red 1 acrylate).

When continuously excited using a suitable green-blue beam of light, the photo-responsive azobenzene side chains of pDR1a undergo repetitive molecular transformations, *cis–trans* isomerizations, which can produce mesoscopic and even macroscopic shape changes in the polymer. [80] Specifically, if only selected areas of an azopolymer layer are subjected to a light beam, the polymer has been shown to migrate from the illuminated to the dark areas. [81] By utilizing different spatial light intensity distributions, a multitude of different surface relief structures can then be formed onto the surface of the azopolymer layer. Sinusoidal surface relief gratings (SRGs) can, for example, be easily formed by subjecting the polymer to the intensity

pattern of two interfering plane waves of equal wavelength but different propagation directions. [82] As opposed to conventional photoresists, azopolymer surfaces can be exposed multiple times, allowing one to superimpose multiple gratings with varying grating constants and directions. [83] Previously, azopolymer-based nanofabrication schemes have been demonstrated for a variety of periodic nanostructures, including Au hole, disk, and stripe arrays [84], as well as silicon nanopillars and nanogrooves [85].

If a standard Lloyd mirror is used to produce a sinusoidal interference pattern on an azopolymer film, the periodicity Λ of the resulting SRG is given by

$$\Lambda = \frac{\lambda}{2 \sin \theta}, \tag{54}$$

where λ is the wavelength incident on the polymer film, and θ is the angle between the propagation direction of the incident light beam and the surface normal of the polymer film. [13] For the samples studied in this thesis, the 488 nm laser line of an argon ion (Ar^+) laser is used, resulting in practical minimum and maximum grating periods of roughly 250 nm and 1000 nm, respectively.

The APIL process flow for fabricating quasi-spherical Ag NPs is depicted graphically in Figure 13. First, 40 nm of Ag is evaporated using an electron beam evaporator, followed by a 20 nm layer of Au. The Au layer acts as both a diffusion barrier and a hard mask in ensuing process steps. Metallic adhesion layers are not used in the design, as such layers have been shown to adversely affect the FE capabilities of plasmonic structures. [86] Then, a thin film of pDR1a is spin coated on top of the Au layer. In order to produce a suitable SRG onto the azopolymer, the sample is exposed twice to the same sinusoidal interference pattern. Since the sample is rotated by 90° with respect to the interferometer between the two exposures, the surface of the azopolymer forms a sinusoidal 2D grating structure. The nanopatterned polymer layer is then etched using oxygen plasma until only the crests of the SRG are left covering the Au film. Following an extensive Ar milling step, the topography of the etched azopolymer layer is transferred to the metals — first to the Au layer, and then to the Ag underneath. Due to low etch selectivity between the azopolymer, Au, and Ag in Ar milling, the Ag structures produced by Ar milling resemble thin disks or metal sheets instead of spheres or ellipsoids. Therefore, an extra annealing step is used to convert the Ag into spherical particles.

Finally, the particles are coated with an oxygen diffusion barrier layer using atomic layer deposition (ALD). The ALD coating also acts as a spacer between the particles and the organic fluorophores that are deposited onto the particles at a later stage. Although ALD-deposited alumina layers have already been successfully utilized as dielectric spacers between plasmonic particles and fluorophores [9], the dielectric layers in this thesis are composed of two different materials: alumina and silica. The alumina layer alone would suffice also as an oxidation barrier; however, the silica layer needs to be added, as ALD-grown alumina was seen to slowly dissolve in water and the deposition of the fluorophores is done by immersion into an aqueous fluorophore solution (see Section 4.2).

The APIL-based process flow described above imposes three main restrictions

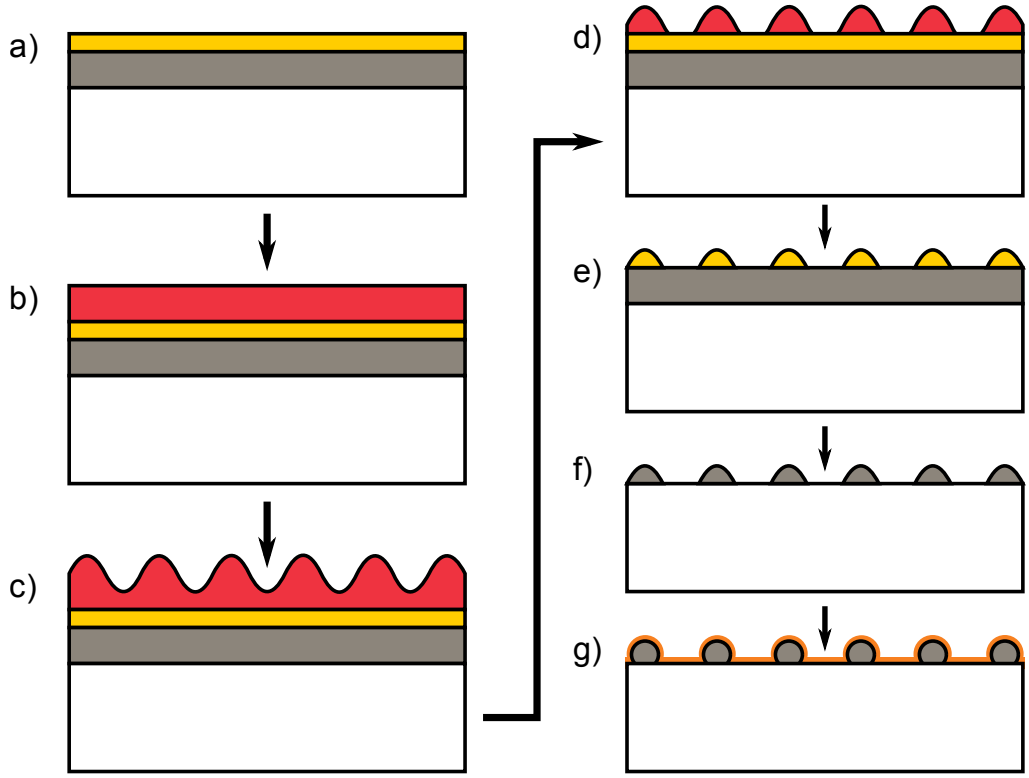

Figure 13: The seven main steps in fabricating silver nanoparticles on glass: a) evaporation of 40 nm of silver and 20 nm of gold on top of a glass substrate, b) spin coating a thin layer of the poly(Disperse Red 1 acrylate) azopolymer, c) exposure of a two-dimensional surface relief grating onto the azopolymer, d) dry etching of the azopolymer layer with oxygen plasma, e-f) argon milling of the gold and silver layers to form silver islands, as well as g) annealing and the deposition of a passivating dielectric coating.

on plasmonic NP arrays that can be fabricated: only nearly spherical particles can be formed, the particles have to be arranged in a rectangular lattice, and the NP sizes achievable increase with increasing interparticle distances. Spherical particles are assumed to result from the high-temperature annealing step that presumably melts the Ag islands produced via Ar milling. The second restriction, rectangular lattices, results from the 90° angle between the two exposures used to produce the 2D surface relief grating onto the azopolymer, while the third restriction is caused by the sinusoidal form of the surface relief grating.

4.2 Dip coating of fluorescent dyes

Dip coating is a method for depositing a thin liquid film onto the surface of a solid substrate by withdrawing the substrate out of a liquid bath. Naturally, the substrate surface has to be wetted by the liquid in question in order to achieve homogeneous deposition. In this thesis, organic fluorophores are deposited on the surfaces of the studied NP array samples by dip coating. This deposition method was

selected due to its relative simplicity and robustness, as well as the high deposition uniformity achievable using the method. This section first introduces the physics of the deposition method, and then continues by describing the specifics of the dip coating procedures used in this thesis. Finally, the characteristics of the two specific fluorophores used in this work are discussed, with an emphasis on their optical properties.

During dip coating, a substrate is generally withdrawn vertically from a liquid bath at a constant speed U_0 with the substrate surface oriented parallel to the withdrawal direction. [87] Due to the movement of the substrate, a liquid meniscus is formed on the substrate surface. This meniscus is usually thought of as being divided into two separate regions: an inner layer that moves along with the substrate, and an outer layer that returns to the liquid bath. [88] To illustrate this division, Figure 14 depicts the steady-state flow patterns during dip coating. Theoretically, the position of the streamline dividing the inner and outer layers of the meniscus (depicted in grey in the figure) defines the final thickness d of the liquid film deposited onto the substrate.

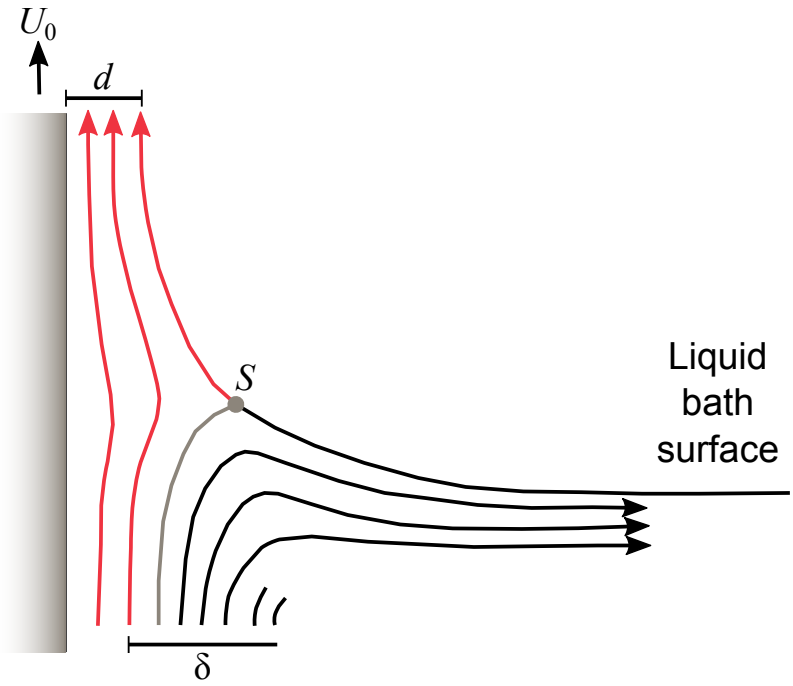

Figure 14: A schematic of the steady-state liquid flow patterns during dip coating. U_0 is the withdrawal speed of the substrate, and d is the thickness of the final liquid film. S and δ designate the stagnation point and the outer boundary layer of the liquid meniscus, respectively. Figure re-drawn based on Ref. [87].

In general, the position of the grey streamline in Figure 14 exhibits a relatively complicated dependence on a multitude of forces acting near the substrate surface. However, when the viscosity η of the liquid and the withdrawal speed U_0 are low enough not to affect the curvature of the meniscus, the entrained thickness d results from the balancing of the viscous drag, gravitational pull, and liquid-vapour surface

tension γ_{lv} experienced by the liquid. [87] Specifically, the thickness d can then be calculated from

$$d = 0.94 \frac{(\eta U_0)^{2/3}}{\gamma_{lv}^{1/6} (\rho g)^{1/2}}, \tag{55}$$

where ρ is the density of the liquid and g is the acceleration of gravity. [89]

In the present work, fluorescent molecules were deposited from de-ionized water (DIW) solutions with concentrations of 1 μM. Due to the relatively low concentrations used, the viscosities, densities, and surface tensions of these solutions are assumed to be well approximated by those of pure water. With a measured withdrawal speed of 0.25 mm/s, the resulting liquid film thickness can be estimated as 0.6 μm. If the concentration of the solvated molecules is assumed to stay constant within the liquid bath and the meniscus, the average molecule surface density on the substrate after drying is then approximately 0.4 μm^{-2}. If individual molecules were arranged in a close-packed hexagonal lattice, such a density would correspond to an average distance of roughly 1.5 μm between the molecules. This simple calculation does not, however, take into account interactions between the molecules and the substrate. For the fluorophores used in this thesis, such interactions are assumed to substantially increase the actual molecule surface density after deposition, as all coated samples were immersed for 60 s prior to withdrawal.

Continuing with the properties of the organic fluorophores used in the present work, Figures 15 and 16 present the molecular structures, as well as the absorbance and emission spectra of rhodamine 6G (R6G) cations and cascade blue (CB) acetyl azide, respectively. A derivative of xanthene, R6G is a common fluorescent dye that has been used extensively, for example, in dye lasers [90]. This fluorophore has been shown to exhibit a high fluorescence quantum yield (0.90-0.96) in a variety of solvents with peak wavelengths ranging from 563 nm to 568 nm. [91] In solvated form, R6G molecules have an excited state lifetime of roughly 4 ns. [92] On the other hand, CB is a water-soluble fluorescent molecule with an emission peak at a wavelength of roughly 420 nm that has been developed for use in multi-color fluorescence imaging. Compared to R6G, CB acetyl azide has attracted considerably less attention in the literature. Nevertheless, the usefulness of this molecule has been demonstrated, for example, in RET studies when combined with heme prosthetic groups. [93].

As described previously, fluorophores are deposited onto studied NP array samples by dip coating. In these array samples, the outermost layer is composed of ALD-grown silica. When immersed in DIW with a pH of 7, such silica layers are assumed to exhibit a negative net charge, as literature values for the isoelectric points of silica materials are usually of the order of 1.5–4 [94]. Due to their positively charged functional groups and de-localized π-electron clouds, both of the fluorophores presented previously are assumed to adsorb spontaneously onto the ALD-coated surfaces of the studied NP array samples. In the case of R6G, such adsorption has been studied at an interface between silica and water, and a bathochromic shift of 5 nm was observed in the fluorescence spectra of adsorbed molecules compared to solvated ones [95].

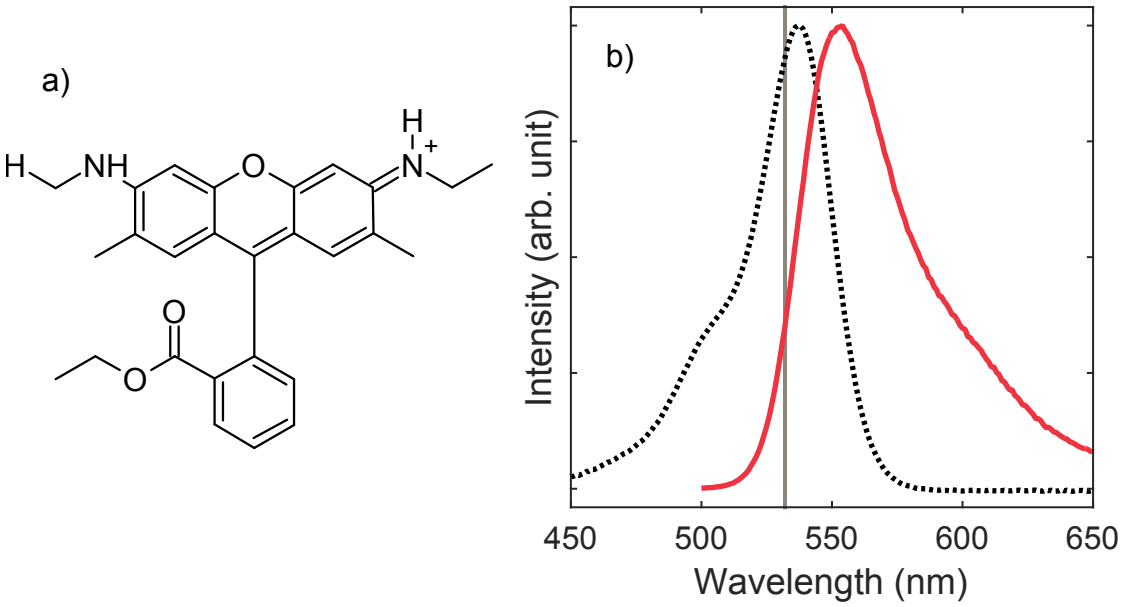

Figure 15: a) The molecular structure of rhodamine 6G, and b) the normalized absorbance (black dots) and fluorescence (red) spectra of 1 μM rhodamine 6G in de-ionized water. The grey vertical line depicts the excitation wavelength $\lambda_{exc} = 532$ nm used to excite rhodamine 6G in the confocal fluorescence measurements.

4.3 Finite element method simulations

This section introduces the numerical simulation method used in this thesis and describes the simulation models built to predict the optical properties of 2D Ag NP arrays. These simulation models can be used to study effects caused by variations in several device parameters, including material properties, NP size and shape, coating thickness, as well as distances between adjacent particles. However, the sizes of simulated arrays (i.e., the number of particles in the arrays) cannot be adjusted, as the models assume that each array consists of an infinite amount of identical NPs. In the present work, two sets of finite element method (FEM) simulation models are used: models built on a so-called scattered field formalism and those using a full-field formalism. The scattered field formalism is the main formalism utilized in this work, and the full-field simulations are used for validating the achieved results.

FEM is a general numerical method for solving boundary value problems governed by differential equations. This numerical method is characterized by three distinctive features: division of the studied model geometry to sub-domains called finite elements (i.e., meshing), approximating the properties of the studied system within these finite elements using simple interpolation functions, and assembly of the complete system response using continuity and known boundary conditions. [96] FEM is applicable to a wide range of problems, as it is capable of solving problems involving complicated model geometries, a variety of different boundary conditions, and non-linear responses. [97] Furthermore, adopting the method is simple due to

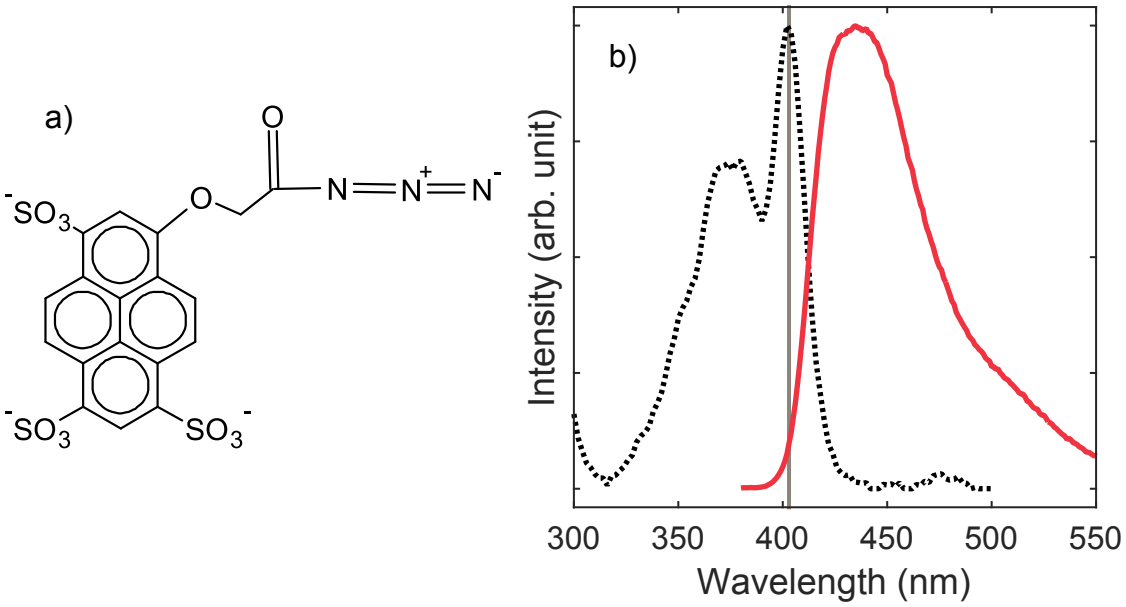

Figure 16: a)The molecular structure of cascade blue acetyl azide, and b) the normalized absorbance (black dots) and fluorescence (red) spectra of 1 μM cascade blue in de-ionized water. The grey vertical line depicts the excitation wavelength $\lambda_{exc} = 403$ nm used to excite cascade blue molecules in the confocal fluorescence measurements.

the existence of off-the-shelf FEM software packages, such as Comsol Multiphysics® developed by the Comsol Group.

Compared to other numerical differential equation formulations, such as the finite difference time-domain method, FEM has a relatively wide degree of flexibility regarding the geometry of simulated systems, as it can be used in conjunction with unstructured meshes. [97] Combining such unstructured meshes with the ability to approximate electromagnetic fields using continuous interpolation functions, FEM can be used to precisely simulate the electric near fields around realistically shaped plasmonic nanostructures. [98] In the present work, the geometry of a single NP array sample is determined by scanning electron microscopy (SEM) and atomic force microscopy (AFM) in order to realistically simulate the optical properties of the array.

In this thesis, Comsol Multiphysics (version number 5.0.0.244) is used to build a FEM model suitable for designing 2D Ag NP arrays on glass substrates. This simulation software package was selected, as the graphical user interface in Comsol facilitates both the model building process and the post-processing of simulation results. In Comsol, building a simulation model comprises six steps: defining the model geometry, specifying material parameters in the model, adding suitable boundary conditions, meshing, defining model parameters, and selecting the type of studies to be computed. The remainder of this section provides a detailed description of the simulation model used in this thesis.

The model geometry used in this work is schematically presented in Figure 17.

First, four cuboidal domains are added on top of each other to act as the superstrate (i.e., air) and substrate (i.e., glass) in the simulation, followed by the addition of a spherical domain coated with a uniform, thin coating domain. The center of this encapsulated sphere is placed above the substrate domains so that the sphere is still partially inside the substrate. Then, the sphere and the coating are truncated by removing the parts remaining inside the substrate. Though such geometries are presumed to resemble those obtained using the APIL-based fabrication process described in Section 4.1, the model geometry has been simplified to some extent. Specifically, the fabricated particles will not be entirely spherical, and the dielectric coating should be applied also on top of the substrate. However, the sphericity is not a strict requirement of the model geometry, and the sphere can be easily replaced by any spheroidal particle. Furthermore, the thin dielectric layer on top of the substrate is assumed to be reasonably insignificant to the optical properties of these Ag NP arrays.

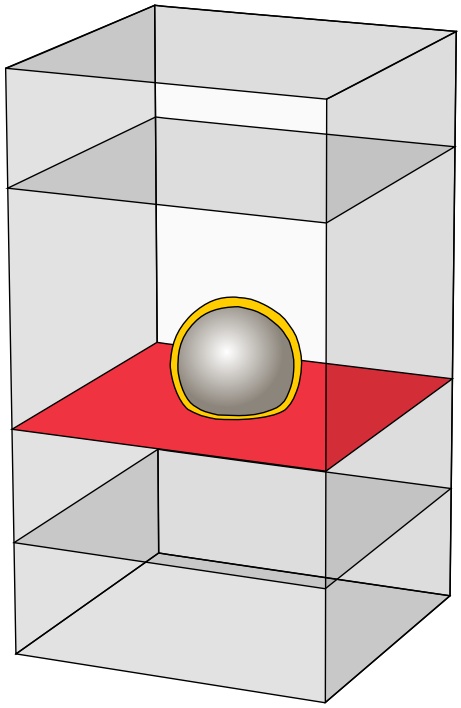

Figure 17: A schematic illustration of the silver nanoparticle array geometry used in the FEM model. The dielectric coating surrounding the particle is depicted in yellow, and the boundary between the substrate and superstrate domains is highlighted in red.

Once the model geometry has been defined accordingly, the material parameters of each of the domains are added to the simulation. Since FEM allows using arbitrary material properties, experimentally determined material parameters from Ref. [99] were used for the Ag NPs. Additionally, the top and bottom domains in Figure 17 are defined as perfectly matched layers (PML), i.e., they attenuate light efficiently. Defining these domains using such a formalism effectively extends the substrate and superstrate domains indefinitely. Since the built-in PMLs in Comsol cannot be used

in conjunction with absorbing materials, the superstrate and substrate are assumed to exhibit no losses, and their optical properties need to be presented using real-valued refractive indices $n_{air} = 1$ and $n_{sub} = 1.5$, respectively. Similar non-absorbing properties are also assumed to hold for the dielectric coating, simulated as a material with a refractive index n_c of 1.65. Supposedly, simplifying the optical properties of these three dielectric domains will result in minimal simulation error.

The fourth step in building the Comsol model, addition of boundary conditions, was already partly described, i.e., the PML domains are used to extend the substrate and superstrate in the vertical direction. Usage of a commercial FEM software package greatly facilitates the addition of boundary conditions, as Comsol automatically uses the material parameters of different domains to calculate the electromagnetic fields at the boundaries between adjacent materials. The next boundary condition that needs to be manually added is an excitation input port below the PML in the superstrate and an output port above the PML in the substrate. The excitation is defined as a plane wave normally incident on the substrate–superstrate boundary. In addition, the vertical sidewalls of the substrate and superstrate are designated with periodic (i.e., Floquet) boundary conditions. This turns the model geometry into a unit cell in an infinite 2D array of identical elements. Consequently, one can vary the spacing between neighbouring NPs in the simulated array by changing the horizontal dimensions of the model geometry.

Meshing is the fifth part in building a FEM model using Comsol. The meshing procedure used in the simulations begins by creating free triangular meshes on the outer surfaces of the geometry. Meshing of the outer surfaces utilizes copied meshes, since the Floquet boundary conditions on the vertical sidewalls require that the meshes of the vertical boundaries on opposite sides of the geometry are pair-wise identical. To reduce non-physical scattering caused by individual mesh elements, the meshing procedure introduces a mesh consisting of cuboidal elements in both PML domains. Other parts of the geometry are meshed using tetrahedral elements. In order to obtain sufficiently accurate numerical results, at least five second-order elements per wavelength were used in each medium.

All the results in this thesis are based on frequency domain studies. Time domain studies are not used, as the Floquet boundary conditions used in the simulation models are only applicable in the frequency domain. In order to properly calculate the near-fields and far-field extinction efficiencies of the particles, simulations based on the scattered field formalism are divided into two parts. First, a plane wave incident on the substrate–superstrate boundary is simulated in the absence of the NP. Then, the model calculates the field scattered by the coated NPs when excited by the incident plane wave. When running extensive parameter sweeps, the robustness of the computation is further improved by using direct (i.e., non-iterative) numerical solvers in the simulations and by setting Comsol to react to all encountered errors by saving empty dummy solutions and continuing with different simulation parameters.

The Comsol simulations are used to calculate approximate fluorescence enhancement figures of merit (FE-FOMs) for different NP array designs. The FE-FOMs were calculated based on two factors: scattering to absorption ratio, and average intensity magnification on the array surface. In this thesis, predictions on the ap-

plicability of different array designs is based on the assumption that the total FE of fluorophores placed onto different plasmonic arrays is approximately proportional to the FE-FOM:

$$\text{FE} = F_{abs}F_P \propto\!\!\!\approx \frac{I_p^{ave}}{I_0^{ave}}\left(1 + \frac{C_s}{C_{ext}}\right) = \text{FE-FOM}, \tag{56}$$

where I_p^{ave} and I_0^{ave} are the average incident light intensities on the surface of the simulated array with and without the coated NPs, respectively. Although the increased surface area of arrays with larger particles is also expected to increase measured fluorescence intensities, the effect of increased surface area was intentionally not taken into consideration. Detected fluorescence intensities in real measurements depend also on the directivity of fluorescence emission. Since the simulation model in its present form cannot predict the far-field emission patterns of simulated NP arrays, the directivity of fluorescence is not taken into account. Moreover, the above definition does not consider the coupling efficiency Γ_c between fluorophores (see Section 3.6) or the Stokes shift between the emission and absorption peaks of organic fluorophores (see Section 3.2).

Using the scattered field formalism, the average intensity magnification is readily determined by simple averaging of electric field intensities on the surfaces of the studied arrays with and without NPs. However, in order to calculate the scattering and extinction cross sections and efficiencies of an individual particle in the simulated arrays, two crucial model parameters need to be specified prior to simulations: the power scattered and absorbed by a single NP. The power absorbed by an NP is calculated by integrating the total power loss density given by the built-in Comsol variable Q_h over the volume of the particle, while the scattered power is determined by integrating the normal component of the scattered field on the outer boundary of the Ag NP. As described in Section 2.2, the cross sections can then be calculated by normalizing the absorbed and scattered powers by the intensity of the incident radiation, and the efficiencies are given by dividing these cross sections by the geometrical cross-sectional area of the simulated particle. Naturally, extinction cross sections and efficiencies are calculated by summing the corresponding scattering and absorption quantities.

For all theoretical work, verification of achieved results is crucial. Whenever possible, simulation results are verified by comparisons to analytical models. In the present case, however, achieving analytical results would be impractical due to the complexity of the simulated array geometries. Consequently, the results obtained using the scattered field formalism are compared to a second set of FEM simulations using a full-field formalism. In these simulations, the complete electromagnetic field is determined for the simulated array, i.e., the method makes no distinction between incident and scattered fields. Using this total field formulation, the extinction cross sections of simulated NP arrays are calculated based on the transmittance of normally incident light. To attain realistic results, all relevant diffraction orders of the arrays need to be explicitly specified using diffraction ports, making simulations with large interparticle separations very memory-intensive.

In the full-field verification models, absorption and scattering contributions to

extinction could be separated by determining the absorption cross sections similarly to the previous models, i.e., by direct integration of the built-in variable Q_h. However, electric field intensity magnifications had to be calculated differently. Using the total field formulation, the average local intensity $I_p^{ave} = \left\langle c_0 \varepsilon_0 n \left|\mathbf{E}\right|^2 / 2 \right\rangle$ was compared to the expected average intensity at the surface. Near the substrate surface, the average intensity I_0^{ave} can be approximately written as

$$I_0^{ave} = I_0 \left(1 - \frac{n_{sub} - n_{air}}{n_{sub} + n_{air}} \right)^{-2}, \tag{57}$$

where n_a and n_b are the refractive indices of the superstrate and substrate, respectively, and I_0 is the intensity of the incident beam. [100]

More precise classical models could also be built to study the fluorescence enhancing effect of NPs. The fluorecence enhancement of a molecule placed in the proximity of an NP could be determined numerically by simulating the molecule as a point dipole and calculating the total power radiated by the dipole with and without the NP. [8] A two-step simulation procedure could then be built to separately simulate the absorption and emission enhancements imposed by the particle. However, such a procedure would be computationally more demanding, requiring two-dimensional wavelength sweeping for both the absorption and emission wavelengths of a fluorophore. If multiple randomly oriented fluorophores are placed near an NP, such a model would also need to average the results of various molecular positions and orientations and polarization states of exciting light. In the case of single molecule measurements (for example, see Ref. [55]), such averaging is not required, facilitating the use of more precise simulation models.

4.4 Optical characterization

UV–Vis spectroscopy

The transmittance of ultraviolet (UV) and visible (Vis) radiation through a sample is measured using a UV–Vis spectrometer, also referred to as a UV–Vis spectrophotometer. Figure 18 depicts the structure of the PerkinElmer Lambda 950 UV–Vis spectrometer used in this work. In the instrument, a halogen lamp is used to produce light near the visible wavelength range, i.e., at wavelengths above roughly 320 nm. Although not shown in the figure, the wavelength range of the Lambda 950 instrument can also be extended further into the UV wavelength range by switching to a deuterium lamp. During normal operation, the light produced by one of these lamps is directed to two consecutive monochromators. In such a double-monochromator assembly, the exit slit of the first monochromator acts as the entrance slit of the second monochromator. By synchronously rotating the grating tables in these monochromators, different, narrow wavelength bands can be selectively passed through to the studied sample, allowing rapid recording of transmittance spectra.

After wavelength selection, the beam of light emerging from the exit slit of the second monochromator passes through a common beam mask. This mask can be used to tailor the height of the light beam incident on the studied sample. Once a

suitable beam height has been selected, the beam is divided in two by a rotating chopper wheel. One of these beams is directed to the measured sample, and the other one passes trough a reference sample. Consequently, the Lambda 950 can be classified as a double-beam spectrometer. Finally, the intensities of the two beams are measured by a photodetector. In the Lambda 950, two different detectors can be used: a photomultiplier tube (PMT) for wavelength in the UV–Vis wavelength range and a Peltier-cooled lead sulfide detector in the near-infrared (not shown in Figure 18). Due to the wavelength range of interest, only the PMT was used in the present work.

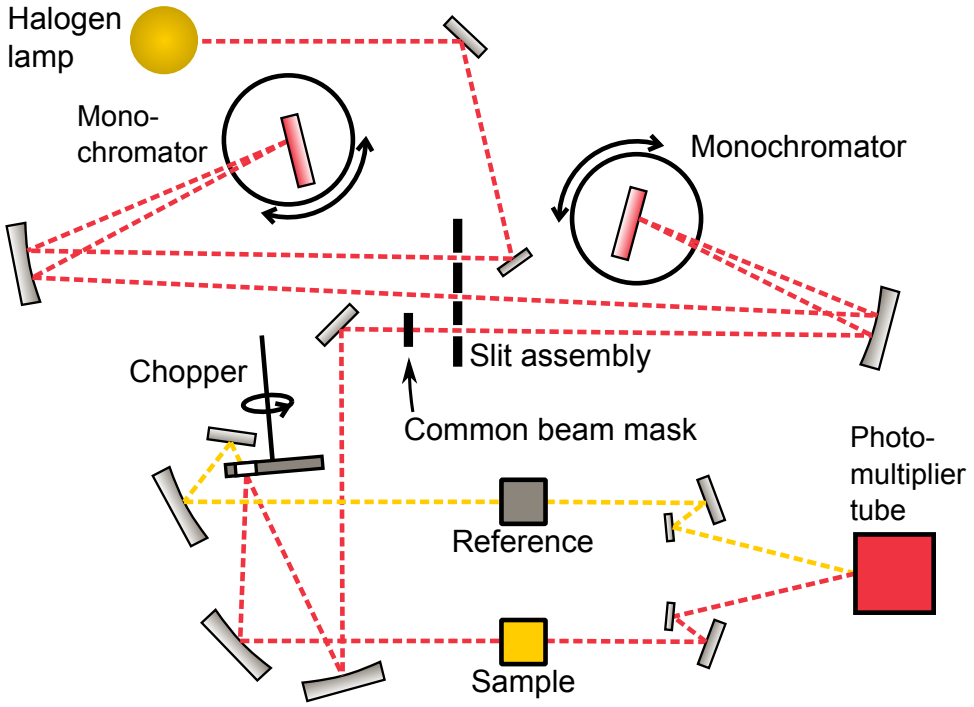

Figure 18: A schematic representation of the optical system in the PerkinElmer Lambda 950 UV–Vis spectrometer used for the absorbance and extinction measurements.

In a two-beam instrument, the transmittance T through the measured sample is calculated according to

$$T = \frac{I_s}{I_r}, \tag{58}$$

where I_s and I_r are the intensities of the sample and reference beams, respectively. For regular, 2D NP arrays, one can then calculate the average extinction cross-section C_{ext} per particle as

$$C_{ext} = (1 - T)\, A_{uc}^{\perp}, \tag{59}$$

where $A_{uc}^{\perp}$ is the area of a single unit cell of the array, projected onto a plane perpendicular to the propagation direction of incident light.

Alternatively, the transmittance T can be written in terms of the absorbance A:

$$A = -\log_{10}(T). \tag{60}$$

According to the Beer–Lambert law, the absorbance A of a beam of light travelling through a substance of thickness d can also be written as

$$A = \epsilon c d, \tag{61}$$

where c is the molar concentration of attenuating species with molar extinction coefficient ϵ in the substance. For highly absorbing samples, deviations from the Beer–Lambert law are expected, mainly due to experimental error caused by stray light. [101] Following a common convention, the absorption spectra of organic molecules presented in this thesis are expressed in terms of absorbances.

The UV–Vis spectrometer used in this thesis can alternatively be configured to measure the reflectance spectra of planar samples. Figure 19 illustrates the passage of light in the sample and reference paths when using this reflectance measurement configuration. As shown in the figure, the reflectance R of a sample is measured using an integrating sphere. The studied sample is placed in the rear sample holder, and a highly reflecting Spectralon plate is placed in the reference sample holder. In order to prevent specularly reflected light from escaping the sphere, light is incident onto the sample and the reference plate at an angle of 8°. The variable port placed at the specular reflectance angle can be opened or closed in order to measure either diffuse or total reflectance spectra, respectively. For scattering samples, diffuse reflectance is usually measured. Similarly to the transmission measurements described previously, the reflectance R of the sample is then calculated as

$$R = \frac{I_s}{I_r}. \tag{62}$$

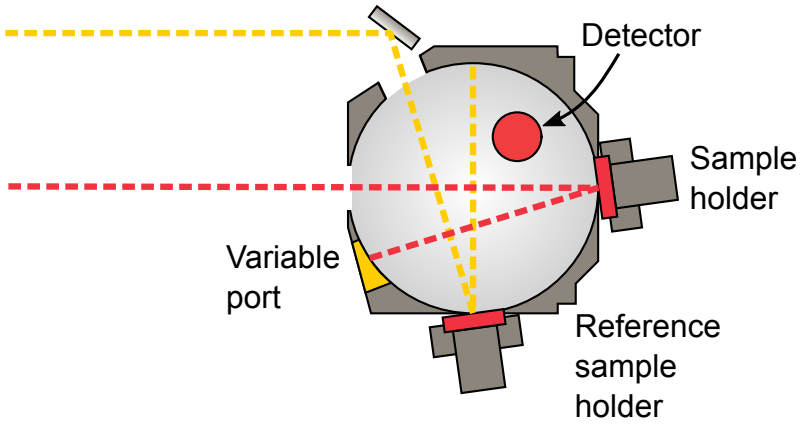

Figure 19: A schematic of the reflectance configuration in the PerkinElmer Lambda 950 UV–Vis spectrometer.

Fluorescence spectroscopy

A fluorometer, or spectrofluorometer, is the standard instrument for measuring the fluorescence spectra of organic fluorophores. Figure 20 shows a schematic of the Photon Technology International QuantaMaster 40 fluorometer used in this thesis. To measure fluorescence spectra, the studied sample is excited by a nearly monochromatic beam of light. The wavelength, λ_{exc}, of this excitation beam is selected to coincide with the absorption spectrum of the sample. In the QuantaMaster 40, light is first produced by a xenon lamp, and the excitation wavelength is chosen using two consecutive monochromators. Clearly, this wavelength selection scheme is similar to the one described previously in the case of UV–Vis spectroscopy. For realistic measurement results, fluorescence spectra should be measured from sufficiently dilute samples with absorbances A below a value of roughly 0.1. [101] This limitation can be attributed to inhomogeneity in excitation intensity and efficient self-absorption of fluorescence inside highly absorbing samples (i.e., inner filter effects). [2]

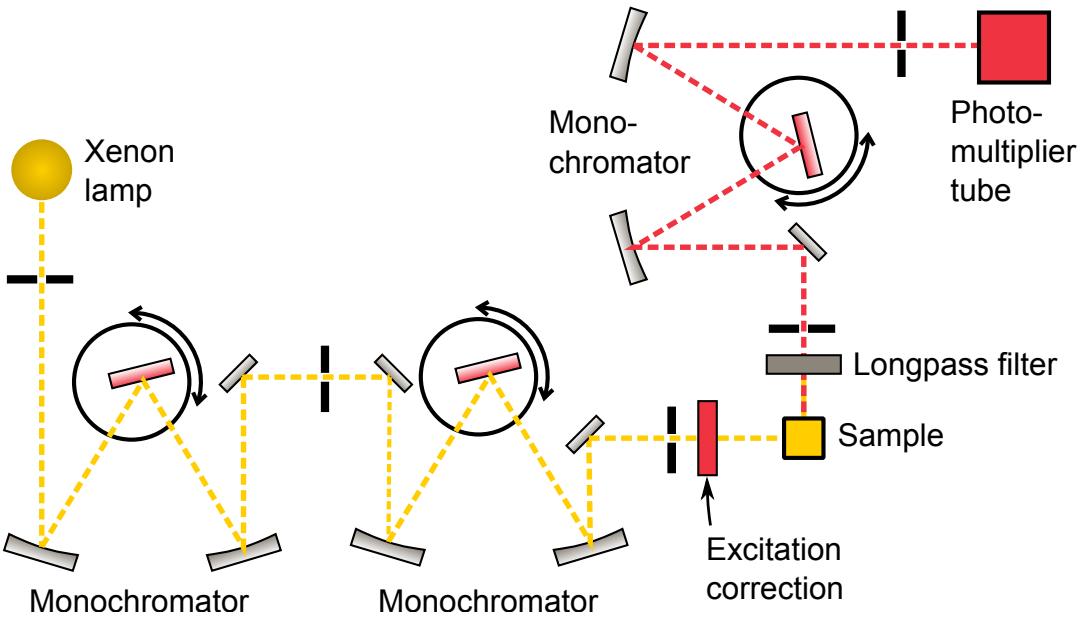

Figure 20: A schematic representation of the optical system in the QuantaMaster 40 fluorometer used for this thesis.

After passing through the two monochromators, the excitation beam is split in two. In order to filter the effect of excitation intensity fluctuations from measured fluorescence spectra, a fraction of the excitation beam is directed to a photodiode. The rest of the excitation beam passes to the studied sample. Finally, the emission spectrum of the sample is recorded using a monochromator connected to a PMT. For liquid samples, rectangular quartz cuvettes are used for measurements. In order to reduce background noise due to stray light, light emitted by liquid samples is usually collected at an angle of 90° with respect to the excitation direction.

For thin films, such as organic molecules deposited onto a glass substrate, samples should be appropriately rotated to inhibit specularly reflected light from reaching

the collection optics. In this thesis, thin film samples were excited at an polar incidence angle of roughly 15°, yielding a collection angle of approximately 75°. For highly scattering samples, longpass filters need to be additionally placed before the collection optics to prevent diffusely reflected light from entering the detector. For this purpose, some of the measurements in this work were done using a longpass filter (Semrock BrightLine FF02-409/LP-25) with a cut-on wavelength of 409 nm.

Confocal fluorescence microscopy

Confocal fluorescence microscopy is an optical far-field imaging technique that can produce high-contrast, diffraction-limited images of fluorescent samples. This section only considers so-called stage-scanning confocal fluorescence microscopes in which studied samples are illuminated by a stationary, focused light beam and translated on a sample stage. Contrary to standard full-field microscopy, such confocal microscopy techniques can be described as serial imaging methods, i.e., an image of a sample is formed one point at a time. To illustrate the operating principle of a stage-scanning confocal fluorescence microscope, Figure 21 shows a schematic of the Witec alpha300 S scanning near-field optical microscope in its confocal fluorescence microscopy operation mode.

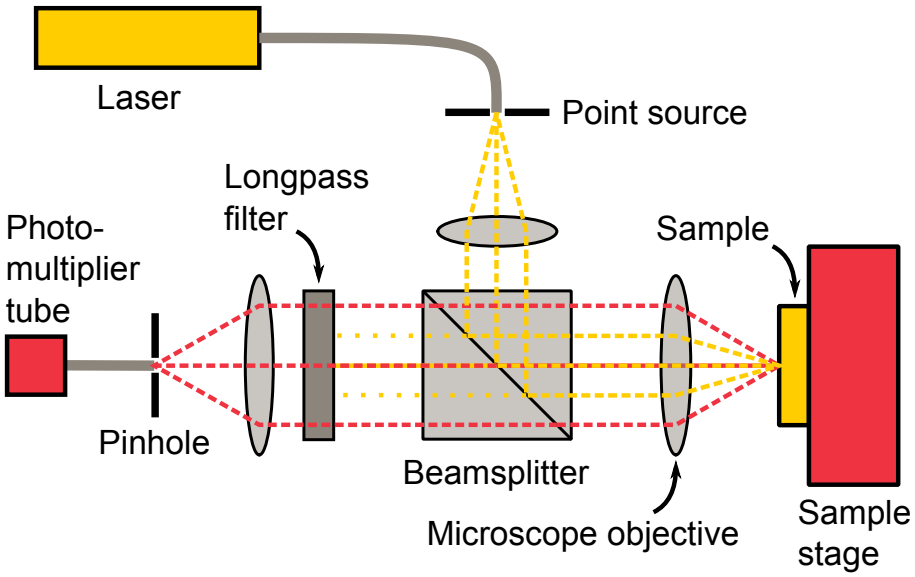

Figure 21: Schematic illustration of confocal fluorescence microscopy using the Witec alpha300 S scanning near-field optical microscope.

In order to attain sufficiently high excitation intensities, confocal fluorescence microscopes usually utilize lasers as light sources. [2] Two different lasers with peak wavelengths of 403 nm and 532 nm were used for this thesis. In the alpha300 S, laser light is coupled to the instrument using a polarization-maintaining single-mode optical fibre. During measurement, the laser light is focused onto a sample through a beamsplitter and a microscope objective, exciting fluorophores in the sample. In the present work, confocal fluorescence images were measured using a Carl Zeiss EC

Epiplan microscope objective with a magnification of 20 and a numerical aperture of 0.4. In order to form a 2D fluorescence intensity image of the measured sample, the alpha 300 utilizes specimen scanning, i.e., the measured sample is moved with respect to the objective on an automated sample stage.

When using the so-called pick-up configuration of the alpha300 S, fluorescence emitted from the illuminated spot on the sample is collected by the microscope objective. Then, the emitted light passes through a beamsplitter and a longpass filter that inhibits the passage of the excitation beam. The confocal fluorescence measurements in this thesis relied on two different longpass filters, Semrock BrightLine FF02-409/LP-25 and Thorlabs FELH0550, at excitation wavelengths of 403 nm and 532 nm, respectively. After passing through a longpass filter, the collected fluorescence is focused to the end of an optical fibre that effectively acts as a pinhole. Finally, the optical fibre delivers the collected fluorescence to a PMT for detection.

In confocal microscopy, image contrast and resolution are enhanced by the focusing of the collected fluorescence to a pinhole prior to optical detection. This enhancement can be explained by the imaging properties of the microscope: only the focal point of the microscope objective is imaged to the pinhole, so that off-focus points on the sample produce only a minor contribution to the measured fluorescence intensity. Using scalar diffraction theory, the lateral resolution r_{min} of a confocal microscope can be approximately written as

$$r_{min} \approx \frac{0.61}{\sqrt{2}} \frac{\lambda_{exc}}{\mathrm{NA}}, \tag{63}$$

where NA is the numerical aperture of the microscope objective. [102] In other words, the resolution of a confocal microscope is improved roughly by a factor of $\sqrt{2}$ compared to a conventional full-field microscope. Using Equation 63, the resolution of the measurement configuration used in this thesis can be approximated as 434 nm or 573 nm, corresponding to excitation wavelengths of 403 nm and 532 nm, respectively.

In addition to affecting the image resolution of a confocal microscope, the choice of objective also influences the collection efficiency of fluorescence from the studied sample. Naturally, collection efficiency is proportional to the acceptance angle of the objective. Using numerical apertures, the collection efficiency Q_{coll} can be expressed as

$$Q_{coll} \propto \frac{1}{2}\left[1 - \sqrt{1 - (\mathrm{NA}/n)^2}\right], \tag{64}$$

where n is the refractive index of the medium surrounding the objective (i.e., air or immersion oil). [102] In accordance with the above equation, a high numerical aperture is beneficial for confocal fluorescence microscopy, enhancing collection efficiency and detection sensitivity.

In this work, confocal fluorescence microscopy is used to measure the fluorescence intensities I_{meas} of fluorophores placed in the vicinity of plasmonic particles. In such

a case, the measured fluorescence intensity can be written as

$$I_{meas} \propto F_{abs}\, F_P\, Q_{coll}\, \sigma, \tag{65}$$

where F_{abs} and F_P are the average absorption enhancement and Purcell factors experienced by the fluorophores, respectively. [77] Q_{coll} is the collection efficiency of the measurement instrument, accounting for variations in fluorescence far-field patterns and the angular acceptance profile of the confocal microscope, while σ is proportional to the density of fluorophores on a given sample. In this thesis, σ is assumed to stay relatively constant between similarly dye-coated samples. However, Q_{coll} cannot be presumed to stay strictly constant, as the proximity of metal NPs can affect the radiation patterns of organic fluorophores. [69] In spite of this, such considerations are omitted in the present work due to time and experimental constraints.

5 Results and discussion

This chapter presents results attained using the experimental and simulation methods described in Chapter 4, and the results are assessed based on the theory discussed in Chapters 2 and 3. Section 5.1 first determines the suitability of different NP array designs for FE using FEM simulations. The results of these simulations are verified by comparisons to FEM simulations based on a different theoretical formalism. In Section 5.2, FE is experimentally demonstrated using an NP array fabricated based on one of the simulated NP array designs. This chapter also compares the measured optical properties of a real Ag NP array to simulation results in order to evaluate the applicability of FEM simulations for designing plasmonic NP arrays.

5.1 Simulated extinction spectra

This section describes the results of the FEM simulations used to determine suitable NP array structures for the enhancement of molecular fluorescence. Optical properties were determined for a total of 15 array designs. The FEM simulations assessed the influence of particle size and interparticle distances (i.e., array periodicity) on the optical properties of the simulated plasmonic NP arrays. In general, the studied arrays exhibit two different types of plasmon modes: single-particle modes and array resonances. The single-particle modes can be recognized as dipolar modes or multipolar modes based on their field distributions. For the simulated structures, dipole resonances peaked at wavelengths above 450 nm, while multipolar extinction peaks were observed at roughly 400 nm. Contrary to single-particle modes, array resonances are most easily identified by comparing the extinction spectra of NP arrays with different periodicities, though identification based on field distributions is also possible.

Figure 22 depicts the extinction efficiencies and FE-FOMs of three different Ag NP arrays with varying particle radii, illuminated by a normally incident plane wave. The radii are measured on a plane parallel to the substrate surface. Due to their truncated shape, the heights of the simulated particles are 15 % shorter than their diameters. In the figure, all the NP arrays have a periodicity of 250 nm. Increased NP size was seen to lead to a higher scattering efficiency and a distinctive red-shift of dipole resonances, caused by dynamic depolarization. These red-shifts were accompanied by a widening of the resonance peaks, supposedly caused by increased radiative damping of plasmon resonances. The particles also featured quadrupole resonances at a wavelength of roughly 410 nm. For quadrupole resonances, spectral shifts were relatively minor. Increased particle size was seen to strengthen quadrupole resonances, so that the quadrupole extinction peak of the particles with 75 nm radii was noticeably higher than their dipole resonance peak.

As depicted in Figure 23, the simulated extinction spectra of the four arrays with 500 nm periodicities show both similarities and differences compared to the more dense arrays of Figure 22. In both figures, the extinction spectra of the arrays with the smallest particles are relatively similar, i.e., individual NPs in these arrays are

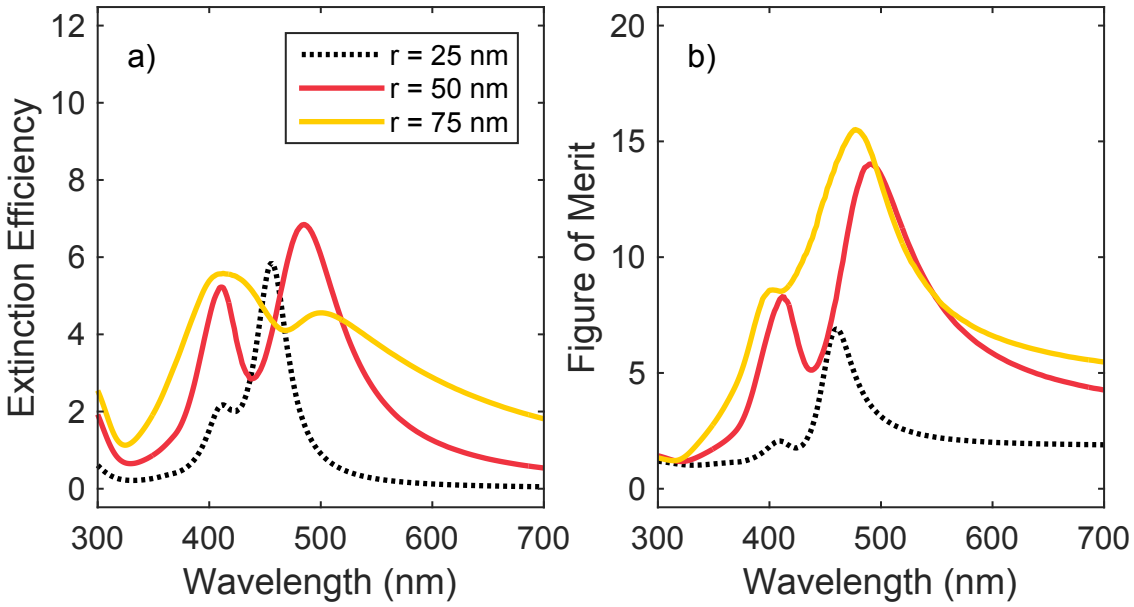

Figure 22: a) Extinction spectra and b) fluorescence enhancement figures of merit for four silver nanoparticle arrays with periodicities of 250 nm and varying particle radii r.

not affected by their neighbouring NPs. This effect is related to the low scattering cross sections of the NPs. In a weakly scattering array, the total field experienced by an individual particle is simply the plane wave incident on the array, despite the array periodicity. Although the spectra of the smallest particles were nearly identical for the two periodicities, distinctive differences were noticed for other NP sizes. In particular, the dipole resonance frequencies of different arrays were more sensitive to changes in particle size for the arrays with 500 nm periodicities.

For the 500 nm arrays, array resonances were observed for the three arrays with the largest particles at approximately 510 nm. This array resonance wavelength could clearly be associated with the Rayleigh cut-off wavelength corresponding to the disappearance of the fundamental air diffraction mode in the arrays. The extinction cross sections of these array resonances were highly dependent on the size of the particle, larger particles with high scattering cross sections producing more pronounced array resonances. The array resonance of the 100 nm NPs could well be used for FE, as the FE-FOM corresponding to the array resonance was relatively high. Furthermore, the extinction peak corresponding to this array resonance was narrow, indicating a high Q-value and, consequently, an increased Purcell effect.

In order to verify the results presented in Figures 22 and 23, the same arrays were additionally modelled using a different theoretical formalism. The results of these full-field verification simulations (see Section 4.3) are depicted in Figures 24 and 25. Using the full-field formulation, all relevant diffraction orders of the arrays need to be explicitly specified using diffraction ports, making simulations with large grating periodicities very memory-intensive. Consequently, only NP arrays with 250 nm and 500 nm periodicities were simulated. To facilitate comparisons with

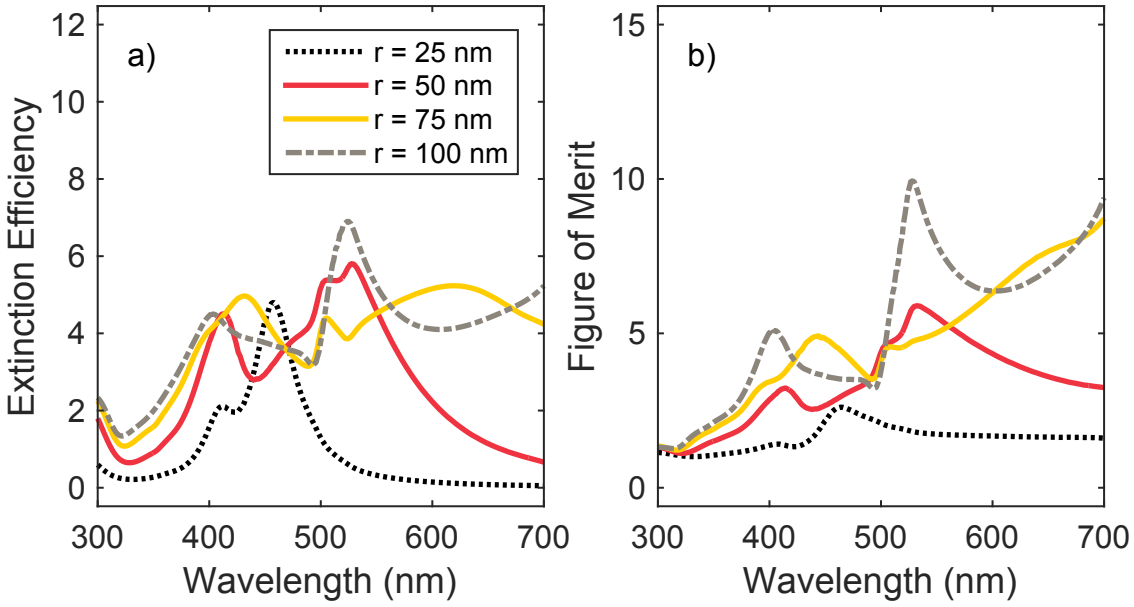

Figure 23: a) Extinction spectra and b) fluorescence enhancement figures of merit for four silver nanoparticle arrays with periodicities of 500 nm and varying particle radii r.

the previous results, the minima in scattering spectra of the arrays with 25 nm particle radii were normalized to zero by a simple constant subtraction from the entire spectrum. This was done to filter out the effect of specular reflection from the substrate–superstrate boundary so that the spectra more closely relate to the properties of the arrays. Clearly, the extinction peak positions of the various arrays closely match the previous simulations. However, the magnitudes of these peaks vary depending on the problem formulation.

The most important difference noticed between the two simulation methods was the saturation of extinction efficiency for dense arrays composed of large NPs. This saturation is evident, for example, in the extinction spectrum of the 250 nm array with 75 nm particle radii; The quadrupole resonance peak value using the scattered field formulation was 5.6, whereas the total field formulation yielded a peak value of only 3.5. In reality, the maximum extinction cross section of the particles is limited by the unit cell area of the array, Λ^2. Converted to intensity transittance, the extinction efficiency of 3.5 corresponds to a transmittance of only 1 %. Although intrinsic to the total field formulation, the scattered field formulation clearly overestimates the extinction efficiencies of dense arrays. However, the FE-FOMs in Figures 24b and 25b agree well with the predictions made using the scattered field formulation. In particular, the average field magnifications were seen to match unusually well with a maximum fractional change of only 5 %. Consequently, most of the numerical variations in FE-FOMs can be attributed to variations in the scattering-to-extinction ratios C_s/C_{ext}.

Continuing with larger array periodicities, Figures 26 and 27 depict the extinction spectra and FE-FOMs of NP arrays with array periods of 750 nm and 1000 nm,

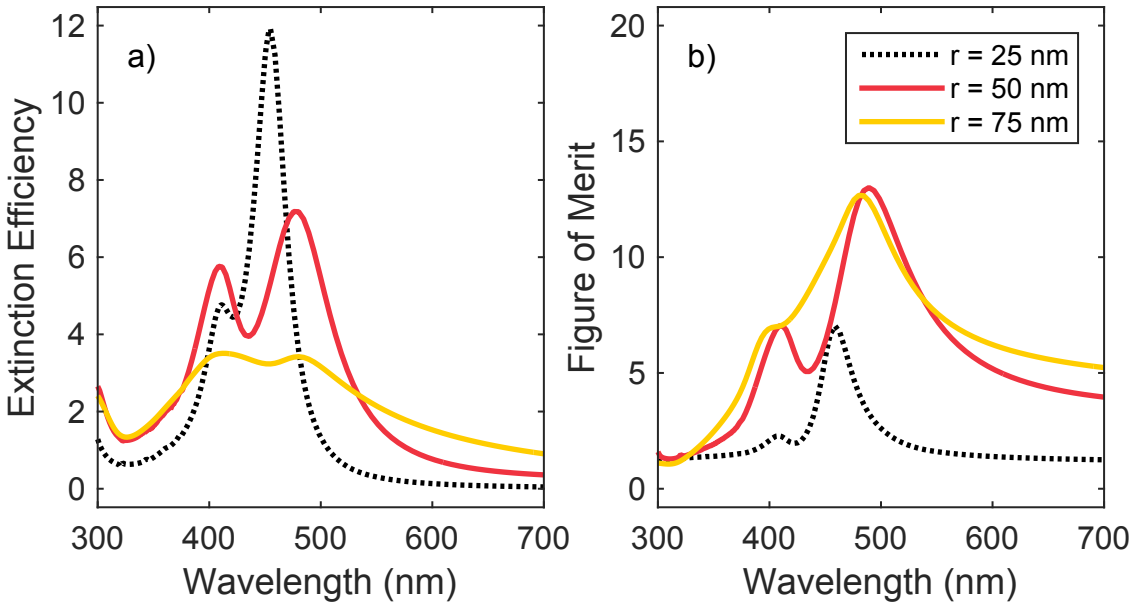

Figure 24: a) Extinction spectra and b) fluorescence enhancement figures of merit for three silver nanoparticle arrays with periodicities of 250 nm and varying particle radii r, calculated using the full-field formulation.

respectively. For these two interparticle separations, increases in array periodicity raised the number of array resonances observable in simulated extinction spectra. Such behaviour is to be expected, as an increased array periodicity red-shifts the fundamental array resonance wavelength of an array. Since array resonances grow stronger with particle size, this effect is most easily observed in the NP arrays with the largest particles. The extinction spectra of these arrays do not exhibit clearly distinguishable peaks, instead forming a nearly continuous extinction band due to multiple overlapping resonances. For FE, such spectral overlap of resonances should be avoided in order to maintain a simple correspondence between theoretical predictions and experimental results. In reality, as particle size and shape variations reduce coupling effects between individual particles, more easily discernible single-particle resonances should be expected for arrays with large interparticle separations.

In order to achieve measurable FE in ensemble measurements, the extinction cross section of the utilized array should be as high as possible. This trend is illustrated in Figure 28 for arrays with 50 nm particles. In particular, if the extinction cross section of an individual NP is not of the same order of magnitude as the area of a single unit cell in the array, light incident onto the array will interact with the particles only to a minor extent. In such a case, most of the light will pass through the array unhindered, and absorption rates of fluorophores placed in the vicinity of the NPs will be largely unaltered. Though not taken into account in the definition of FE-FOM presented in Section 4.3, increased interparticle separations also lengthen average interaction distances between the fluorophores and the particles, reducing the average Purcell factors experienced by the fluorophores. This tendency further favours shorter interparticle separations compared to larger ones.

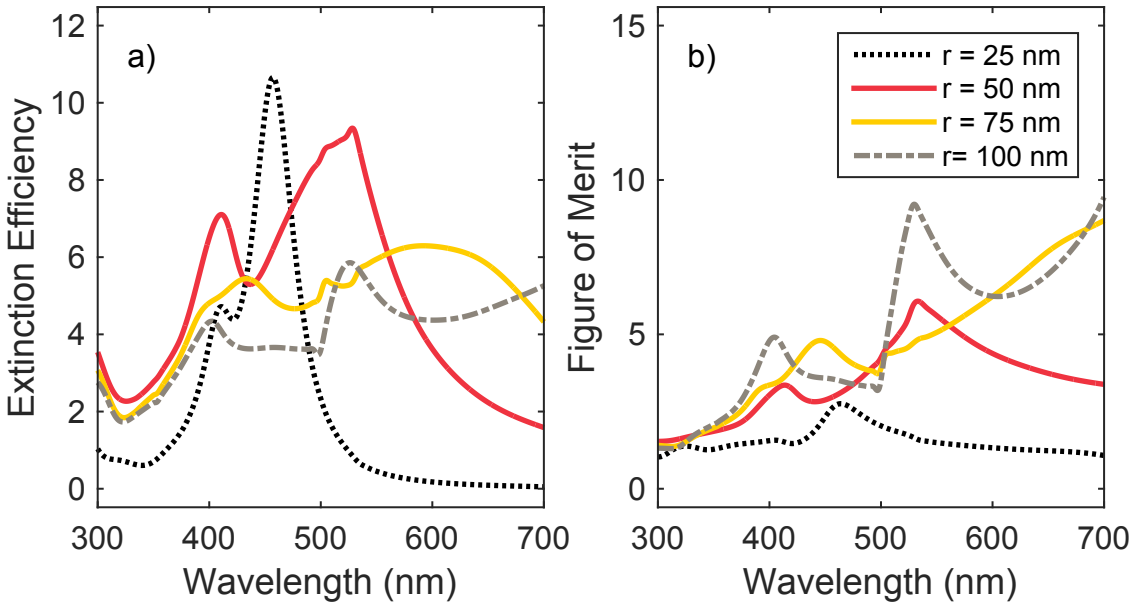

Figure 25: a) Extinction spectra and b) fluorescence enhancement figures of merit for four silver nanoparticle arrays with periodicities of 500 nm and varying particle radii r, calculated using the full-field formulation.

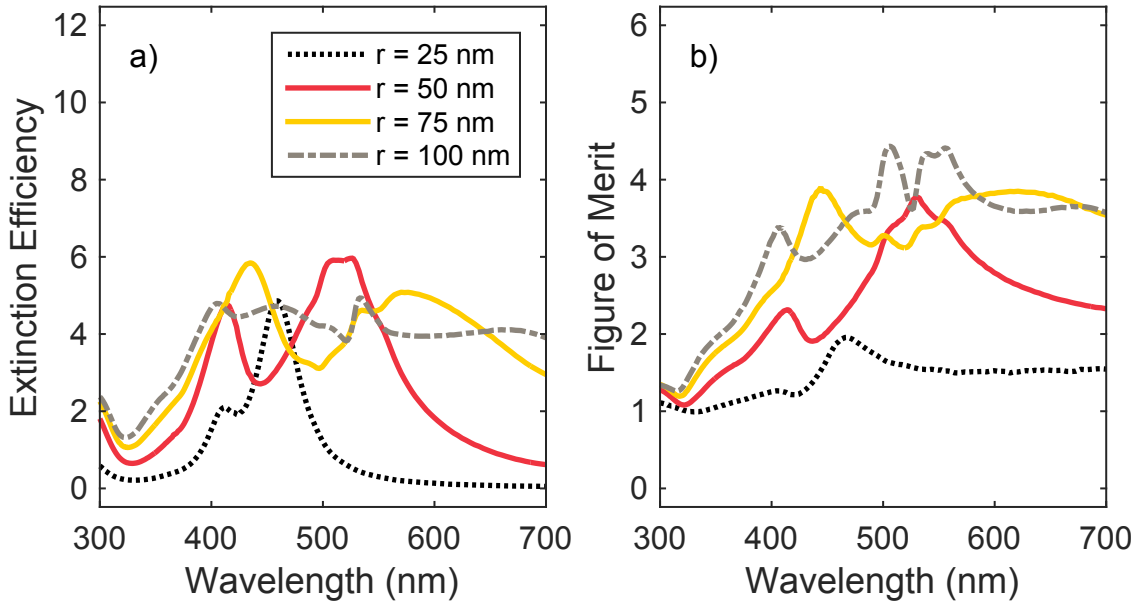

Figure 26: a) Extinction spectra and b) fluorescence enhancement figures of merit for four silver nanoparticle arrays with periodicities of 750 nm and varying particle radii r.

Based on the results above, two different array designs are proposed. In the first array design, individual particles are relatively small with radii of approximately 50 nm, and the dipole resonance of these particles is tuned with the emission wave-

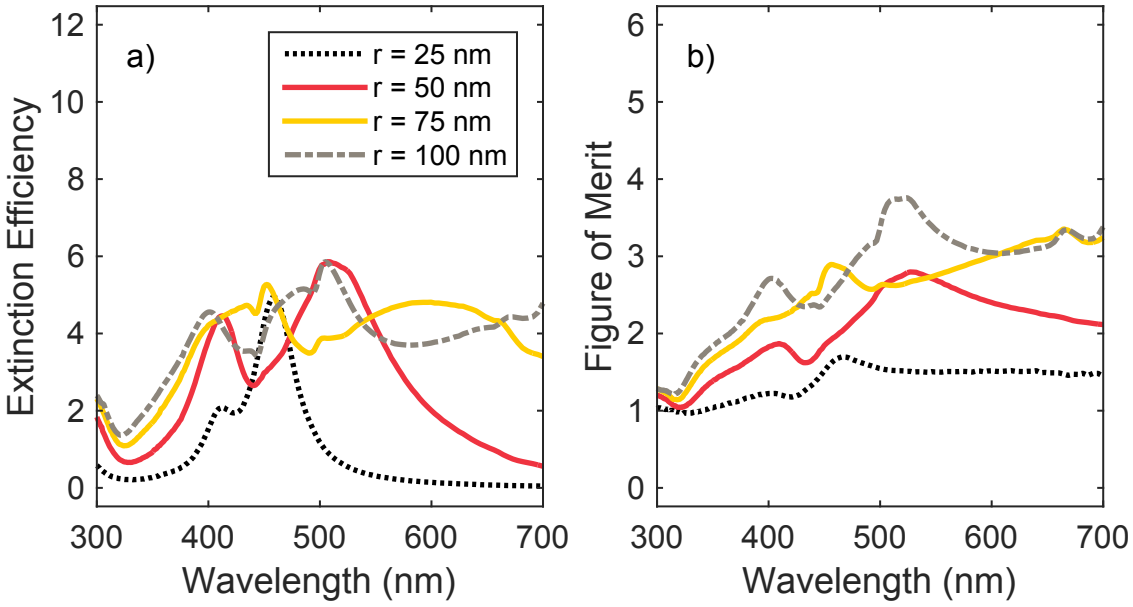

Figure 27: a) Extinction spectra and b) fluorescence enhancement figures of merit for four silver nanoparticle arrays with periodicities of 1000 nm and varying particle radii r.

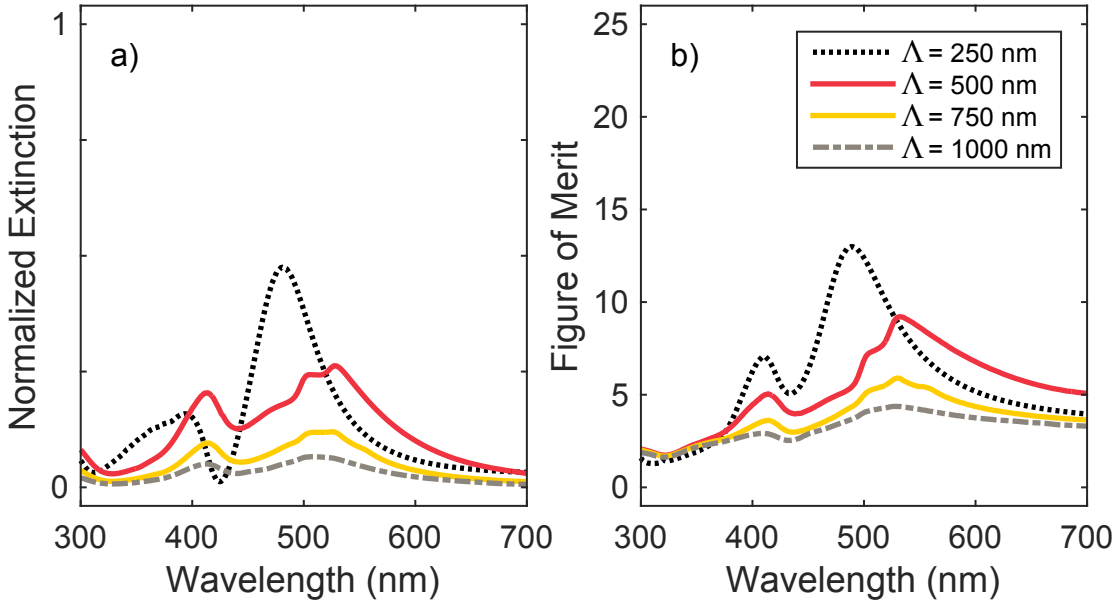

Figure 28: a) Normalized extinction cross sections and b) fluorescence enhancement figures of merit for four silver nanoparticle arrays with radii of 50 nm and different array periodicities Λ. The cross sections in a) were normalized with respect to the unit cell area Λ^2 of each array.

length of a fluorophore. The particles are positioned close to each other to increase their surface density, which should increase the sensitivity of ensemble fluorescence

measurements. An array periodicity of 250 nm was also seen to make the dipole resonance frequency less sensitive to the exact size of the particle, which is expected to facilitate the optimization of fabrication parameters in the APIL process. Built around this design, a Ag NP array with a periodicity of roughly 250 nm was fabricated, and experimental measurement data on this array will be presented in Section 5.2.

The second design utilizes significantly larger NPs with radii larger than 75 nm. These NPs feature strong array resonances, the resonance wavelengths of which can be adjusted simply by changing the array periodicity. The most pronounced resonance corresponds to the disappearance of the fundamental air diffraction mode in the arrays, i.e., the resonance wavelength is slightly longer than the array period, Λ. Usage of large NPs ensures strong coupling between individual particles. However, this array design was excluded from this thesis, as the usage of a non-standard fabrication method was assumed to result in increased variations in particle sizes and shapes. The array resonances in Ag NP arrays based on the APIL process could, however, be studied separately in the future.

5.2 Fluorescence enhancement with dipolar resonances

This section describes measurement results of FE using a Ag NP array with short interparticle distances. In order to achieve FE, the dipole resonance wavelength of the fabricated particles is tuned with the fluorescence emission spectrum of R6G molecules. The section focuses on the optical characterization of the fabricated array and the FE results measured using confocal fluorescence microscopy, and a more thorough investigation of the correspondence between experimental and simulation results is postponed until Section 5.3.

Figure 29 depicts a Ag NP array prior to the deposition of a protective dielectric coating by ALD (see Section 4.1). As annealing steps were neglected in the case of this particular sample, considerable particle shape variations can be seen throughout the array. Using the free image analysis software ImageJ [103], the widths and lattice constants of the particles were measured, yielding values of 132 nm and 92 nm for the widths, as well as 230 nm and 242 nm for the lattice constants in the horizontal and vertical directions, respectively. The angle between these two lattice directions was measured to be 88.7°, reasonably close to the value 90° for a square lattice.

After the deposition of a thin dielectric alumina coating using ALD, the extinction and scattering spectra of the array were measured to determine the suitability of the NP array for enhancing the molecular fluorescence of R6G molecules. As the fluorescence intensity of these molecules peaks at roughly 550 nm, the dipole resonance of the particles has to occur at roughly 520 nm, slightly to the short-wavelength side of the fluorophore emission peak. Figure 30 shows the normalized extinction and scattering spectra of the fabricated particles, as well as the fluorescence spectrum of R6G molecules dip coated onto a glass slide. Indeed, the plasmon resonance of the particle array is slightly blue-shifted with respect to the fluorescence emission peak of R6G, justifying further measurements of possible FE by the NP array.

In order to determine the FE efficiency of the the Ag NP array, the fluorescence

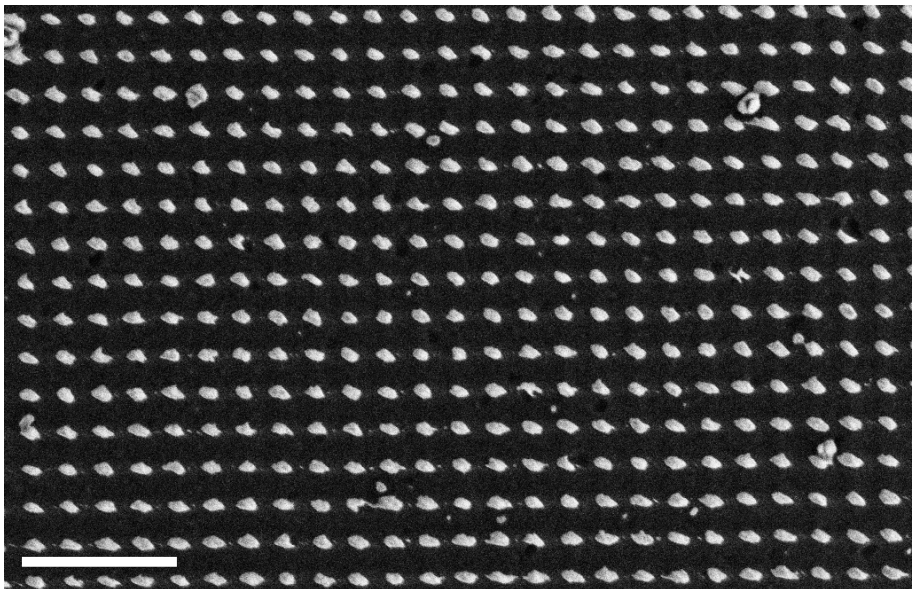

Figure 29: Scanning electron microscope image of a silver nanoparticle array with a periodicity $\Lambda \approx 250$ nm. The length of the scale bar is 1 μm. Figure courtesy of C. Kauppinen.

intensities of R6G molecules dip coated onto the sample were measured on different locations on the substrate surface, as depicted in the three confocal fluorescence intensity maps of Figure 31. Figures 31a and 31b first show the results of two reference measurements taken from a non-coated and a coated portion of the sample, both without NPs at the measurement sites. For comparison, Figure 31c illustrates the fluorescence intensity of R6G molecules deposited onto the NP array. The difference in signal strength is obvious. Specifically, the average PMT count rates of the the two reference measurements were calculated as 0.55 kHz and 1.43 kHz, whereas the average count rate of in Figure 31c was 5.88 kHz. Compared to the intensity obtained without the NPs, the average fluorecence intensity enhancement factor can be calculated to be roughly 4.11.

The FE factor of the studied Ag NP array is rather modest in relation to comparable FE values reported in the literature. For example, average FEs of the order of 50-fold have been reported using Au nanospheres. [70] Nevertheless, the measured FE value of 4.11 deserves additional merit due to the well controlled deposition method used for immobilizing R6G molecules onto the measured sample. Furthermore, all values reported in this thesis result from the averaging of an enormous number of data points, virtually eliminating the possibility of statistical errors. Since an image is formed of all measured samples, one can also practically reject the possibility of reaching false FE factors due to the aggregation of the fluorophores.

Due to the high intrinsic fluorescence quantum yield of R6G molecules, increases in the fluorescence quantum yield of the molecules are not probable. Instead, a major part of the measured FE can probably be contributed to absorption enhancement. However, as the plasmon resonance of the particles is assumed to exhibit consid-

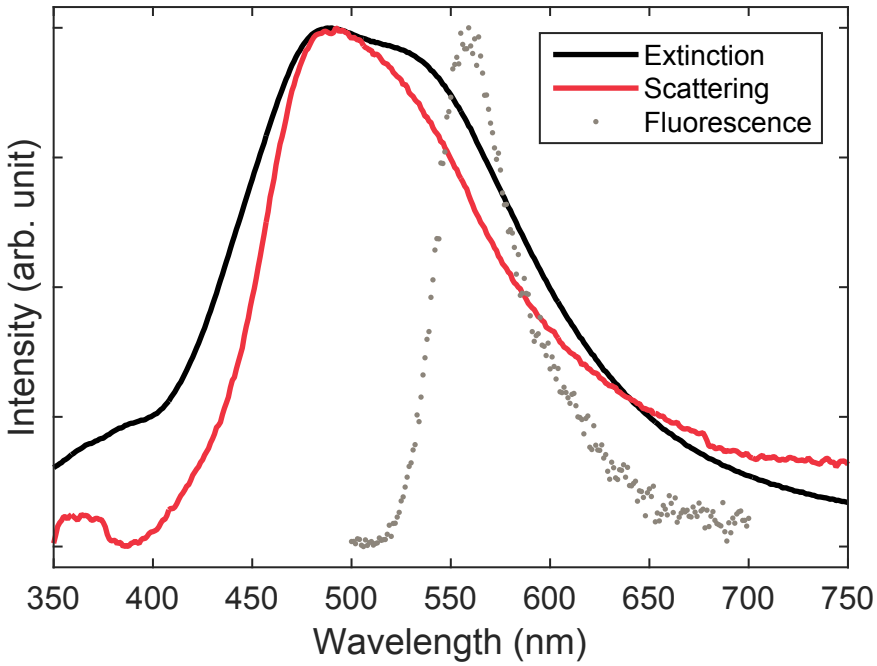

Figure 30: The normalized extinction and scattering spectra of the studied silver nanoparticle array, as well as the fluorescence emission spectrum of rhodamine 6G molecules immobilized on a glass substrate.

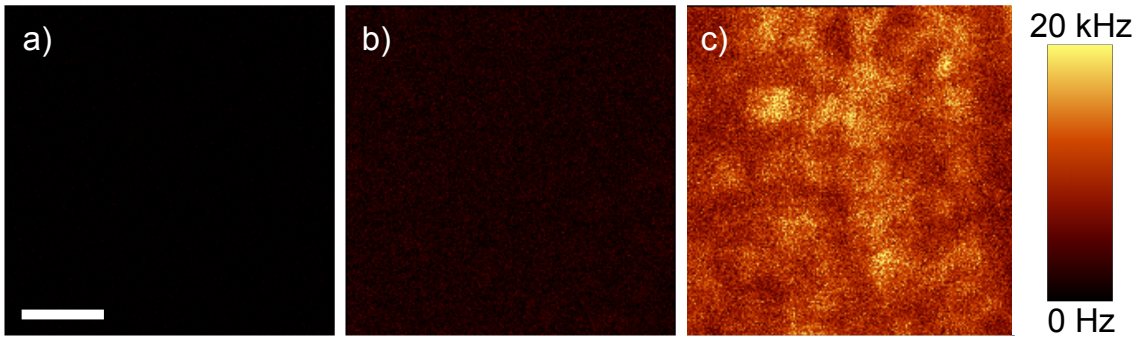

Figure 31: Spatial fluorescence intensity maps of a) the ALD-coated substrate without nanoparticles or fluorophores, b) rhodamine 6G molecules on the substrate without nanoparticles, and c) rhodamine 6G molecules on the nanoparticle array. The length of the scale bar is 5 μm, and the colour scale indicates the measured photomultiplier tube count rate.

erable horizontal dipolar character, the measurable fluorescence intensity may also be increased due to changes in the angular emission pattern of the fluorophores. Such effects may, however, be reduced by the high intrinsic fluorescence quantum yield of R6G. As all optical filters exhibit finite leakage at their stop-bands, a minor intensity increase should also be assigned to elastic scattering by the particles. Nevertheless, as the signal intensity measured on top of a clean portion of the substrate (see Figure 31a) is relatively low, measurement errors caused by the particles should

be minor.

5.3 Quadrupole resonances in large nanoparticles

Having successfully demonstrated that FE can be achieved using the studied Ag NP arrays, this chapter continues by comparing experimental measurements with simulation results. Due to insufficient characterization routines and the perceived particle irregularity in the case of the array described previously, the results in this section are based on a different NP array. This second array is depicted in Figure 32 prior to a subsequent annealing step.

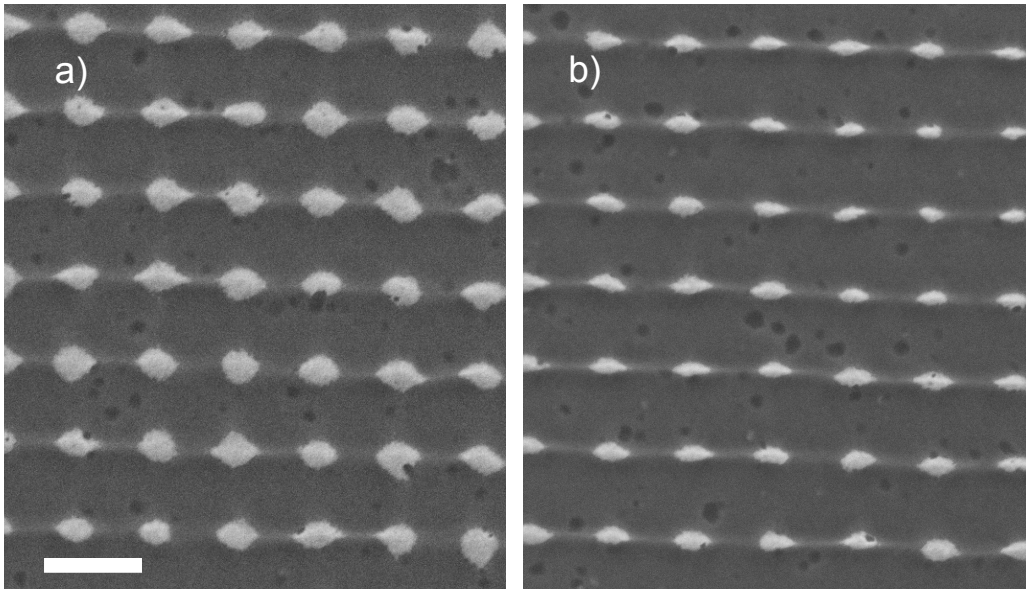

Figure 32: Two scanning electron microscope images of a two-dimensional silver nanoparticle array with a periodicity $\Lambda \approx 1$ μm before annealing. Images in a) and b) were taken from different locations on the sample. The length of the scale bar is 1 μm.

Although depicting the same NP array sample, the two scanning electron micrographs of Figure 32 feature both similarities and noticeable differences. As a result of extended Ar milling, both micrographs feature particles that are distinctively irregular. This irregularity in particle shapes is presumably further increased by voids in the glass substrate. On the other hand, the most noticeable difference observed between Figures 32a and 32b is related to the sizes of individual NPs. In Figure 32a, the particles have an average cross-sectional area of roughly 0.089 μm^2, whereas the ones in Figure 32b are a factor of two smaller with an average cross-sectional area of only 0.044 μm^2. Based on this data, the fabricated NPs can be argued to exhibit severe size variations. These variations may be caused by a variety of factors, including uneven spin coating of azopolymer onto the sample and spatial variations in reactive ion etching rates. Such size variations are presumed to complicate the finite-element modelling of plasmonic NP arrays fabricated by the APIL-based method.

In the future, these variations might be reduced by using larger, possibly circular, substrates.

After an annealing step in 600°C for 20 min, the shapes of the NPs change considerably. This can be clearly seen in Figure 33a, depicting an AFM image of the same NP array after annealing and the deposition of a dielectric coating with a thickness of roughly 10 nm by ALD. In order to illustrate the three-dimensional shape of the resulting particles, a representative cross-sectional view of the array is also depicted in Figure 33b. In the figure, individual particles can be seen to be roughly semi-ellipsoidal in shape. Based on this shape, the Ag NPs are assumed to melt, coalesce, and solidify during annealing, resulting in increased particle shape uniformity and symmetry. Based on the AFM data, individual particles were estimated to have average diameters of 446 nm and 382 nm in the horizontal and vertical directions, respectively. Additionally, the height of the particles was measured as approximately 100 nm. However, the exact volumes of individual particles are assumed to exhibit sizeable variations. Such variations were later verified by SEM, and the results of the AFM measurements were estimated to better represent maximum NP dimensions, rather than ensemble averages.

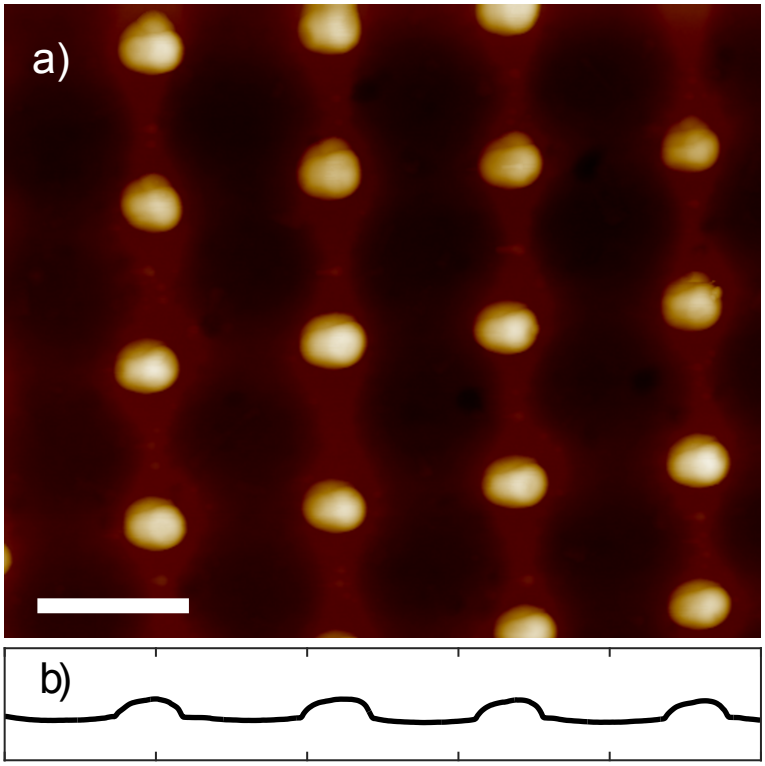

Figure 33: a) An atomic force micrograph of a silver nanoparticle array with large particles after annealing and the deposition of a dielectric coating, and b) a cross section of the array with symmetric axes, showing the shape of the particles. The length of the scale bar is 1 μm.

In addition to the sizes and shapes of individual particles, the measurement data in Figures 32 and 33a can also provide information on the 2D array structure.

Based on Figure 32a, the array periodicities in the horizontal and vertical directions were measured to be roughly 826 nm and 856 nm, respectively. The angle between the two lattice directions was measured as 89°. If measured from Figures 32b, the corresponding values are 831 nm and 846 nm for the periodicities, as well as 87° for the lattice angle, reasonably close to the previous measurement results. Based on this AFM data, however, array periodicities of 1213 nm and 1035 nm were measured in the horizontal and vertical directions, respectively, and the angle between these two directions was measured to be roughly 85°. These values are in clear disagreement with the data gathered from the SEM images of Figure 32.

The measured discrepancies in array periodicities and angles between lattice directions attest to a deficiency in the interference lithography step. In particular, the lithography step utilizes a combination of a pinhole and free-space propagation for producing two planar wavefronts that subsequently interfere to form a sinusoidal intensity pattern on the surface of an azopolymer film. In the case of the present array, the free-space propagation length was approximately 30 cm. In order to obtain nearly planar wavefronts, the length of the free space propagation should be long enough to ensure sufficiently low wavefront curvature on the polymer surface. In the future, such wavefront curvature could be reduced by using a longer free-space propagation length. However, this would also decrease the maximum attainable exposure intensity, lengthening exposure times.

In order to improve the applicability of APIL for the fabrication of plasmonic NPs, the fabrication procedure (see Section 4.1) could be improved also by other means. An ideal process would provide an easily predictable, one-to-one correspondence between the etched azopolymer grating pattern and the final plasmonic structures, eliminating the need for excessive annealing steps and enabling the fabrication of various ellipsoidal NPs. Consequently, the same two general requirements should be set for azopolymer masks as for conventional photoresists: vertical mask sidewalls and high etch selectivity. [104] Since the sidewalls of a sinusoidal surface relief grating are never vertical, the azopolymer mask should be post-processed in order to improve the predictability of the fabrication process. This post-processing should be achievable, for example, by melting the azopolymer to form droplets prior to Ar milling or by utilizing a novel post-processing method called self-perfection by liquefaction [105].

The second requirement, etch selectivity, might be improved by growing a thin layer of aluminum oxide on top of the Au hard mask. After etching the resist in oxygen plasma, the alumina layer could possibly be selectively etched in a buffered hydrofluoric acid bath without affecting either the azopolymer or the underlying Au layer. Such an alumina layer should show better resistivity to Ar milling compared to Au [106], increasing the overall selectivity of the milling process. As an alternative, the Ar milling step could be completely circumvented by developing a suitable lift-off deposition process based on APIL.

Following the dimensional characterization of the final array geometry, the optical properties of the fabricated array were measured by UV-Vis spectrometry. The results of these optical measurements are depicted in Figure 34. In the figure, the extinction spectrum was measured by a simple transmittance measurement, and the

scattering spectrum corresponds to the diffuse reflectance spectrum of the array. The extinction spectrum of the array has a maximum roughly at a wavelength of 420 nm, and the corresponding peak has a distinctive shoulder on its long-wavelength side. As the scattering cross section of the array is relatively low at wavelengths close to 420 nm, this extinction peak was presumed to correspond to a multipolar resonance or a dipole resonance with its dipole moment oriented along the substrate normal. A second, broad peak can also be seen at a wavelength of approximately 700 nm. Based on the scattering data, this second peak was assumed correspond to the horizontal dipole plasmon resonance of the NPs.

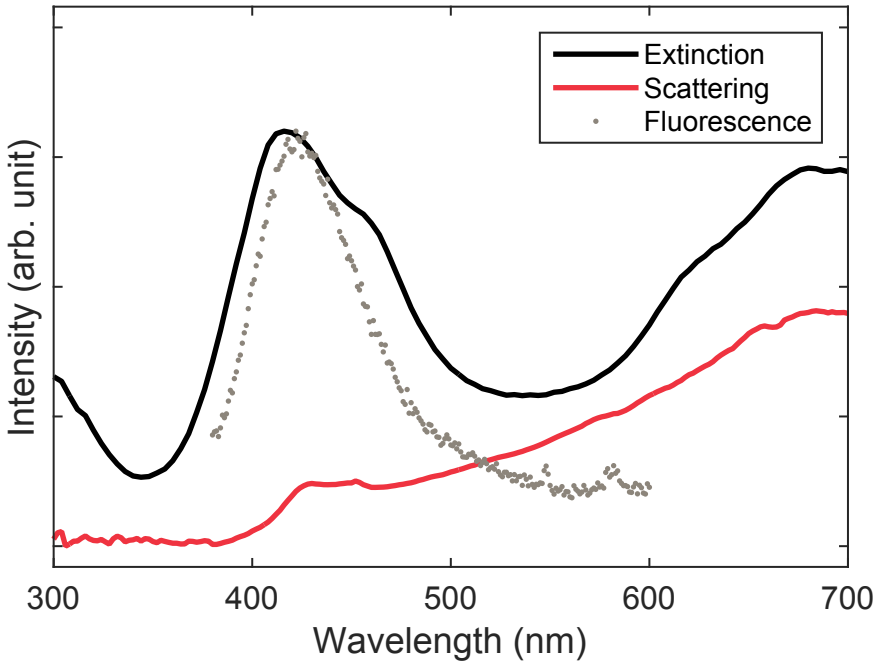

Figure 34: The extinction and scattering spectra of the second silver nanoparticle array, as well as the fluorescence emission spectrum of cascade blue molecules immobilized on a glass substrate. In the figure, different lines are not to scale.

Figure 34 also shows the fluorescence spectrum of CB molecules deposited onto a glass substrate. As the fluorescence spectrum of these molecules peaks close to the observed plasmon resonance of the studied NP array, further measurements on possible FE were conducted using confocal fluorescence microscopy and conventional fluorescence spectroscopy. Figure 35 depicts three fluorescence intensity maps that illustrate the effect of the NPs on the fluorescence intensity of CB molecules. Figures 35a shows the signal intensity measured on the fabricated Ag NP array prior to the deposition of fluorophores, and Figures 35b illustrates the measured signal after the deposition of the fluorophores but without any NPs underneath the fluorophores. The average PMT count rates of these two images were calculated as 2.96 kHz and 7.73 kHz, respectively. Finally, Figure 35c depicts the fluorescence intensity measured on the Ag NP array dip-coated with CB molecules. The average count rate was 12.9 kHz, yielding an average fluorescence intensity magnification of

only 1.67.

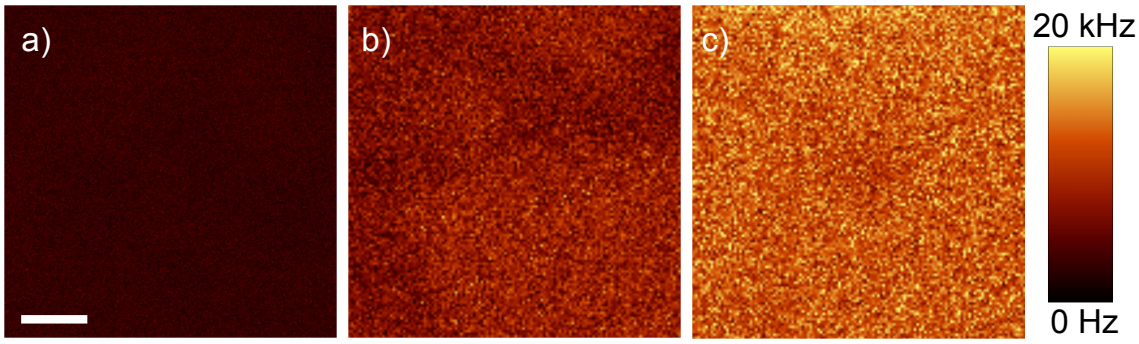

Figure 35: Spatial fluorescence intensity maps of a) coated silver nanoparticles without added fluorophores, b) cascade blue molecules without nanoparticles underneath, and c) the same molecules deposited onto the silver nanoparticles. The length of the scale bar is 2 μm, and the colour scale indicates the measured photomultiplier tube count rate.

Additionally, the fluorescence spectrum of CB dip coated onto the studied NP array was measured using a fluorometer. This additional measurement was done for two reasons: to verify that the increased signal intensity in the confocal fluorescence measurements can be attributed mainly to FE and to investigate whether the emission spectrum of the fluorophores would be altered by the presence of the NPs. Figure 36 depicts the fluorescence spectra of CB molecules dip coated onto both the Ag NP array and a cleaned glass substrate. To record the fluorescence spectrum on the NPs, a longpass filter with a cut-on wavelength of 409 nm was placed in the collection port of the fluorometer. Due to the presence of the additional filter, the fluorescence intensity measured on the NP array sample is normalized to zero at the long-wavelength end of the spectrum. Such normalization assures that measured intensity differences are not caused by variations in stray light intensities.

In Figure 36, a slight fluorescence peak shift from roughly 425 nm to 437 nm was observed due to the presence of the NPs. However, a more distinguishable difference can be seen between the fluorescence intensities of the two samples. Based on the fluorescence spectra in the figure, an approximate FE factor of 7 was calculated simply by comparing peak intensities. This estimate is in clear disagreement with the enhancement factor of 1.67 calculated based on Figure 35 previously. Although this difference could be partially explained by spatial variations in the NP array, the most probable cause for this apparent contradiction lies in the far-field radiation pattern of the fluorophores; The confocal microscope setup used in the experiments only detects fluorescence that is emitted to azimuthal angles below roughly 24° with respect to the substrate surface normal. On the other hand, the fluorometer measurements used a relatively large collection angle of approximately 75°. A higher measured intensity magnification would, therefore, be justified if the NPs redirected the fluorescence of the CB molecules preferentially along the substrate-superstrate boundary. However, additional measurements would be required in order to achieve more conclusive evidence of such directivity.

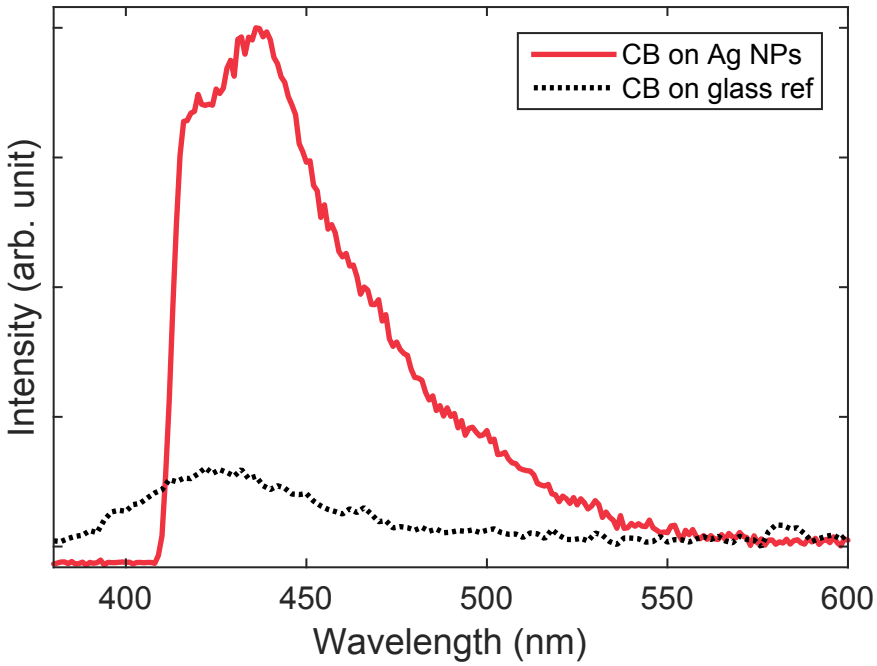

Figure 36: Fluorescence spectrum of cascade blue molecules deposited on a silver nanoparticle array. The reference spectrum was measured from a glass substrate coated with the same fluorophores.

Finally, the Ag NP array studied in this section was simulated using a FEM model similar to those described in Sections 4.3 and 5.1. The results of the simulations are depicted in Figure 37. Based on the SEM images in Figure 32, the array periodicity in the simulation model was set to 850 nm in both lattice directions. Individual NPs were simulated as coated hemispheres with a coating thickness of 10 nm and an inner radius of 87 nm. Such a radius was selected based on additional SEM images taken after the deposition of a 5 nm layer of Au on top of the particles. The height of such particles is also close to the real NP heights measured by AFM.

Figure 37a depicts the simulated extinction, absorption, and scattering spectra of the Ag NPs. In these spectra, two distinct resonances can be seen at wavelengths of roughly 414 nm and 454 nm. Of these two resonances, the one at 414 nm is seen to scatter light more efficiently to the far field. Additionally, a strong resonance can be seen peaking approximately at a wavelength of 690 nm. Based on the high scattering efficiency of the particles on this particular resonance band, the plasmon mode can be argued to possess a strong dipole moment along the substrate surface. Although the simulated spectra, especially the peak positions, are seen to correspond reasonably well with the measured spectra in Figure 34, clear differences were observed in the relative peak heights of different plasmon bands.

In order to evaluate the suitability of the simulated array for FE, Figure 37b illustrates the spectral dependency of the calculated FE-FOM of the NP array, along with the two components contributing to it. Compared to the highest values achieved previously in Section 5.1, the FE-FOM is seen to stay quite low throughout

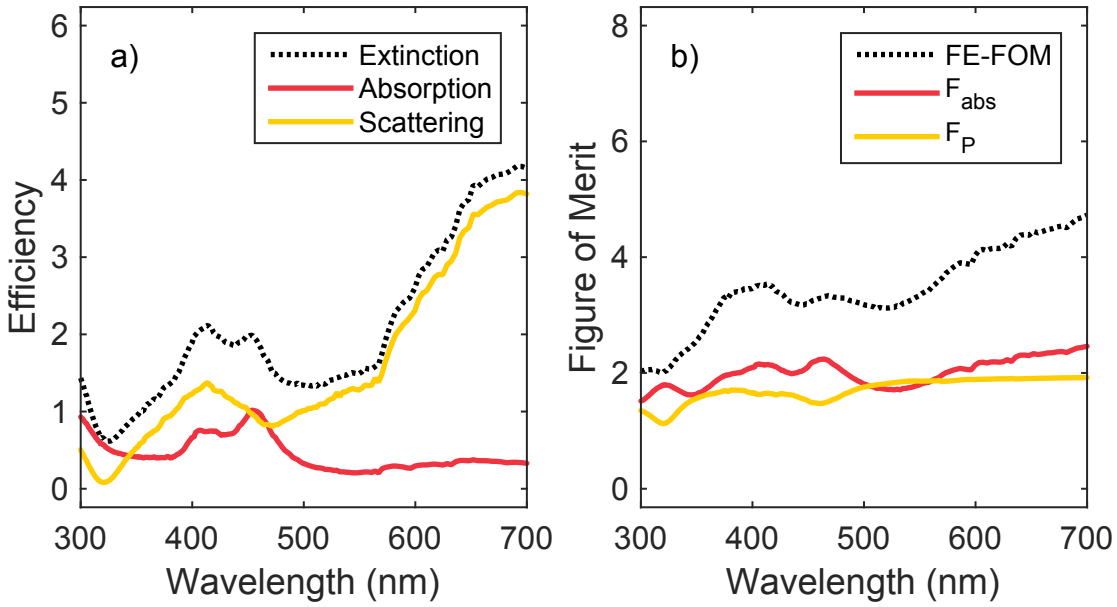

Figure 37: a) Simulated extinction, absorption, and scattering spectra, as well as b) the fluorescence enhancement figure of merit (FE-FOM) of the fabricated nanoparticle array. Approximated numerical values for the two factors, F_{abs} and F_P, contributing to FE-FOM are also depicted in b). In the simulation, the array periodicity and particle radii were set to 850 nm and 87 nm, respectively.

the visible spectrum, increasing slowly with incident wavelength. In particular, the FE-FOM of the simulated array is only approximately 3.5 at the fluorescence emission wavelengths of CB molecules. Thus, the results of the simulations agree with the relatively modest FEs recorded in optical measurements. However, quantitative correspondence is not achieved, as expected due to the approximate nature of the simulations. No more than qualitative correspondence should be expected also due to variations in real NP sizes, shapes, and positions, as well as differences between simulated and real material properties.

The FEM simulations were also used to study the electric near field distributions around individual NPs. Figure 38 depicts these field distributions at each of the three resonance wavelengths of the particles. Based on the figure, the two resonances occurring at the blue end of the visible spectrum, i.e., at wavelengths of 414 nm and 454 nm, correspond to plasmon resonances mostly quadrupolar in character. As predicted previously, the near field of the third resonance occurring at roughly at a wavelength of 690 nm has a distinctive dipolar shape. Although the three images in Figure 38 are assumed to represent the near field distributions in the vicinity of the fabricated NPs fairly well, minor errors are expected to result mainly from the sharp edges in the simulated naNPs along the substrate-superstrate boundary. To avert such sharp features, the simulation geometry could be altered by partially embedding the NP inside the substrate and by rounding the bottom edges of the NPs. These changes were, however, not implemented in the simulations used in this thesis, as such alterations would add the amount arbitrary parameters in the

simulation geometry.

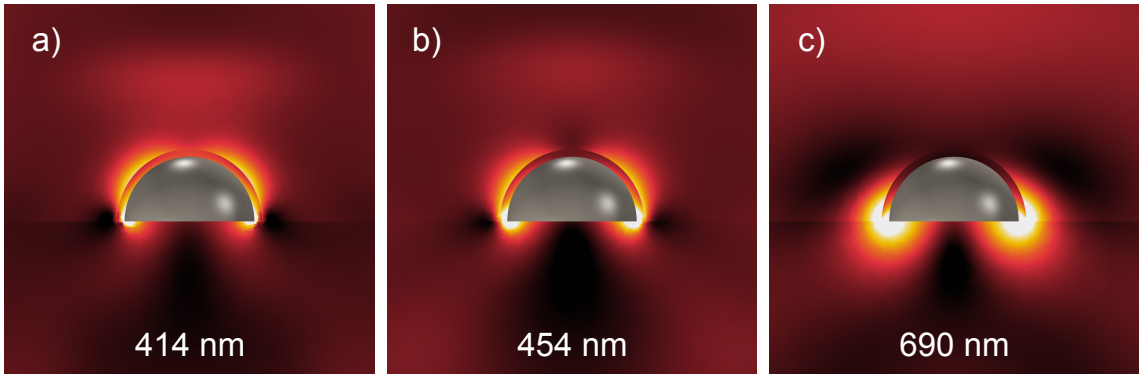

Figure 38: The simulated near field patterns in a two-dimensional nanoparticle array with hemispherical nanoparticles at wavelengths of a) 414 nm, b) 454 nm, and c) 690 nm.

In summary, FE was demonstrated with 2D Ag NP arrays fabricated using the APIL-method with a maximum average enhancement factor of 4.11. Additionally, FEM simulations can, indeed, be used to predict the optical properties of these plasmonic NP arrays and to rapidly estimate their FE efficiency using the concept of FE-FOM introduced in Section 4.3. More specifically, the plasmon resonance wavelengths of such arrays can be reproduced by simulations, though the simulated relative heights of different plasmon bands were observed to vary from those measured from a fabricated NP array. Based on the FEM simulations, short interparticle separations were seen to be beneficial for achieving high average FEs, an effect mainly contributed to increased average intensity magnifications in dense NP arrays.

6 Conclusions

In conclusion, FEM simulations were used to determine 2D Ag NP array designs suitable for enhancing molecular fluorescence. Furthermore, this work investigated the applicability of azopolymer interference lithography for realizing such arrays. The optical properties of fabricated arrays were characterized using UV–Vis spectroscopy, fluorescence spectroscopy, and stage-scanning confocal fluorescence microscopy. Finally, the results of this thesis attest to a qualitative agreement between the simulated and experimentally determined optical properties of 2D Ag NP arrays. Such agreement between simulation and experiment demonstrates the usefulness of FEM modelling for engineering the properties of intricate plasmonic nanostructures.

A series of FEM simulations resulted in two different recommendations for fluorescence-enhancing array designs. The first array design utilizes Ag NPs with radii of roughly 50 nm, positioned in a relatively dense rectangular lattice with a periodicity of approximately 250 nm. According to the simulations, such NP arrays exhibit strong dipolar single-particle resonances with peak wavelengths close to 500 nm. In general, enhanced fluorescence intensities are expected for fluorophores with emission wavelengths slightly red-shifted with respect to these resonance wavelengths. Due to short interparticle separations, dense arrays exhibit high extinction cross sections and resonance wavelengths that are relatively stable with respect to the exact sizes of individual NPs.

Based on diffractive coupling between individual NPs, the second array design relies on slightly larger NPs with radii above 75 nm. When placed in a rectangular lattice, such particles produce a narrow array resonance, and the wavelength of this array resonance can be tuned by altering the periodicity of the NP array. However, in order to exhibit strong array resonances, the NP array has to be embedded in a nearly homogeneous refractive index environment. Moreover, a certain degree of uniformity has to be met regarding interparticle separations, as well as the sizes and shapes of individual particles. Owing to these two requirements, array resonances were not experimentally observed in this thesis.

In this thesis, a maximum FE factor of 4.11 was measured from a sample roughly conforming to the first array design. Compared to values reported in the literature, this enhancement factor is relatively low. This may be partially caused by the high intrinsic fluorescence quantum yield of the R6G molecules used in the experiment. Nevertheless, the FE factors reported in this thesis resulted from the averaging of immense sets of data points, adding a certain degree of statistical certainty to the achieved results. Furthermore, improved results should be attainable with fluorophores exhibiting fluorescence quantum yields lower than that of R6G.

Based on the optical and dimensional characterization of fabricated samples, azopolymer interference lithography can be feasibly utilized for realizing fluorescence-enhancing Ag NP arrays with periodicities ranging between 250 nm and 1000 nm. However, in its present form, the fabrication procedure imposes undesirable constraints on the shapes and sizes of fabricated particles. Moreover, unwanted variation was noticed in critical array parameters, such as particle sizes, interparticle distances, and lattice angles. In essence, such variation causes unavoidable discrep-

ancy between simulations and experimental results.

In this work, several approaches are presented for improving the fabrication scheme used for this thesis: the NP arrays could be fabricated onto larger substrates, and the interference lithography could utilize a longer free-space propagation length to reduce the curvature of interfering wavefronts. Furthermore, fabricated azopolymer masks could be post-processed, for example, by thermal treatments prior to the formation of plasmonic nanostructures by Ar milling. In the future, improved nanofabrication schemes based on azopolymer interference lithography could be implemented for studying various optical phenomena, including FE and surface-enhanced Raman scattering, as well as array resonances in diffractively coupled NP arrays.

References

[1] J. R. Lakowicz, *Principles of Fluorescence Spectroscopy*, 3rd ed. New York: Springer, 2006.

[2] B. Valeur and M. N. Berberan-Santos, *Molecular Fluorescence: principles and applications*, 2nd ed. Weinheim, Germany: Wiley-VCH, 2013. [Online]. Available: http://dx.doi.org/10.1002/9783527650002

[3] M. Orrit and J. Bernard, "Single pentacene molecules detected by fluorescence excitation in a *p*-terphenyl crystal," *Phys. Rev. Lett.*, vol. 65, no. 21, pp. 2716–2719, Nov. 1990. [Online]. Available: http://dx.doi.org/10.1103/PhysRevLett.65.2716

[4] K.-S. Lee and M. A. El-Sayed, "Gold and silver nanoparticles in sensing and imaging: sensitivity of plasmon response to size, shape, and metal composition," *J. Phys. Chem. B*, vol. 110, no. 39, pp. 19 220–19 225, Oct. 2006. [Online]. Available: http://dx.doi.org/10.1021/jp062536y

[5] B. Auguié and W. L. Barnes, "Diffractive coupling in gold nanoparticle arrays and the effect of disorder," *Opt. Lett.*, vol. 34, no. 4, pp. 401–403, Feb. 2009. [Online]. Available: http://dx.doi.org/10.1364/OL.34.000401

[6] H. Chen, X. Kou, Z. Yang, W. Ni, and J. Wang, "Shape- and size-dependent refractive index sensitivity of gold nanoparticles," *Langmuir*, vol. 24, no. 10, pp. 5233–5237, May 2008. [Online]. Available: http://dx.doi.org/10.1021/la800305j

[7] K. L. Kelly, E. Coronado, L. L. Zhao, and G. C. Schatz, "The Optical Properties of Metal Nanoparticles: The Influence of Size, Shape, and Dielectric Environment," *J. Phys. Chem. B*, vol. 107, no. 3, pp. 668–677, Jan. 2003. [Online]. Available: http://dx.doi.org/10.1021/jp026731y

[8] M. Pelton and G. W. Bryant, *Introduction to Metal-Nanoparticle Plasmonics*. Somerset, NJ: John Wiley & Sons, 2013.

[9] Y. Teng, K. Ueno, X. Shi, D. Aoyo, J. Qiu, and H. Misawa, "Surface plasmon-enhanced molecular fluorescence induced by gold nanostructures," *Ann. Phys.*, vol. 524, no. 11, pp. 733–740, Nov. 2012. [Online]. Available: http://dx.doi.org/10.1002/andp.201200143

[10] T. D. Corrigan, S. Guo, R. J. Phaneuf, and H. Szmacinski, "Enhanced fluorescence from periodic arrays of silver nanoparticles," *J. Fluoresc.*, vol. 15, no. 5, pp. 777–784, Sep. 2005. [Online]. Available: http://dx.doi.org/10.1007/s10895-005-2987-3

[11] J. C. Hulteen, D. A. Treichel, M. T. Smith, M. L. Duval, T. R. Jensen, and R. P. Van Duyne, "Nanosphere Lithography: Size-Tunable Silver Nanoparticle

and Surface Cluster Arrays," *J. Phys. Chem. B*, vol. 103, no. 19, pp. 3854–3863, May 1999. [Online]. Available: http://dx.doi.org/10.1021/jp9904771

[12] S.-W. Lee, K.-S. Lee, J. Ahn, J.-J. Lee, M.-G. Kim, and Y.-B. Shin, "Highly sensitive biosensing using arrays of plasmonic Au nanodisks realized by nanoimprint lithography," *ACS Nano*, vol. 5, no. 2, pp. 897–904, Feb. 2011. [Online]. Available: http://dx.doi.org/10.1021/nn102041m

[13] K. Du, I. Wathuthanthri, W. Mao, W. Xu, and C.-H. Choi, "Large-area pattern transfer of metallic nanostructures on glass substrates via interference lithography," *Nanotechnology*, vol. 22, no. 28, p. 285306, Jul. 2011. [Online]. Available: http://dx.doi.org/10.1088/0957-4484/22/28/285306

[14] C. F. Bohren and D. R. Huffman, *Absorption and Scattering of Light by Small Particles*. New York: Wiley, 1983.

[15] S. M. Dutra, *Cavity Quantum Electrodynamics: The Strange Theory of Light in a Box*. New York: Wiley, 2005.

[16] M. Fox, *Quantum Optics: An Introduction*. Oxford, UK: Oxford University Press, 2006.

[17] U. Kreibig and M. Vollmer, *Optical Properties of Metal Clusters*. Berlin, Germany: Spinger-Verlag, 1995.

[18] H. Im, N. C. Lindquist, A. Lesuffleur, and S.-H. Oh, "Atomic layer deposition of dielectric overlayers for enhancing the optical properties and chemical stability of plasmonic nanoholes," *ACS Nano*, vol. 4, no. 2, pp. 947–954, Feb. 2010. [Online]. Available: http://dx.doi.org/10.1021/nn901842r

[19] J. Zuloaga, E. Prodan, and P. Nordlander, "Quantum description of the plasmon resonances of a nanoparticle dimer," *Nano Lett.*, vol. 9, no. 2, pp. 887–891, Feb. 2009. [Online]. Available: http://dx.doi.org/10.1021/nl803811g

[20] S. Asano and G. Yamamoto, "Light scattering by a spheroidal particle," *Appl. Opt.*, vol. 14, no. 1, pp. 29–49, Jan. 1975. [Online]. Available: http://dx.doi.org/10.1364/AO.14.000029

[21] R. L. Hightower and C. B. Richardson, "Resonant Mie scattering from a layered sphere," *Appl. Opt.*, vol. 27, no. 23, pp. 4850–4855, Dec. 1988. [Online]. Available: http://dx.doi.org/10.1364/AO.27.004850

[22] S. A. Maier, *Plasmonics: Fundamentals and applications*. New York: Springer US, 2007.

[23] M. Liu, T.-W. Lee, S. Gray, P. Guyot-Sionnest, and M. Pelton, "Excitation of Dark Plasmons in Metal Nanoparticles by a Localized Emitter," *Phys. Rev. Lett.*, vol. 102, no. 10, p. 107401, Mar. 2009. [Online]. Available: http://dx.doi.org/10.1103/PhysRevLett.102.107401

[24] E. Encina and E. Coronado, "Resonance Conditions for Multipole Plasmon Excitations in Noble Metal Nanorods," *J. Phys. Chem. C*, vol. 111, no. 45, pp. 16 796–16 801, Nov. 2007. [Online]. Available: http://dx.doi.org/10.1021/jp075880j

[25] C. Noguez, "Surface Plasmons on Metal Nanoparticles: The Influence of Shape and Physical Environment," *J. Phys. Chem. C*, vol. 111, no. 10, pp. 3806–3819, Mar. 2007. [Online]. Available: http://dx.doi.org/10.1021/jp066539m

[26] K.-S. Lee and M. A. El-Sayed, "Dependence of the enhanced optical scattering efficiency relative to that of absorption for gold metal nanorods on aspect ratio, size, end-cap shape, and medium refractive index," *J. Phys. Chem. B*, vol. 109, no. 43, pp. 20 331–20 338, Nov. 2005. [Online]. Available: http://dx.doi.org/10.1021/jp054385p

[27] M. Meier and A. Wokaun, "Enhanced fields on large metal particles: dynamic depolarization," *Opt. Lett.*, vol. 8, no. 11, p. 581, Nov. 1983. [Online]. Available: http://dx.doi.org/10.1364/OL.8.000581

[28] A. S. Kumbhar, M. K. Kinnan, and G. Chumanov, "Multipole plasmon resonances of submicron silver particles," *J. Am. Chem. Soc.*, vol. 127, no. 36, pp. 12 444–12 445, Sep. 2005. [Online]. Available: http://dx.doi.org/10.1021/ja053242d

[29] J. J. Mock, D. R. Smith, and S. Schultz, "Local Refractive Index Dependence of Plasmon Resonance Spectra from Individual Nanoparticles," *Nano Lett.*, vol. 3, no. 4, pp. 485–491, Apr. 2003. [Online]. Available: http://dx.doi.org/10.1021/nl0340475

[30] G. Xu, M. Tazawa, P. Jin, S. Nakao, and K. Yoshimura, "Wavelength tuning of surface plasmon resonance using dielectric layers on silver island films," *Appl. Phys. Lett.*, vol. 82, no. 22, pp. 3811–3813, May 2003. [Online]. Available: http://dx.doi.org/10.1063/1.1578518

[31] T. R. Jensen, M. D. Malinsky, C. L. Haynes, and R. P. Van Duyne, "Nanosphere Lithography: Tunable Localized Surface Plasmon Resonance Spectra of Silver Nanoparticles," *J. Phys. Chem. B*, vol. 104, no. 45, pp. 10 549–10 556, Nov. 2000. [Online]. Available: http://dx.doi.org/10.1021/jp002435e

[32] W. A. Murray, J. R. Suckling, and W. L. Barnes, "Overlayers on silver nanotriangles: Field confinement and spectral position of localized surface plasmon resonances," *Nano Lett.*, vol. 6, no. 8, pp. 1772–1777, Aug. 2006. [Online]. Available: http://dx.doi.org/10.1021/nl060812e

[33] F. Bernal Arango, A. Kwadrin, and A. F. Koenderink, "Plasmonic antennas hybridized with dielectric waveguides," *ACS Nano*, vol. 6, no. 11, pp. 10 156–10 167, Nov. 2012. [Online]. Available: http://dx.doi.org/10.1021/nn303907r

[34] L. Novotny and B. Hecht, *Principles of Nano-Optics*, 2nd ed. Cambridge, UK: Cambridge University Press, 2012.

[35] M. W. Knight, Y. Wu, J. B. Lassiter, P. Nordlander, and N. J. Halas, "Substrates matter: influence of an adjacent dielectric on an individual plasmonic nanoparticle," *Nano Lett.*, vol. 9, no. 5, pp. 2188–2192, May 2009. [Online]. Available: http://dx.doi.org/10.1021/nl900945q

[36] Y. Wu and P. Nordlander, "Finite-Difference Time-Domain Modeling of the Optical Properties of Nanoparticles near Dielectric Substrates," *J. Phys. Chem. C*, vol. 114, no. 16, pp. 7302–7307, Apr. 2010. [Online]. Available: http://dx.doi.org/10.1021/jp908980d

[37] T. Wenzel, J. Bosbach, F. Stietz, and F. Träger, "In situ determination of the shape of supported silver clusters during growth," *Surf. Sci.*, vol. 432, no. 3, pp. 257–264, Jul. 1999. [Online]. Available: http://dx.doi.org/10.1016/S0039-6028(99)00546-4

[38] R. Lazzari, S. Roux, I. Simonsen, J. Jupille, D. Bedeaux, and J. Vlieger, "Multipolar plasmon resonances in supported silver particles: The case of $Ag/\alpha - Al_2O_3(0001)$," *Phys. Rev. B*, vol. 65, no. 23, p. 235424, Jun. 2002. [Online]. Available: http://dx.doi.org/10.1103/PhysRevB.65.235424

[39] J. R. Lakowicz, Y. Shen, S. D'Auria, J. Malicka, J. Fang, Z. Gryczynski, and I. Gryczynski, "Radiative decay engineering: 2. Effects of Silver Island Films on Fluorescence Intensity, Lifetimes, and Resonance Energy Transfer," *Anal. Biochem.*, vol. 301, no. 2, pp. 261–277, Feb. 2002. [Online]. Available: http://dx.doi.org/10.1006/abio.2001.5503

[40] L. Zhao, K. L. Kelly, and G. C. Schatz, "The Extinction Spectra of Silver Nanoparticle Arrays: Influence of Array Structure on Plasmon Resonance Wavelength and Width," *J. Phys. Chem. B*, vol. 107, no. 30, pp. 7343–7350, Jul. 2003. [Online]. Available: http://dx.doi.org/10.1021/jp034235j

[41] E. Prodan, C. Radloff, N. J. Halas, and P. Nordlander, "A hybridization model for the plasmon response of complex nanostructures," *Science*, vol. 302, no. 5644, pp. 419–422, Oct. 2003. [Online]. Available: http://dx.doi.org/10.1126/science.1089171

[42] C. L. Haynes, A. D. McFarland, L. Zhao, R. P. Van Duyne, G. C. Schatz, L. Gunnarsson, J. Prikulis, B. Kasemo, and M. Käll, "Nanoparticle Optics: The Importance of Radiative Dipole Coupling in Two-Dimensional Nanoparticle Arrays," *J. Phys. Chem. B*, vol. 107, no. 30, pp. 7337–7342, Jul. 2003. [Online]. Available: http://dx.doi.org/10.1021/jp034234r

[43] A. B. Evlyukhin, C. Reinhardt, U. Zywietz, and B. N. Chichkov, "Collective resonances in metal nanoparticle arrays with dipole-quadrupole interactions," *Phys. Rev. B*, vol. 85, no. 24, p. 245411, Jun. 2012. [Online]. Available: http://dx.doi.org/10.1103/PhysRevB.85.245411

[44] J. Sung, E. M. Hicks, R. P. Van Duyne, and K. G. Spears, "Nanoparticle Spectroscopy: Plasmon Coupling in Finite-Sized Two-Dimensional Arrays of Cylindrical Silver Nanoparticles," *J. Phys. Chem. C*, vol. 112, no. 11, pp. 4091–4096, Mar. 2008. [Online]. Available: http://dx.doi.org/10.1021/jp077332b

[45] A. G. Nikitin, A. V. Kabashin, and H. Dallaporta, "Plasmonic resonances in diffractive arrays of gold nanoantennas: near and far field effects," *Opt. Express*, vol. 20, no. 25, pp. 27 941–27 952, Dec. 2012. [Online]. Available: http://dx.doi.org/10.1364/OE.20.027941

[46] V. G. Kravets, F. Schedin, and A. N. Grigorenko, "Extremely Narrow Plasmon Resonances Based on Diffraction Coupling of Localized Plasmons in Arrays of Metallic Nanoparticles," *Phys. Rev. Lett.*, vol. 101, no. 8, p. 087403, Aug. 2008. [Online]. Available: http://dx.doi.org/10.1103/PhysRevLett.101.087403

[47] V. G. Kravets, F. Schedin, G. Pisano, B. Thackray, P. A. Thomas, and A. N. Grigorenko, "Nanoparticle arrays: From magnetic response to coupled plasmon resonances," *Phys. Rev. B*, vol. 90, no. 12, p. 125445, Sep. 2014. [Online]. Available: http://dx.doi.org/10.1103/PhysRevB.90.125445

[48] B. Auguié, X. M. Bendaña, W. L. Barnes, and F. J. García de Abajo, "Diffractive arrays of gold nanoparticles near an interface: Critical role of the substrate," *Phys. Rev. B*, vol. 82, no. 15, p. 155447, Oct. 2010. [Online]. Available: http://dx.doi.org/10.1103/PhysRevB.82.155447

[49] B. Auguié and W. Barnes, "Collective Resonances in Gold Nanoparticle Arrays," *Phys. Rev. Lett.*, vol. 101, no. 14, p. 143902, Sep. 2008. [Online]. Available: http://dx.doi.org/10.1103/PhysRevLett.101.143902

[50] A. Vitrey, L. Aigouy, P. Prieto, J. M. García-Martín, and M. U. González, "Parallel collective resonances in arrays of gold nanorods," *Nano Lett.*, vol. 14, no. 4, pp. 2079–2085, Jan. 2014. [Online]. Available: http://dx.doi.org/10.1021/nl500238h

[51] H. Xu, J. Aizpurua, M. Käll, and P. Apell, "Electromagnetic contributions to single-molecule sensitivity in surface-enhanced Raman scattering," *Phys. Rev. E*, vol. 62, no. 3, pp. 4318–4324, Sep. 2000. [Online]. Available: http://dx.doi.org/10.1103/PhysRevE.62.4318

[52] J. Gersten and A. Nitzan, "Electromagnetic theory of enhanced Raman scattering by molecules adsorbed on rough surfaces," *J. Chem. Phys.*, vol. 73, no. 7, pp. 3023–3037, Jul. 1980. [Online]. Available: http://dx.doi.org/10.1063/1.440560

[53] E. Hao and G. C. Schatz, "Electromagnetic fields around silver nanoparticles and dimers," *J. Chem. Phys.*, vol. 120, no. 1, pp. 357–366, Jan. 2004. [Online]. Available: http://dx.doi.org/10.1063/1.1629280

[54] N. Calander and M. Willander, "Theory of surface-plasmon resonance optical-field enhancement at prolate spheroids," *J. Appl. Phys.*, vol. 92, no. 9, p. 4878, Oct. 2002. [Online]. Available: http://dx.doi.org/10.1063/1.1512315

[55] A. Kinkhabwala, Z. Yu, S. Fan, Y. Avlasevich, K. Müllen, and W. E. Moerner, "Large single-molecule fluorescence enhancements produced by a bowtie nanoantenna," *Nat. Photonics*, vol. 3, no. 11, pp. 654–657, Oct. 2009. [Online]. Available: http://dx.doi.org/10.1038/nphoton.2009.187

[56] P. W. Barber, R. K. Chang, and H. Massoudi, "Surface-Enhanced Electric Intensities on Large Silver Spheroids," *Phys. Rev. Lett.*, vol. 50, no. 13, pp. 997–1000, Mar. 1983. [Online]. Available: http://dx.doi.org/10.1103/PhysRevLett.50.997

[57] D. J. Griffiths, *Introduction to Quantum Mechanics*. Upper Saddle River, NJ: Prentice Hall, 1994.

[58] P. Atkins and R. Friedman, *Molecular Quantum Mechanics*, 4th ed. New York: Oxford University Press, 2005.

[59] P. Atkins and J. de Paula, *Physical Chemistry*, 8th ed. Oxford, UK: Oxford University Press, 2006.

[60] G. Juzeliūnas and D. L. Andrews, *Quantum electrodynamics of resonance energy transfer* (Advances in Chemical Physics 112), I. Prigogine and A. Rice, Stuart, Eds. Hoboken, NJ: John Wiley & Sons, Inc., 2000. [Online]. Available: http://dx.doi.org/10.1002/9780470141717.ch4

[61] R. Chakrabarty, P. S. Mukherjee, and P. J. Stang, "Supramolecular coordination: self-assembly of finite two- and three-dimensional ensembles," *Chem. Rev.*, vol. 111, no. 11, pp. 6810–6918, Nov. 2011. [Online]. Available: http://dx.doi.org/10.1021/cr200077m

[62] A. Eisfeld and J. Briggs, "The J- and H-bands of organic dye aggregates," *Chem. Phys.*, vol. 324, no. 2-3, pp. 376–384, May 2006. [Online]. Available: http://dx.doi.org/10.1016/j.chemphys.2005.11.015

[63] M. Kasha, H. R. Rawls, and M. Ashraf El-Bayoumi, "The exciton model in molecular spectroscopy," *Pure Appl. Chem.*, vol. 11, no. 3-4, pp. 371–392, Jan. 1965. [Online]. Available: http://dx.doi.org/10.1351/pac196511030371

[64] F. L. Arbeloa, P. R. Ojeda, and I. L. Arbeloa, "Dimerization and trimerization of rhodamine 6G in aqueous solution. Effect on the fluorescence quantum yield," *J. Chem. Soc. Faraday Trans. 2*, vol. 84, no. 12, pp. 1903–1912, Jan. 1988. [Online]. Available: http://dx.doi.org/10.1039/F29888401903

[65] M. S. Tame, K. R. McEnery, . K. Özdemir, J. Lee, S. A. Maier, and M. S. Kim, "Quantum plasmonics," *Nat. Phys.*, vol. 9, no. 6, pp. 329–340, Jun. 2013. [Online]. Available: http://dx.doi.org/10.1038/nphys2615

[66] E. M. Purcell, "Spontaneous emission probabilities at radio frequencies," in *Phys. Rev.*, vol. 69, 1946, p. 681.

[67] J. R. Lakowicz, "Radiative decay engineering 5: metal-enhanced fluorescence and plasmon emission." *Anal. Biochem.*, vol. 337, no. 2, pp. 171–94, Feb. 2005. [Online]. Available: http://dx.doi.org/10.1016/j.ab.2004.11.026

[68] P. N. Prasad, *Nanophotonics*. Hoboken, NJ: Wiley, 2004. [Online]. Available: http://dx.doi.org/10.1002/0471670251

[69] T. H. Taminiau, F. D. Stefani, F. B. Segerink, and N. F. van Hulst, "Optical antennas direct single-molecule emission," *Nat. Photonics*, vol. 2, no. 4, pp. 234–237, Mar. 2008. [Online]. Available: http://dx.doi.org/10.1038/nphoton.2008.32

[70] F. Tam, G. P. Goodrich, B. R. Johnson, and N. J. Halas, "Plasmonic enhancement of molecular fluorescence." *Nano Lett.*, vol. 7, no. 2, pp. 496–501, Feb. 2007. [Online]. Available: http://dx.doi.org/10.1021/nl062901x

[71] O. Stranik, H. McEvoy, C. McDonagh, and B. MacCraith, "Plasmonic enhancement of fluorescence for sensor applications," *Sensors Actuators B Chem.*, vol. 107, no. 1, pp. 148–153, May 2005. [Online]. Available: http://dx.doi.org/10.1016/j.snb.2004.08.032

[72] P. Bharadwaj, P. Anger, and L. Novotny, "Nanoplasmonic enhancement of single-molecule fluorescence," *Nanotechnology*, vol. 18, no. 4, p. 044017, Jan. 2007. [Online]. Available: http://dx.doi.org/10.1088/0957-4484/18/4/044017

[73] G. Sun and J. B. Khurgin, "Plasmon Enhancement of Luminescence by Metal Nanoparticles," *IEEE J. Sel. Top. Quantum Electron.*, vol. 17, no. 1, pp. 110–118, Jan. 2011. [Online]. Available: http://dx.doi.org/10.1109/JSTQE.2010.2047249

[74] H. Wang, Y. Wu, B. Lassiter, C. L. Nehl, J. H. Hafner, P. Nordlander, and N. J. Halas, "Symmetry breaking in individual plasmonic nanoparticles," *Proc. Natl. Acad. Sci. U. S. A.*, vol. 103, no. 29, pp. 10 856–10 860, Jul. 2006. [Online]. Available: http://dx.doi.org/10.1073/pnas.0604003103

[75] G. T. Boyd, T. Rasing, J. R. R. Leite, and Y. R. Shen, "Local-field enhancement on rough surfaces of metals, semimetals, and semiconductors with the use of optical second-harmonic generation," *Phys. Rev. B*, vol. 30, no. 2, pp. 519–526, Jul. 1984. [Online]. Available: http://dx.doi.org/10.1103/PhysRevB.30.519

[76] M. Thomas, J.-J. Greffet, R. Carminati, and J. R. Arias-Gonzalez, "Single-molecule spontaneous emission close to absorbing nanostructures," *Appl. Phys. Lett.*, vol. 85, no. 17, pp. 3863–3865, Oct. 2004. [Online]. Available: http://dx.doi.org/10.1063/1.1812592

[77] Y. Chen, K. Munechika, and D. S. Ginger, "Dependence of fluorescence intensity on the spectral overlap between fluorophores and plasmon resonant single silver nanoparticles," *Nano Lett.*, vol. 7, no. 3, pp. 690–696, Mar. 2007. [Online]. Available: http://dx.doi.org/10.1021/nl062795z

[78] M. Ringler, A. Schwemer, M. Wunderlich, A. Nichtl, K. Kürzinger, T. A. Klar, and J. Feldmann, "Shaping Emission Spectra of Fluorescent Molecules with Single Plasmonic Nanoresonators," *Phys. Rev. Lett.*, vol. 100, no. 20, p. 203002, May 2008. [Online]. Available: http://dx.doi.org/10.1103/PhysRevLett.100.203002

[79] J. Zhang, Y. Fu, and J. R. Lakowicz, "Enhanced Förster Resonance Energy Transfer (FRET) on a Single Metal Particle," *J. Phys. Chem. C*, vol. 111, no. 1, pp. 50–56, Jan. 2007. [Online]. Available: http://dx.doi.org/10.1021/jp062665e

[80] A. Natansohn and P. Rochon, "Photoinduced Motions in Azo-Containing Polymers," *Chem. Rev.*, vol. 102, no. 11, pp. 4139–4176, Nov. 2002. [Online]. Available: http://dx.doi.org/10.1021/cr970155y

[81] A. Priimagi and A. Shevchenko, "Azopolymer-based micro- and nanopatterning for photonic applications," *J. Polym. Sci. Part B Polym. Phys.*, vol. 52, no. 3, pp. 163–182, Feb. 2014. [Online]. Available: http://dx.doi.org/10.1002/polb.23390

[82] P. Rochon, E. Batalla, and A. Natansohn, "Optically induced surface gratings on azoaromatic polymer films," *Appl. Phys. Lett.*, vol. 66, no. 2, pp. 136–138, Jan. 1995. [Online]. Available: http://dx.doi.org/10.1063/1.113541

[83] D. Y. Kim, S. K. Tripathy, L. Li, and J. Kumar, "Laser-induced holographic surface relief gratings on nonlinear optical polymer films," *Appl. Phys. Lett.*, vol. 66, no. 10, p. 1166, Mar. 1995. [Online]. Available: http://dx.doi.org/10.1063/1.113845

[84] A. Kravchenko, A. Shevchenko, P. Grahn, V. Ovchinnikov, and M. Kaivola, "Photolithographic periodic patterning of gold using azobenzene-functionalized polymers," *Thin Solid Films*, vol. 540, pp. 162–167, Jul. 2013. [Online]. Available: http://dx.doi.org/10.1016/j.tsf.2013.05.156

[85] A. Kravchenko, A. Shevchenko, V. Ovchinnikov, A. Priimagi, and M. Kaivola, "Optical interference lithography using azobenzene-functionalized polymers for micro- and nanopatterning of silicon," *Adv. Mater.*, vol. 23, no. 36, pp. 4174–4177, Sep. 2011. [Online]. Available: http://dx.doi.org/10.1002/adma.201101888

[86] H. Aouani, J. Wenger, D. Gérard, H. Rigneault, E. Devaux, T. W. Ebbesen, F. Mahdavi, T. Xu, and S. Blair, "Crucial role of the adhesion layer on the plasmonic fluorescence enhancement," *ACS Nano*, vol. 3, no. 7, pp. 2043–2048, Jul. 2009. [Online]. Available: http://dx.doi.org/10.1021/nn900460t

[87] C. Brinker, G. Frye, A. Hurd, and C. Ashley, "Fundamentals of sol-gel dip coating," *Thin Solid Films*, vol. 201, no. 1, pp. 97–108, Jun. 1991. [Online]. Available: http://dx.doi.org/10.1016/0040-6090(91)90158-T

[88] C. Jeffrey Brinker and A. J. Hurd, "Fundamentals of sol-gel dip-coating," *J. Phys. III*, vol. 4, no. 7, pp. 1231–1242, Jul. 1994. [Online]. Available: http://dx.doi.org/10.1051/jp3:1994198

[89] L. D. Landau and B. G. Levich, "Dragging of a liquid by a moving plate," *Acta Physiochimica U.R.S.S.*, vol. 17, no. 1-2, pp. 42–54, 1942.

[90] B. H. Soffer, "Continuously tunable, narrow-band organic dye lasers," *Appl. Phys. Lett.*, vol. 10, no. 10, pp. 266–267, Nov. 1967. [Online]. Available: http://dx.doi.org/10.1063/1.1754804

[91] D. Magde, R. Wong, and P. G. Seybold, "Fluorescence Quantum Yields and Their Relation to Lifetimes of Rhodamine 6G and Fluorescein in Nine Solvents: Improved Absolute Standards for Quantum Yields," *Photochem. Photobiol.*, vol. 75, no. 4, pp. 327–334, May 2007. [Online]. Available: http://dx.doi.org/10.1562/0031-8655(2002)0750327FQYATR2.0.CO2

[92] D. Magde, G. E. Rojas, and P. G. Seybold, "Solvent Dependence of the Fluorescence Lifetimes of Xanthene Dyes," *Photochem. Photobiol.*, vol. 70, no. 5, pp. 737–744, Nov. 1999. [Online]. Available: http://dx.doi.org/10.1111/j.1751-1097.1999.tb08277.x

[93] R. M. Taylor, B. Lin, T. R. Foubert, J. B. Burritt, J. Sunner, and A. J. Jesaitis, "Cascade blue as a donor for resonance energy transfer studies of heme-containing proteins," *Anal. Biochem.*, vol. 302, no. 1, pp. 19–27, Mar. 2002. [Online]. Available: http://dx.doi.org/10.1006/abio.2001.5523

[94] G. A. Parks, "The Isoelectric Points of Solid Oxides, Solid Hydroxides, and Aqueous Hydroxo Complex Systems," *Chem. Rev.*, vol. 65, no. 2, pp. 177–198, Apr. 1965. [Online]. Available: http://dx.doi.org/10.1021/cr60234a002

[95] Z. Chen, Y.-J. Tang, T.-T. Xie, Y. Chen, and Y.-Q. Li, "Fluorescence spectral properties of rhodamine 6G at the silica/water interface," *J. Fluoresc.*, vol. 18, no. 1, pp. 93–100, Jan. 2008. [Online]. Available: http://dx.doi.org/10.1007/s10895-007-0241-x

[96] A. C. Polycarpou, "Introduction to the Finite Element Method in Electromagnetics," *Synth. Lect. Comput. Electromagn.*, vol. 1, no. 1, pp. 1–126, Jan. 2006. [Online]. Available: http://dx.doi.org/10.2200/S00019ED1V01Y200604CEM004

[97] J.-M. Jin and D. J. Riley, *Finite Element Analysis of Antennas and Arrays*. Hoboken, NJ: John Wiley & Sons, Inc., 2008. [Online]. Available: http://dx.doi.orf/10.1002/9780470409732

[98] A. M. Kern and O. J. F. Martin, "Excitation and reemission of molecules near realistic plasmonic nanostructures," *Nano Lett.*, vol. 11, no. 2, pp. 482–487, Feb. 2011. [Online]. Available: http://dx.doi.org/10.1021/nl1032588

[99] P. B. Johnson and R. W. Christy, "Optical constants of the noble metals," *Phys. Rev. B*, vol. 6, no. 12, pp. 4370–4379, 1972. [Online]. Available: http://dx.doi.org/10.1103/PhysRevB.6.4370

[100] E. Hecht, *Optics*, 4th ed. San Francisco, CA: Addison Wesley, 2002.

[101] M. G. Gore, *Spectrophotometry and Spectrofluorimetry: A Practical Approach* (Practical Approach Series 225), B. D. Hames, Ed. New York: Oxford University Press, 2000.

[102] M. Muller, *Introduction to Confocal Fluorescence Microscopy*, 2nd ed. Bellingham, WA: SPIE, 2006. [Online]. Available: http://dx.doi.org/10.1117/3.639736

[103] W. Rasband, "ImageJ - Image Processing and Analysis in Java," 2004. [Online]. Available: http://imagej.nih.gov/ij/

[104] S. Franssila, *Introduction to Microfabrication*, 2nd ed. Hoboken, NJ: John Wiley & Sons, 2010. [Online]. Available: http://dx.doi.org/10.1002/9781119990413

[105] S. Y. Chou and Q. Xia, "Improved nanofabrication through guided transient liquefaction," *Nat. Nanotechnol.*, vol. 3, no. 5, pp. 295–300, May 2008. [Online]. Available: http://dx.doi.org/10.1038/nnano.2008.95

[106] K. R. Williams, K. Gupta, and M. Wasilik, "Etch rates for micromachining processing—Part II," *J. Microelectromechanical Syst.*, vol. 12, no. 6, pp. 761–778, 2003. [Online]. Available: http://dx.doi.org/10.1109/JMEMS.2003.820936